An Introduction to the Global Circulation of the Atmosphere

David A. Randall

Contents

Preface

This is a graduate-level introductory overview of the global circulation of the atmosphere, a subject that is closely tied to atmospheric dynamics. It is an updated, extended, and corrected version of my book with the same title, which was published in 2015 by Princeton University Press. Color figures were not permitted in the published book, but I am using them extensively in this updated version, which may (or may not) eventually become the second edition of the book.

Graduate-level studies in atmospheric dynamics are essential as preparation for reading this book. I have assumed that the reader is familiar with basic concepts of atmospheric dynamics such as the equation of motion, the approximate hydrostatic and geostrophic balances, potential temperature, vorticity, and planetary waves. More advanced dynamical concepts are introduced as needed. Chapter 4, in particular, gives a brief but fairly detailed overview of the concepts used throughout the book. Some instructors may choose to refer to Chapter 4 only as needed when concepts are used in the later chapters. A course on dynamics tends to focus on basic physical concepts and methods for their analysis, however, while a course on the global circulation must focus on what the atmosphere actually does, and why.

I have also included quite a bit of discussion of the mechanisms that give rise to the thermal driving of the global circulation, and the feedbacks of the circulation on those diabatic processes. We can't claim to understand the circulation unless we understand the heating that drives it, as well as how the circulation influences the heating. This part of the story is particularly interesting, and also particularly challenging.

Tropical meteorology has been at least partially subsumed into the study of the global circulation. This is natural, in part because the tropics covers about half the planet, in terms of surface area. In addition, the tropics is home to major heating and cooling processes that invigorate the global circulation.

It is difficult to draw a line between the global circulation and climate. The two subjects are growing closer together, as the roles of heating and dissipation in the global circulation emerge as key issues. Such topics as monsoons, the hydrologic cycle, and the planetary energy budget can be included under either "climate" or "global circulation," although perhaps with different slants. Climate is the bigger subject. This book skirts the edges of

physical climatology.

I have chosen to discuss many of the topics in terms of their original sources, rather than the latest papers. This quasi-historical approach gives credit to the pioneers of our field, and highlights some of the human aspects of the research.

The global circulation involves many named "emergent" phenomena. I think it's important to tie the discussion of these phenomena back to first principles, so that the students will learn more than just the high-level lingo.

Some of the problems at the ends of the chapters involve working with observations. The Internet has made it unnecessary to include the data with the book. Many of the figures in this book were made using the Interim Reanalysis of the European Centre for Medium Range Weather Forecasts, which would be a suitable source of global atmospheric data for use with the problems, (although of course there are other possibilities).

Mark Branson and Don Dazlich ably produced many of the figures. I could not have finished without their help.

Chapter 1

Perpetual Motion

The atmosphere *circulates*. The circulation is global in extent (Fig. 1.1). The circulating mass consists of "dry air" and three phases of water. Energy and momentum are carried with the air, but evolve in response to various processes along the way. Many of those same processes add or remove moisture.

The circulation is sustained by thermal forcing, which ultimately comes from the Sun. On the average, the Earth absorbs about 240 W m^{-2} of incoming or "incident" solar energy, of which roughly 2% is converted to maintain the kinetic energy of the global circulation against frictional dissipation. Additional, "primordial" energy leaks out of the Earth's interior, but at the relatively tiny rate of 0.1 W m^{-2} (Sclater et al., 1980; Bukowinski, 1999). The thermal forcing of the global circulation is strongly influenced by the circulation itself, e.g., as clouds form and disappear. The interactions between the circulation and the heating are fascinating but complicated.

When averaged over time, the global circulation has to satisfy various balance requirements. For example, in a time average, the infrared radiation emitted at the top of the atmosphere must balance the solar radiation absorbed, precipitation must balance evaporation, and angular momentum exchanges between the atmosphere and the ocean-solid Earth system must sum to zero. We will discuss the global circulation from this classical perspective. We will also supplement this discussion, however, with descriptions and analyses of the many and varied but inter-related phenomena of the circulation, including such things as the Hadley and Walker circulations, monsoons, stratospheric sudden warmings, the Southern Oscillation, subtropical highs, and extratropical storm tracks.

In addition, we will discuss the all-important diabatic and frictional processes that maintain the circulation, and the ways in which these processes are affected by the circulation itself.

The circulations of energy and water are closely linked. It takes about 2.5 million Joules of energy to evaporate one kilogram of water from the oceans, and the same amount of energy is released when the water vapor condenses to form a cloud. This "latent heat"

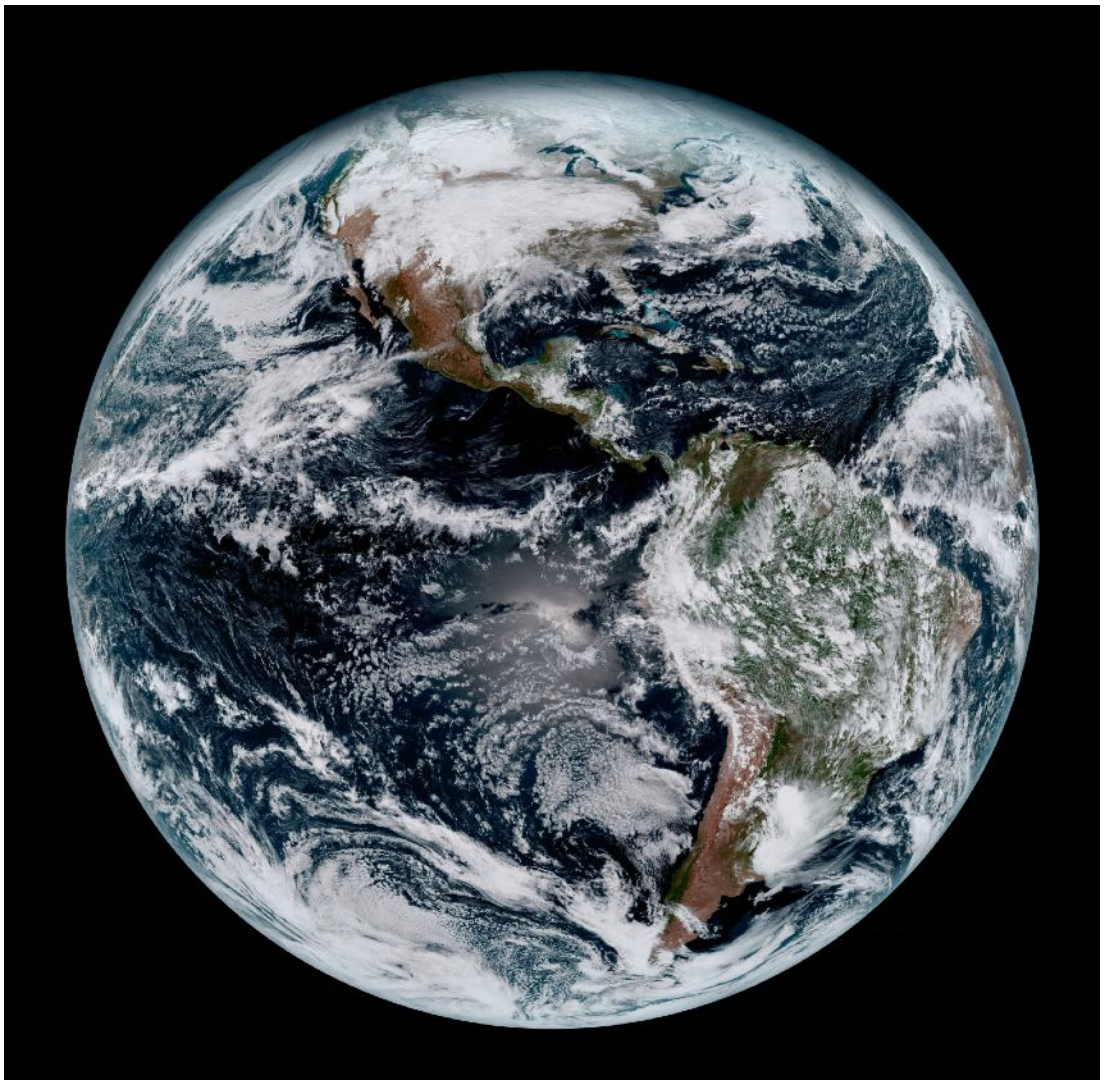

Figure 1.1: A full disk image of the Earth taken by the GOES-16 satellite at 1:07 p.m. EDT on January 15, 2017 , looking down on the Equator, with North and South American in view. Many elements of the global circulation can be seen in this picture, including the "inter-tropical" rain band in the eastern North Pacific, swirling midlatitude storms, and the low clouds associated with the high-pressure systems over the eastern subtropical oceans. From `https://www.nesdis.noaa.gov/content/goes-16-color-composite-images`.

release through condensation drives thunderstorm updrafts that in one hour or less can penetrate to heights of ten or even twenty kilometers. The cloudy outflows from such storms reflect sunlight back to space, and block infrared radiation from the warm surface below. Shallower clouds cast shadows over vast expanses of the oceans. One of the aims of this book is to give proper emphasis to the role of moisture in the global circulation of the atmosphere.

It is conventional and useful, although somewhat arbitrary, to divide the atmosphere

into parts. For purposes of this quick sketch, we will divide the atmosphere vertically and meridionally, only briefly mentioning the longitudinal variations. Let's start at the bottom, and work our way into the sky.

Most of the solar radiation that the Earth absorbs is captured by the surface, rather than within the relatively transparent atmosphere. Several processes act to transfer the absorbed energy upward, from the ocean and land surface into the lower portion of the atmosphere. The layer of air that is closely coupled with the Earth's surface is, by definition, the "planetary boundary layer," or PBL. The top of the PBL is often very sharp and well defined (Fig. 1.2). The depth of the PBL varies dramatically in space and time, but a ball-park value to remember is 1 km. The air in the PBL is turbulent, and the turbulence is associated with rapid exchanges of "sensible heat" (essentially temperature), moisture, and momentum between the atmosphere and the surface. These "fluxes" have dimensions of energy per unit area per unit time. They are produced by the turbulence, and also promote the turbulence, through mechanisms that will be discussed later. The most important exchanges are of moisture and momentum. The surface latent heat flux is a key source of energy for the global circulation, and turbulent mixing in the PBL is a key mechanism for dissipation of the kinetic energy of the global circulation. Friction is also a major driver of the circulation of the oceans.

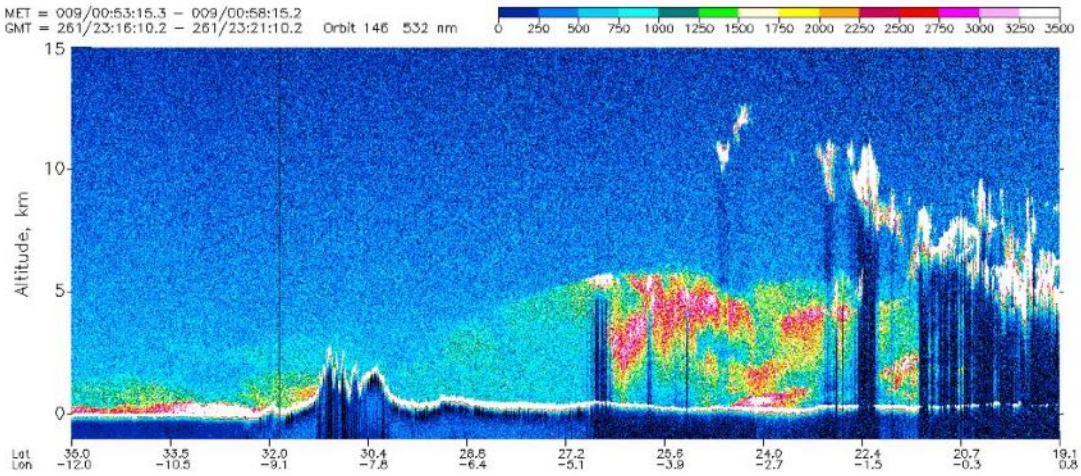

Figure 1.2: This figure shows lidar backscatter from aerosols and clouds. The figure was created using data from LITE, a lidar that flew on the space shuttle in 1994 (Winker et al., 1996). The lidar beam cannot penetrate through thick clouds; this accounts for the dark vertical stripes in the figure. The PBL can be seen in the data because the aerosol concentration decreases sharply upward there. The track shown here starts over the North Atlantic Ocean on the left side, and moves towards the southeast, over Africa. Longitudes and latitudes are given along the bottom of the figure. The Atlas mountains are visible near latitude 31 ° N latitude. From `http://www-lite.larc.nasa.gov/n_saharan_dust.html`.

The troposphere includes the PBL, but it is conventional to add the prefix "free" to

specify the part of the troposphere that lies above the PBL. The PBL is often well mixed, so that air can easily move up or down. The free troposphere has a positive static stability, which means that buoyancy forces resist vertical motion. The depth of the troposphere varies strongly with latitude and season.

A turbulent process called "entrainment" gradually incorporates free-tropospheric air into the PBL. Over the oceans, entrainment is, with a few exceptions, relatively slow but steady. Over land, entrainment is promoted by strong daytime heating of the surface, which helps to generate turbulence. As a result, the turbulent PBL rapidly deepens during the day. When the sun goes down, the processes that promote turbulence and entrainment are abruptly weakened, and the PBL reorganizes itself into a much shallower nocturnal configuration, leaving behind a nno-longer-turbulent layer of air that was part of the PBL during the afternoon. This diurnal deepening and shallowing of the PBL acts as a kind of "pump," which captures air from the free troposphere and adds it to the PBL starting shortly after sunrise, modifies the properties of that air during the day through strong turbulent exchanges with the surface, and then releases the modified air back into the free troposphere at sunset. Diurnal pumping is one way that the PBL exerts an influence on the free troposphere (Denning et al., 1995, 1999).

In addition, however, moisture and energy are carried upward from the PBL into the free troposphere by several mechanisms. Throughout the tropics and the summer-hemisphere middle latitudes, the most important of these mechanisms is cumulus convection. Cumulus clouds typically grow upward from the PBL. The updrafts inside the clouds carry PBL air into the free troposphere, where it is left behind when the clouds decay (Fig. 1.3). One of the effects of this process is to remove air from the PBL, and add it to the free troposphere.

Frontal circulations can also carry air from the PBL into the free atmosphere, essentially by "peeling" the PBL off from the Earth's surface, like the rind from an orange, and lofting the detached air towards the tropopause. This process is especially active in the middle latitudes in winter.

Fig. 1.4 shows somewhat idealized observed midlatitude vertical distributions of temperature, pressure, density, and ozone mixing ratio, from the surface to the 70-km level. For reference, the "top of the atmosphere" is often considered to be 100 km above the surface, but of course this definition is somewhat arbitrary and should be adjusted depending on the context (McDowell, 2018). In the lowest 12 km, the temperature usually decreases monotonically upward; this is the troposphere. The troposphere is cooled radiatively, because it emits infrared radiation much more efficiently than it absorbs solar radiation. The net radiative cooling is balanced mainly by the release of the latent heat of water vapor, as clouds form and precipitate.

The upper boundary of the troposphere is called the tropopause, The height of the tropopause varies from 17 km or so in some regions of the tropics, to about half that near the poles. Above the tropopause, the temperature becomes uniform with height and then begins to increase upward. This region is the stratosphere. The upward increase of tem-

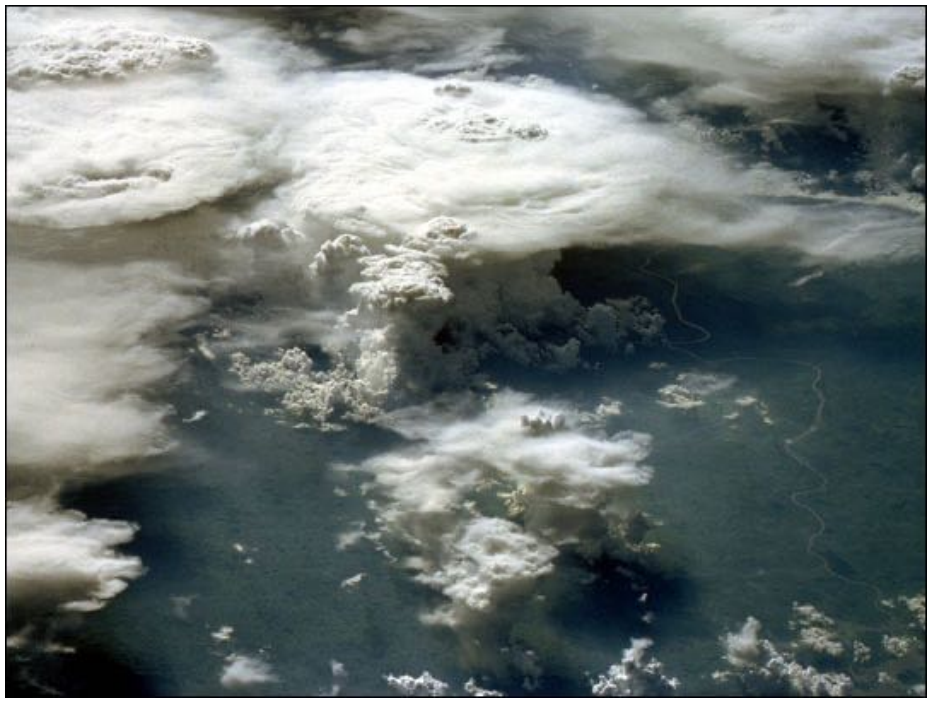

Figure 1.3: A space shuttle photograph of tropical thunderstorms over Brazil. The storms are topped by thick anvil clouds. Much shallower convective clouds can be seen in the foreground. From https://eoimages.gsfc.nasa.gov/images/imagerecords/2000/2443/STS41B-41-2347_lrg.JPG.

perature in the stratosphere is due to the absorption of solar radiation by ozone, which is created in the stratosphere by photochemical processes. Without ozone there would be no stratosphere. The summer-hemisphere stratosphere is almost devoid of active weather, and has warm air over the pole. The summer stratosphere is warmed by the perpetual sunlight, and the winds of the summer stratosphere are predominantly "easterly," which means that they blow from east to west. In contrast, the winter-hemisphere stratosphere has very cold air over the pole, with strong westerly winds, and experiences much more active weather, mainly due to waves propagating upward from the troposphere below. During winter, the polar stratosphere is occasionally disturbed by "Sudden Stratospheric Warmings," which are dramatic changes in temperature (and wind) that occur in many years in the Northern Hemisphere, and much less frequently in the Southern Hemisphere (Baldwin et al., 2021). The tropical stratosphere features an amazing periodic reversal of the zonal (i.e., west-to-east) wind, called the Quasi-Biennial Oscillation, or QBO (Baldwin et al., 2001). Its period is slightly longer than two years.

Even though stratosphere is very dry, its moisture budget is quite interesting. It receives small amounts of moisture from the troposphere, and it also gains some moisture through the oxidation of methane.

The upper boundary of the stratosphere, which is called the stratopause, occurs near the

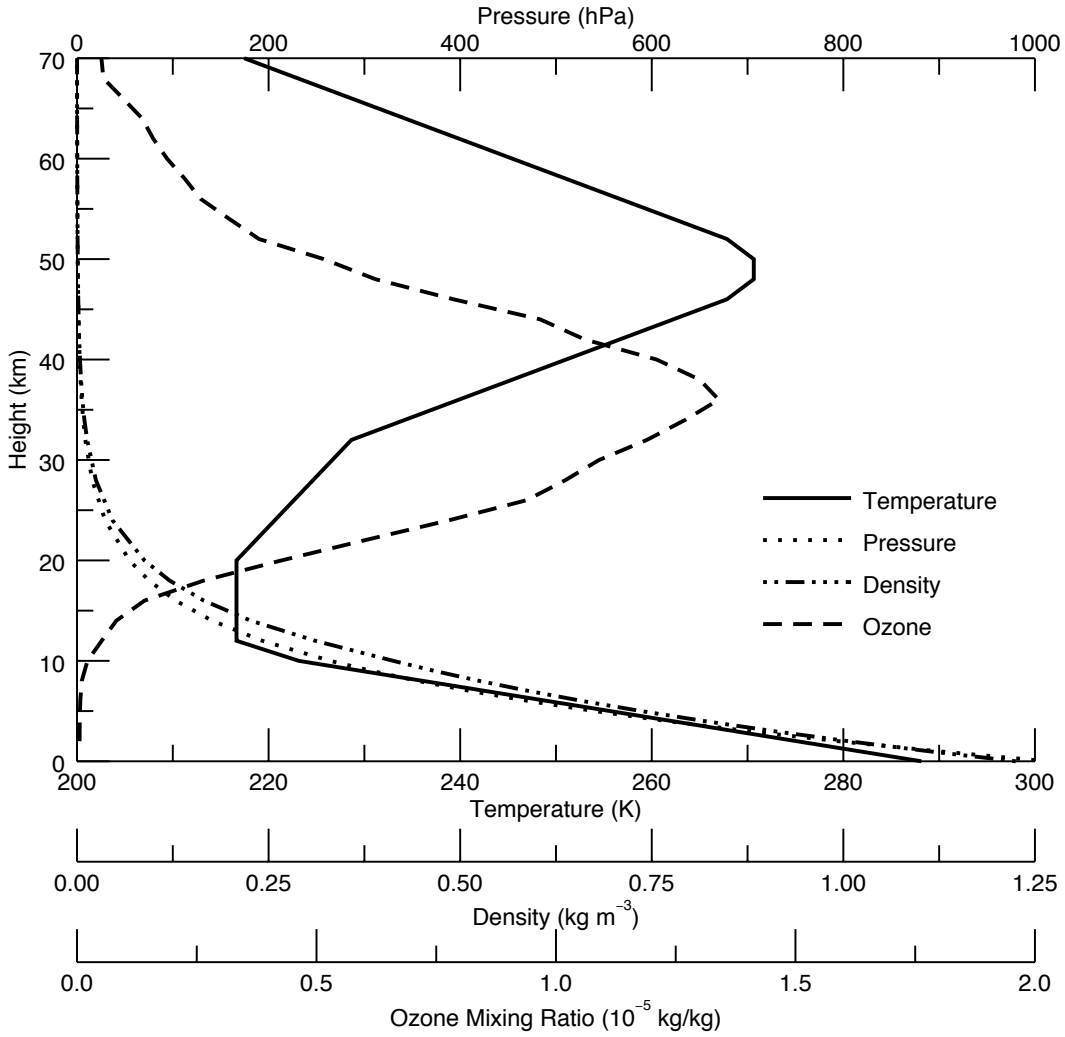

Figure 1.4: Idealized midlatitude temperature, pressure, density and ozone profiles, for the lowest 70 km of the atmosphere. The temperature, pressure, and density profiles are based on the U.S. Standard Atmosphere (National Oceanic and Atmospheric Administration, 1976). The ozone profile is from Krueger and Minzner (1976).

1 hPa ($\sim$ 50 km) level. In this book, we consider the troposphere and the stratosphere, but we will not discuss the layers above the stratopause.

For meteorological purposes, the tropics can be defined as the region from about 20° S to 20° N. Although the tropical temperature and surface pressure are remarkably uniform, the winds and rainfall are quite variable. In many parts of the tropics deep cumulus and cumulonimbus clouds, i.e., thunderstorms, produce lots of rain and transport energy, moisture, and momentum vertically, essentially continuing the job begun closer to the surface by the turbulence of the PBL. The convective clouds often produce strong exchanges of air between the PBL and the free troposphere, in both directions: positively buoyant PBL air

"breaks off" and drifts upward to form the cumuli, while negatively buoyant downdrafts associated with the evaporation of falling rain can inject free-tropospheric air into the PBL. In the convectively active parts of the tropics, the air is slowly rising in an area-averaged sense.

The mean flow in the tropical PBL is easterly; these are the "tradewinds." The tropical temperature and surface pressure distributions are generally very flat and monotonous, for simple dynamical reasons, discussed in Chapter 3, that are connected to the smallness of the tropical Coriolis parameter. The tropical moisture and wind fields are more variable than the temperature, however. The tropics is home to a variety of distinctive traveling waves and vortices, which organize the convective clouds on scales of hundreds to thousands of kilometers. Finally, the tropics is dominated by powerful and very large-scale monsoon systems, which are associated with continental-scale land-sea contrasts, and which actually extend into the subtropics and even middle latitudes.

The tropical atmosphere acquires the angular momentum of the Earth's rotation from the continents and oceans. The global atmospheric circulation carries the angular momentum to higher latitudes, where it is "put back" into the continents and oceans.

The tropical troposphere hosts some circulation phenomena that do not occur in higher latitudes. Most famously, tropical cyclones produce tremendous amounts of rainfall and strong winds. They are relatively small in scale, and highly seasonal. Monsoons are driven by land-sea contrasts. They also very seasonal, and much larger in spatial scale. The Madden-Julian Oscillation, or MJO, is a powerful tropical weather system that influences rainfall across about half of the tropics. El Niño, La Niña, and the Southern Oscillation, which are are collectively known as "ENSO," comprise a strong, quasi-regular oscillation of the ocean-atmosphere system, with a period of a few years (Philander, 1990). In an El Niño, the sea-surface temperatures warm in the eastern (or sometimes central) tropical Pacific, while in a La Niña they cool. The Southern Oscillation is a shift in the pressure and wind fields of the tropical Pacific region, which occurs in conjunction with El Niño and La Niña.

The subtropical portion of each hemisphere is roughly the region between 20° and 30° from the Equator. In many parts of the subtropical troposphere, the air is sinking in large anticyclonic circulation systems called, appropriately enough, "subtropical highs." The subsidence suppresses precipitation, which is why the major deserts of the world are found in the subtropics. Surface evaporation is very strong over the subtropical oceans, which have extensive systems of weakly precipitating shallow clouds. The subtropical upper troposphere is home to powerful "subtropical jets," which are westerly currents that are particularly strong in the winter hemisphere (Fig. 1.5).

The tropical rising motion and subtropical sinking motion can be seen as the vertical branches of a "cellular" circulation in the latitude-height plane. This "Hadley circulation" transports energy and momentum poleward, and it transports moisture toward the Equator. The Hadley circulation interacts strongly with the monsoons.

Figure 1.5: This photograph taken from the space shuttle shows cirrus clouds being carried along by the subtropical jet stream. From http://earth.jsc.nasa.gov/sseop/efs/lores.pl?PHOTO=STS039-601-49.

The region that we call the middle latitudes extends, in each hemisphere, from about 30° to 70° from the Equator. The midlatitude surface winds are primarily westerly. The midlatitude free troposphere is filled with vigorous weather systems called baroclinic eddies, which have scales of a few thousand km and grow as instabilities through a process in which warm air shifts upward and poleward, and is replaced by colder air that descends as it slides toward the Equator (Fig. 1.6). These storms transport energy and moisture poleward and upward, primarily in the winter hemisphere, but also to some extent during summer. They transport westerly momentum poleward and downward, driving currents in the oceans and rustling the leaves on the continents. The energy of the baroclinic eddies is derived from horizontal temperature differences that can only be sustained outside the tropics. They can produce massive cloud systems and heavy precipitation.

On the average, the polar troposphere is characterized by sinking motion and radiative cooling to space. The North Pole is in the Arctic Ocean, which is covered with sea ice (Fig. 1.7) and often blanketed by extensive cloudiness, while the South Pole is in the middle of a dry, mountainous continent (Fig. 1.8). Near the surface, the polar winds tend be easterly, but weak.

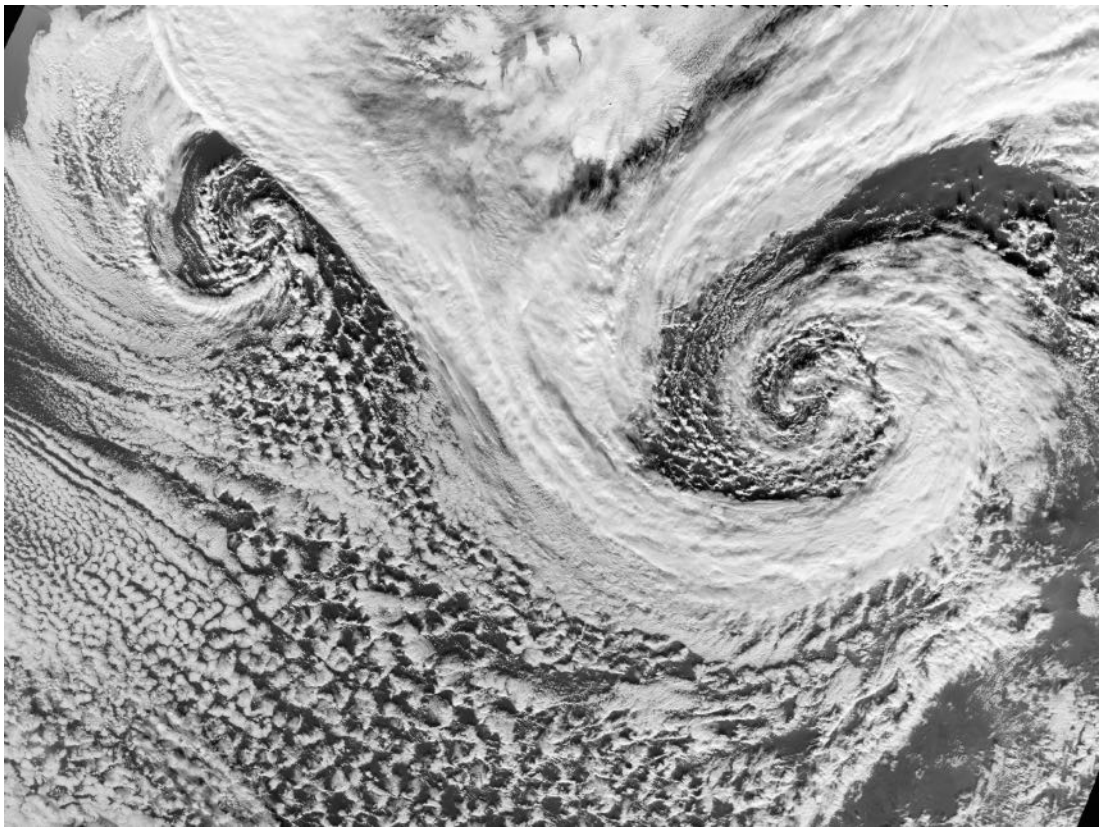

Figure 1.6: A pair of beautiful winter storms over the North Atlantic Ocean in winter. From http://earthobservatory.nasa.gov/IOTD/view.php?id=7264.

The polar regions and middle latitudes are home to prominent "annular modes," which by definition are visible even when the data are averaged over all longitudes. The annular modes fluctuate on a variety of time scales, almost uniformly in longitude. They are seen in both the stratosphere and troposphere, and make major contributions to the overall variability of the global circulation.

Analysis of energy sources, sinks, and transformations can aid in understanding the global circulation. The atmosphere cools radiatively, in an overall sense, and this cooling is balanced primarily by the release of latent heat, which in turn is made possible by surface evaporation. The net flow of energy is upward and towards the poles, carried by thunderstorms and the Hadley Circulation in the tropics, and by baroclinic eddies in middle latitudes. The energy escapes to space via infrared radiation at all latitudes, but especially in the subtropics.

The organization of this book is as follows. Chapter 2 provides an overview of the upper and lower boundary conditions on the global circulation. At the "top of the atmosphere," the observed pattern of radiation implies net poleward energy transports by the atmosphere and ocean together. Lower boundary conditions include the distributions of oceans and

Figure 1.7: An ice station used to collect data in and above the Arctic ocean during 1997-8. From https://en.wikipedia.org/wiki/Surface_Heat_Budget_of_the_Arctic_Ocean#/media/File:Ice_Station_SHEBA-CRREL.jpg.

continents and mountains, the pattern of sea surface temperature and the directly related pattern of sea-surface saturation vapor pressure, the heat capacity of the surface, the distribution of vegetation on the land surface, and the distributions of sea ice and continental glaciers and ice sheets. These lower boundary conditions strongly affect the flows of energy and moisture across the Earth's surface. Chapter 2 closes with a brief overview of the vertically integrated energy and moisture budgets of the surface and atmosphere, and the connections between them.

With this background information out of the way, Chapter 3 presents an observational overview of some basic aspects of the global circulation. We start with the global distribution of atmospheric mass, then move to winds, temperature, and moisture. The amount of interpretation is deliberately kept to a minimum in Chapter 3. By the end of Chapter 3, many important elements of the global circulation have been introduced, giving a basis for further discussion in later chapters.

While Chapter 3 focuses on the observations, Chapter 4 gives a brief but intensive review of concepts that will be used later in the book, starting with the dynamics of fluid motion on a rotating sphere. Angular momentum conservation is derived. We then turn to a detailed discussion of energy transports and transformations. The key subject of potential vorticity is introduced near the end of the chapter. The quasi-geostrophic approximation and the shallow water equations are also introduced.

The term "zonal average" refers to an average over all longitudes. Chapter 6 discusses

Figure 1.8: Cold-looking clouds over the dry mountains of Antarctica. From https://wp.natsci.colostate.edu/walllab/research/antarctica/wall-valley-antarctica-information/.

the zonally averaged circulation, and how it is influenced by sources and sinks of moisture, energy, and momentum. The chapter also presents first look at the effects of "eddies" that transport dry air, moisture, energy, and momentum along "isentropic" surfaces on which the entropy is uniform.

Chapter 8 gives an introduction to the effects of convective energy sources and sinks, starting with a brief review of the nature of buoyant convection in both dry and moist atmospheres. We then outline the famous observational study of convective energy transports by Riehl and Malkus (1958). This is followed by a discussion of the idealized but important concept of radiative-convective equilibrium, and an overview of convective cloud regimes, ranging from deep convection in the tropics to shallow stratocumulus convection in higher latitudes. The concept of convective mass flux is introduced, along with a theory that explains why cumulus updrafts tend to be separated by broad expanses of relatively dry, sinking air. We then show how the convective mass flux can be used to understand the heating and drying associated with cumulus clouds, and what determines the intensity of the convection as a function of the large-scale weather regime. Finally, we introduce the concept of conditional symmetric instability, which is particularly relevant in middle latitudes.

Chapter 7 presents the energetics of the global circulation, beginning with an in-depth discussion of available potential energy and the related concept of the gross static stability. Following Lorenz, these ideas are developed through the use of isentropic coordinates, although we also show how they can be expressed using pressure coordinates. We then discuss the mechanisms by which vertical and meridional gradients of the zonally averaged circulation can be converted into zonally varying features called eddy variances. This leads to a discussion of how available potential energy is generated, and how it is converted into eddy kinetic energy. The chapter closes with a discussion of the observed energy cycle of the global atmosphere.

Chapter 9 introduces various types of eddies, beginning with a brief discussion of the Laplace Tidal Equations, omitting the details of the mathematics. The chapter presents observations of the distribution of energy with scale for midlatitude eddies. We summarize the theory of Rossby waves forced by flow over topography, and Matsuno's theory of Equatorial waves (Matsuno, 1966). This is followed by a discussion of the monsoons, the east-west Walker circulation of the tropical Pacific, and the energy balance of the tropics and subtropics. The chapter closes with discussions of tropical cylcones and the Madden-Julian Oscillation.

Chapter 11 deals with interactions of eddies with the mean flow. We begin with the original "non-interaction theorem" of Eliassen and Palm (1961), as applied to gravity waves excited by flow over mountains. This is followed by a brief discussion of the importance of gravity-wave drag for the global circulation. We then turn to the quasi-geostrophic wave equation, and its use by Charney, Drazin, Matsuno and others to interpret the interactions of Rossby Waves with the zonally averaged circulation. This leads to a discussion of sudden

stratospheric warmings.

Next we discuss the poleward and upward fluxes of sensible heat and momentum associated with winter storms. This leads to a discussion of the Eliassen-Palm Theorem as it relates to balanced flows. The theorem is developed first in pressure coordinates. We then show the additional insights and greater simplicity that come from an analysis in isentropic coordinates, including the relationship between the divergence of the Eliassen-Palm flux and the flux of potential vorticity. The chapter closes with discussions of the Quasi-Biennial Oscillation, blocking, and the Brewer-Dobson circulation (Butchart, 2014) as additional examples of the interactions between eddies and the zonally averaged circulation.

Chapter 12 discusses the global circulation as a kind of large-scale turbulence, starting with a discussion of what turbulence is, framed in terms of vorticity dynamics. We discuss the very different flows of energy between scales in two-dimensional and three-dimensional turbulence, and connect it with a description of the distribution of atmospheric kinetic energy with spatial scale. We then discuss mechanisms that allow dissipation of enstrophy (squared vorticity) without dissipation of kinetic energy. This is followed by a discussion of mixing along isentropic surfaces.

Next, we discuss the predictability of the weather in a chaotic circulation regime. Finally, we explain how climate prediction differs from weather prediction.

The closing chapter briefly summarizes current trends and projected future changes in the global circulation due to increasing concentrations of atmospheric greenhouse gases.

As outlined above, the study of the thermally driven global circulation of the atmosphere brings together concepts from all areas of atmospheric science. We will touch on large-scale dynamics, convection, turbulence, cloud processes, and radiative transfer, with an emphasis on their interactions. Often these various topics are presented as if they were somehow neatly separated from each other. This book will help you to see how they fit together.

Because the circulation is global and spans all seasons, it brings together the concepts of atmospheric science across a very wide range of conditions and contexts. For example, surface friction occurs *everywhere*: over the convectively disturbed tropical oceans, in the chaotic storm track north of Antarctica, over the Himalayan mountains, and in the leafy canopies of the tropical jungles. Unfortunately, however, our understanding of boundary-layer meteorology is mostly applicable only to relatively simple, horizontally uniform conditions, such as might be encountered on a quiet summer morning in Kansas or in a stratocumulus-capped boundary layer over the subtropical oceans. When we try to understand the global circulation, we are forced to confront these and many more limitations of our understanding. This makes the study of the global circulation a particularly challenging and exciting field – as you are about to see for yourselves.

Chapter 2

What Makes It Go?

2.1 The Earth's radiation budget: An "upper boundary condition" on the global circulation

Radiation is (almost) the only mechanism by which the Earth can exchange energy with the rest of the Universe[1]. The most important upper boundary condition on the global circulation of the atmosphere is the incident solar radiation, also called the insolation. The insolation varies with geographical location, and with time. It is determined by the energy output of the Sun, the spherical geometry of the Earth itself, and the geometry of the Earth's orbit (see Fig. 2.1), which can be described in terms of the obliquity (the angle that the Earth's axis of rotation makes with the plane of the Earth's orbit around the sun), the eccentricity (a measure of the degree to with the shape of the Earth's orbit differs from a perfect circle), and the dates of the equinoxes. These all vary over geologic time (e.g., Crowley and North, 1991).

The solar energy flux at the mean radius of the Earth's orbit is about 1365 W m^{-2}. One way to get an intuitive grasp of this number is to imagine fourteen 100-Watt light bulbs per square meter. Another is to consider that 1365 W m^{-2} is equivalent to 1.365 GW km^{-2}, which is the energy output of a large power plant for each square kilometer of area normal to the solar beam.

The globally averaged top-of-the-atmosphere radiation budget is summarized in Table 2.1. The numbers given in the table are now known to three significant digits. The Earth's albedo is near 0.30, independent of season; this number has been known to better than 10 per cent accuracy only since the 1970s. The energy absorbed by the Earth is given by

[1] The other mechanisms are gravitational tides, and the exchanges of mass across the top of the atmosphere, including dust and larger meteors falling in, and the (fortunately) very slow escape of atmospheric mass to space.

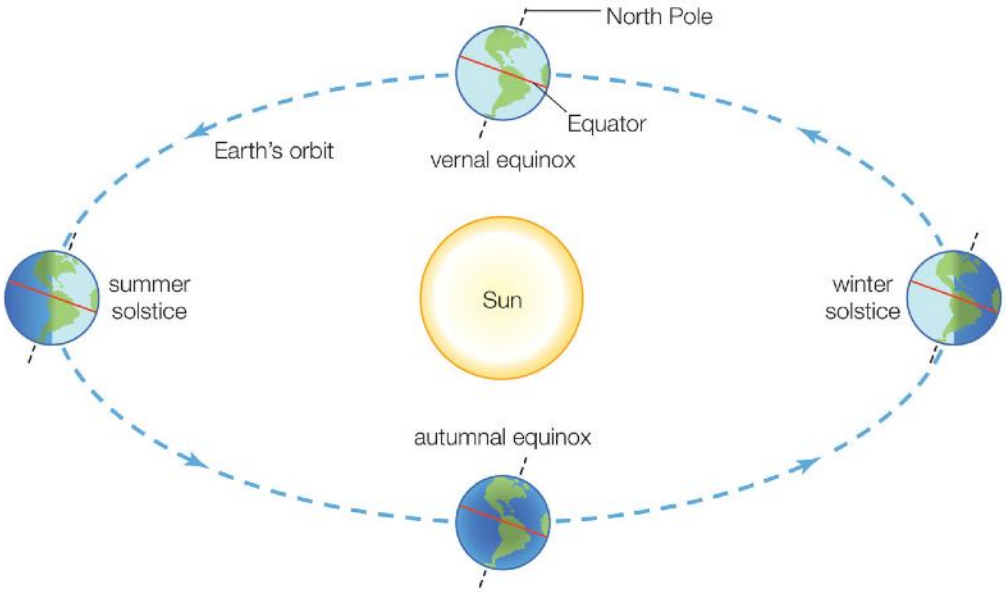

Figure 2.1: March of the seasons. As the tilted Earth revolves around the sun, changes in the distribution of sunlight cause the succession of seasons. From https://dept.astro.lsa.umich.edu/ugactivities/Labs/seasons/SeasonsIntrotroppics.html.

$$\begin{aligned} S_{abs} &= S\left(\frac{\pi a^2}{4\pi a^2}\right)(1-\alpha) \\ &= \frac{1}{4}S(1-\alpha)\ . \end{aligned} \tag{2.1}$$

Here S_{abs} is the globally averaged absorbed solar energy per unit area (given in Table 2.1), S is the globally averaged insolation, a is the radius of the Earth, and α is the planetary albedo. The global average used to compute S includes the zeroes on the night-side of the Earth. That is why S is multiplied by πa^2, the area of the absorbing disk, and divided by $4\pi a^2$, the area of the sphere.

As a matter of common experience, the insolation varies both diurnally and seasonally. At a given moment, it also varies strongly with longitude. Because a year is much longer than a day, the *daily-mean* insolation is (almost) independent of longitude, but it varies strongly with latitude in a way that depends on the season, as summarized in Fig. 2.2. As we move from the solar Equator (i.e., the latitude immediately "under" the Sun) to the summer pole, the insolation initially decreases, because at a given local time (e.g., local noon) the sun appears to be lower in the sky. On the other hand, the length of day increases at high latitudes in summer, and this tends to make the daily-mean insolation increase. Near the poles, the length-of-day effect dominates, so that at high latitudes in summer the insolation actually increases towards the pole. That is why there is a minimum of the

Table 2.1: Summary of the annually averaged top-of-the-atmosphere radiation budget, after Trenberth et al. (2009).

Incident solar radiation	341 W m^{-2}
Absorbed solar radiation	239 W m^{-2}
Planetary albedo	0.30
Outgoing longwave radation	239 W m^{-2}

insolation about 23° away from the pole in the summer hemisphere, as shown in the figure.

Notice that the region of insolation stronger than 500 W m^{-2} (in high latitudes of the summer hemisphere) is larger in January than in July. The reason is that, in the present era, the Earth is closer to the Sun in January than in July. The globally averaged insolation is actually about 7% larger in January than in July. The orbit of Mars is more eccentric; as a result, the globally averaged Martian insolation varies seasonally by about 31 %.

Seasonal and, to a lesser extent, diurnal cycles are clearly evident in the circulation patterns. Around the time of the solstices, no insolation at all occurs near the winter pole (the polar night), but at the same time, near the summer pole, the daily mean insolation is very strong despite low sun angles, simply because the sun never sets (the polar day). As is well known, these effects arise from the sun-Earth geometry shown in Fig. 2.1. In addition, the distance from the sun to the Earth varies slightly with time of year, resulting in a few percent more globally averaged insolation in January than in July, in the current epoch. The month of maximum insolation varies over geologic time. According to the widely accepted astronomical theory of the ice ages, extensive glaciation is favored when the minimum insolation occurs during the Northern Hemisphere summer, because the Northern Hemisphere contains about twice as much land as the Southern Hemisphere (e.g., Crowley and North, 1991).

The Earth emits about as much infrared radiation as required to balance the absorbed solar radiation; both energy flows are at the rate of about 240 W m^{-2}. This near balance has been directly confirmed by analysis of satellite data. The balance is observed to hold within one Watt per square meter, which is comparable to the uncertainty of the measurements. The actual annual-mean imbalance is thought to be about 0.5 W m^{-2} (Loeb et al., 2012; Trenberth et al., 2014).

Fig. 2.3 shows aspects of the Earth's radiation budget as observed from satellites (Wielicki et al., 1998). As discussed above, the zonally averaged incident (i.e., incoming) solar radiation at the top of the atmosphere varies seasonally as the Earth orbits the sun. The zonally averaged albedo, which is the fraction of the zonally averaged incident radiation that is reflected back to space, is highest near the poles, due to cloudiness as

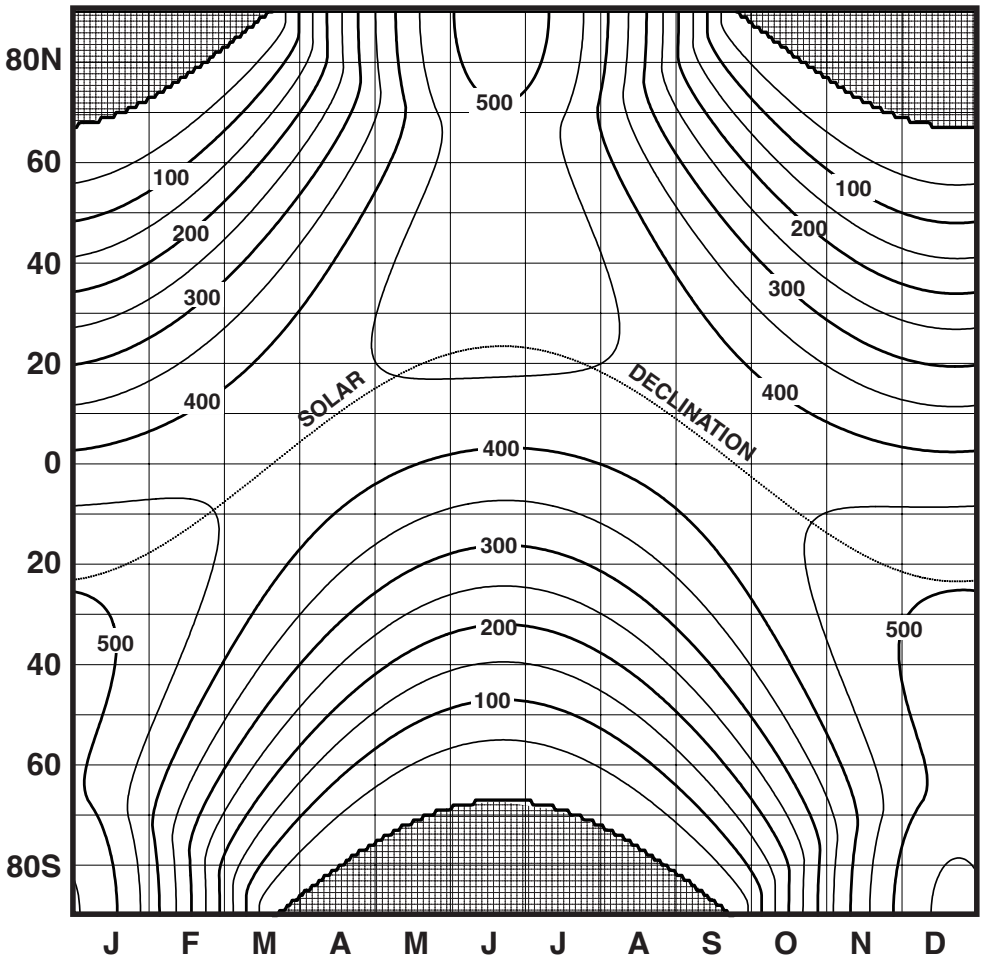

Figure 2.2: The seasonal variation of the zonally (or diurnally) averaged insolation at the top of the atmosphere. The units are W m^{-2}.

well as snow and ice. It tends to have a weak secondary maximum in the tropics, associated with high cloudiness there. The zonally averaged terrestrial radiation at the top of the atmosphere, also called the outgoing longwave radiation or OLR, has its maxima in the subtropics. It is relatively small over the cold poles, but it also has a minimum in the warm tropics, due to the trapping of terrestrial radiation by the cold, high tropical clouds, and by water vapor.

The net radiation at the top of the atmosphere, which is the difference between the absorbed solar radiation and the OLR, is positive in the tropics and negative in higher latitudes. This implies that energy is transported poleward somehow, inside the system. A portion of the energy is transported by the atmosphere, and the rest is transported by the oceans.

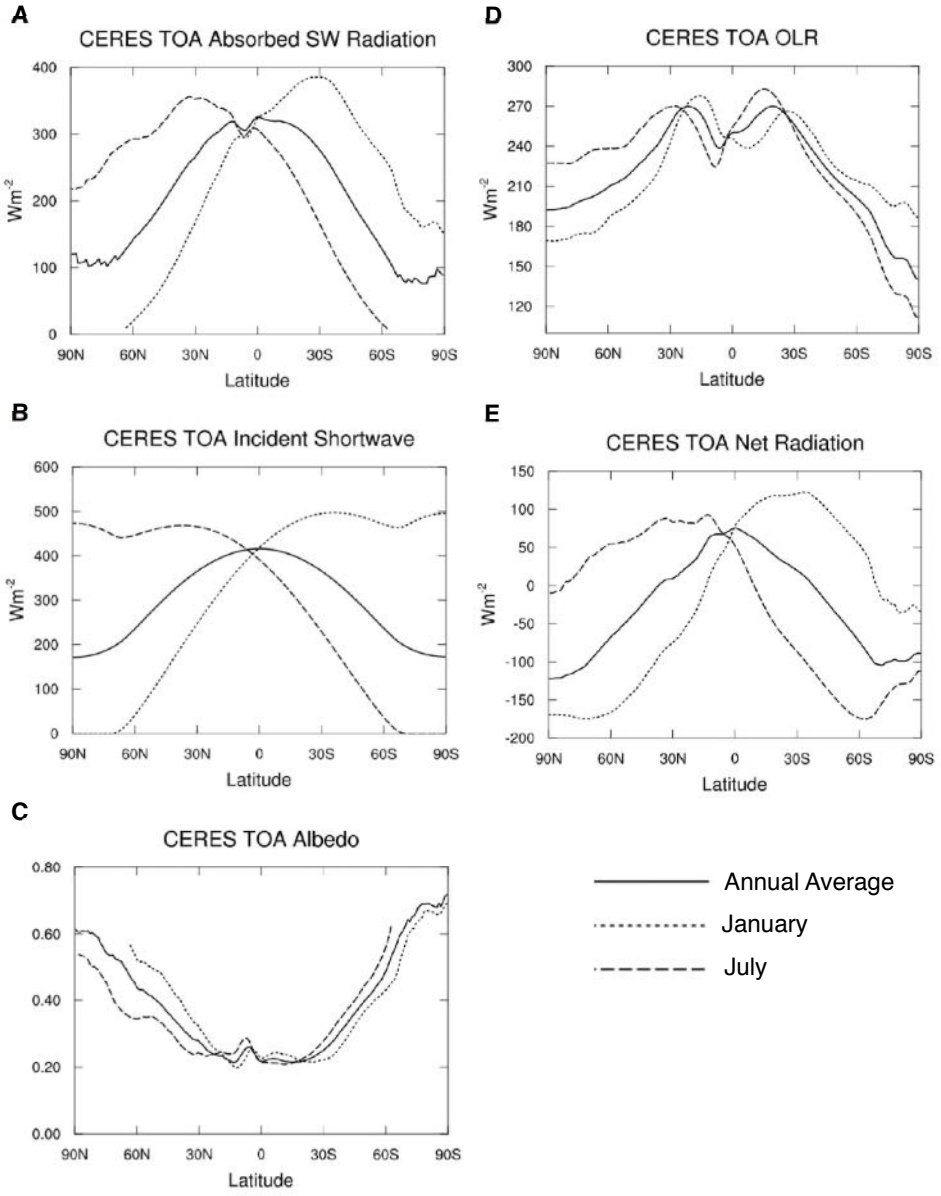

Figure 2.3: The zonally averaged A) absorbed solar radiation at the top of the atmosphere, B) incident solar radiation, C) albedo, D) outgoing longwave radiation (OLR), and E) net radiation at the top of the atmosphere, as observed using satellites in a project called “Clouds and the Earth’s Radiant Energy System” (CERES; Wielicki et al., 1998).

2.2 Meridional energy transports by the atmosphere-ocean system

Considering the energy balance of the atmosphere-ocean system, the variation with latitude of the long-term average net radiation at the top of the atmosphere implies energy transports

inside the system. These transports are produced by the circulations of both the atmosphere and the oceans, and it is tempting to regard the global circulations of the atmosphere and oceans as a "response" to this pattern of net radiation. An important point, however, is that the distributions of the albedo and the outgoing longwave radiation are determined in part by the circulation itself. It is an egregious oversimplification to regard the net radiation at the top of the atmosphere as an "external" forcing function.

Consider the energy budget of a column which extends from the center of the Earth to the "top of the atmosphere:"

$$\frac{\partial E}{\partial t} = N_\infty - \nabla \cdot \mathbf{G}_\infty \, . \tag{2.2}$$

Here E is the energy per unit area stored in the column; t is time; and N_∞ is the net downward flux of energy at the top of the atmosphere, which is entirely due to radiation. The dimensions of N_∞ are energy per unit time per unit area (e.g., W m^{-2}). The energy transport, $\mathbf{G}_\infty$, represents the movement of energy, in the zonal and meridional directions, due to both the winds and the ocean currents. It is a vector with both zonal and meridional components, and it has dimensions of energy per unit length per unit time (e.g., W m^{-1}). The subscript ∞ on $\mathbf{G}_\infty$ signifies that it includes energy transports in all parts of the Earth system, from the center of the Earth out to space.

Suppose that we average over a time interval Δt:

$$\frac{E(t+\Delta t) - E(t)}{\Delta t} = \overline{N_\infty}^t - \nabla \cdot \overline{\mathbf{G}_\infty}^t \, . \tag{2.3}$$

Here $\overline{(.)}^t$ represents a time average; this is a notation that we will use throughout the book. Because the Earth is close to energy balance, $E(t+\Delta t)$ and $E(t)$ cannot be wildly different from each other, so the numerator on the left-hand side of (2.3) is bounded within a finite range, regardless of how large Δt is. Therefore, as Δt increases, the left-hand side of (2.3) decreases in absolute value, and eventually becomes negligible compared to the individual terms on the right-hand side. The physical meaning is that energy storage inside the Earth system can be neglected if the time-averaging interval is long enough; here the minimum interval would be one year, but ideally the average should be taken over many years. When we apply such a time average, the net radiation across the top of the column must be balanced by transports inside; this can be written as

$$\nabla \cdot \overline{\mathbf{G}_\infty}^t = \overline{N_\infty}^t \, . \tag{2.4}$$

The global mean of $\nabla \cdot \mathbf{G}_\infty$ must be exactly zero, not just in a time average, but at each instant. The reason is purely mathematical, rather than physical: the global mean of the divergence of any vector is zero. You are asked to prove that in Problem 1 at the end of this chapter. The only way that (2.4) can be true is if the global mean of $\overline{N_\infty}^t$ is equal to zero, i.e., if the Earth is in energy balance. To the extent that this is not true, the left-hand side of (2.3) is not negligible.

We now break $\mathbf{G}_\infty$ into its zonal and meridional components, i.e.,

$$\mathbf{G}_\infty = (G_\infty)_\lambda \mathbf{e}_\lambda + (G_\infty)_\varphi \mathbf{e}_\varphi \; . \tag{2.5}$$

Here λ and φ represent longitude and latitude, respectively, and $\mathbf{e}_\lambda$ and $\mathbf{e}_\varphi$ are unit vectors pointing towards the east and north, respectively. We expand the divergence operator in spherical coordinates (see Appendix A) as follows:

$$\nabla \cdot \mathbf{G}_\infty = \frac{1}{a\cos\varphi}\frac{\partial (G_\infty)_\lambda}{\partial \lambda} + \frac{1}{a\cos\varphi}\frac{\partial}{\partial \varphi}\left[(G_\infty)_\varphi \cos\varphi\right] \; . \tag{2.6}$$

Here a is the radius of the Earth.[2] Multiply both sides of (2.6) by $a\cos\varphi$ and integrate over all longitudes to obtain

$$\begin{aligned} \int_0^{2\pi} (\nabla \cdot \overline{\mathbf{G}_\infty}^t)\, a\cos\varphi d\lambda &= 2\pi \frac{\partial}{\partial \varphi}\left[\overline{(G_\infty)_\varphi}^{\lambda,t} \cos\varphi\right] \\ &= 2\pi a \overline{N_\infty}^{\lambda,t} a\cos\varphi \quad . \end{aligned} \tag{2.7}$$

Here we use the notation $\overline{(.)}^\lambda \equiv \frac{1}{2\pi}\int_0^{2\pi}()\,d\lambda$ to denote a zonal mean; the combination of a time average and a zonal mean can be denoted by either $\overline{(.)}^{\lambda,t}$ or $\overline{(.)}^{t,\lambda}$. In (2.7), the zonal derivative has dropped out as a result of the integration with respect to longitude. The second line of (2.7) comes by comparison with (2.4).

Eq. (2.7) gives us a way to compute the meridional derivative of the poleward energy transport, i.e., $\frac{\partial}{\partial \varphi}\left[\overline{(G_\infty)_\varphi}^{\lambda,t} \cos\varphi\right]$, in terms of $\overline{N_\infty}^{\lambda,t}$. What we really want, however, is a

[2] Strictly speaking, a should be the radial distance from the center of the Earth to the "top of the atmosphere," but that is approximately the same as the radius of the Earth because the Earth's atmosphere is sufficiently shallow. This is an example of what is called the "thin atmosphere approximation," which will be discussed further in Chapter 4.

formula for the poleward energy transport itself, rather than its divergence. To get this, we multiply (2.7) by a, and integrate with respect to latitude, from the South Pole ($\varphi = -\pi/2$) to an arbitrary latitude φ, to obtain

$$\overline{\Theta}^t(\varphi) = 2\pi a^2 \int_{-\pi/2}^{\varphi} \overline{N_\infty}^{\lambda,t} \cos\varphi' \, d\varphi' \,, \tag{2.8}$$

where we define

$$\Theta(\varphi) \equiv 2\pi a \cos\varphi \overline{(G_\infty)}_\varphi^\lambda \,, \tag{2.9}$$

and we have used the boundary condition

$$\Theta(-\pi/2) = 0 \,. \tag{2.10}$$

The dimensions of $\Theta(\varphi)$ are energy per unit time, e.g., Watts. The boundary condition (2.10) is exact; if it were not true, a finite amount of energy per unit time would be flowing into or out of the South Pole, which is a "point" of zero mass. A similar condition must apply at the North Pole. The right-hand side of (2.8) is the area integral of $\overline{N_\infty}^t$ over the "south polar cap" that extends from the South Pole up to latitude φ. When the upper limit of meridional integration in (2.8) is set to $\pi/2$, the right-hand side of (2.8) reduces to the global mean of $\overline{N_\infty}^t$. But since $\Theta(\pi/2)$ must be equal to zero, it follows that the global mean of $\overline{N_\infty}^t$ is zero.

Fig. 2.4 gives a plot of $\Theta(\varphi)$, computed by using (2.9), with values of based on satellite data from a project called CERES (Wielicki et al., 1996, 1998). A poleward energy transport is clearly apparent in both hemispheres. The curve of the transport has a pleasingly simple shape, roughly like $\sin(2\varphi)$. VonderHaar and Oort (1973) were the first to diagnose $\Theta(\varphi)$ from satellite measurements of the Earth's radiation budget. The maximum absolute values in middle latitudes of both hemispheres are on the order of 6 PW (a PetaWatt is 10^{15} Joules per second). Because this total energy transport by the climate system can be inferred directly from satellite measurements of the Earth's radiation budget, it is known with relatively good accuracy now.

Fig. 2.4 shows that that $\overline{\Theta}^t(\varphi)$ is exactly zero at both poles. We built that in for the South Pole, by using (2.10), but what makes $\overline{\Theta}^t(\varphi)$ miraculously return to zero at the North

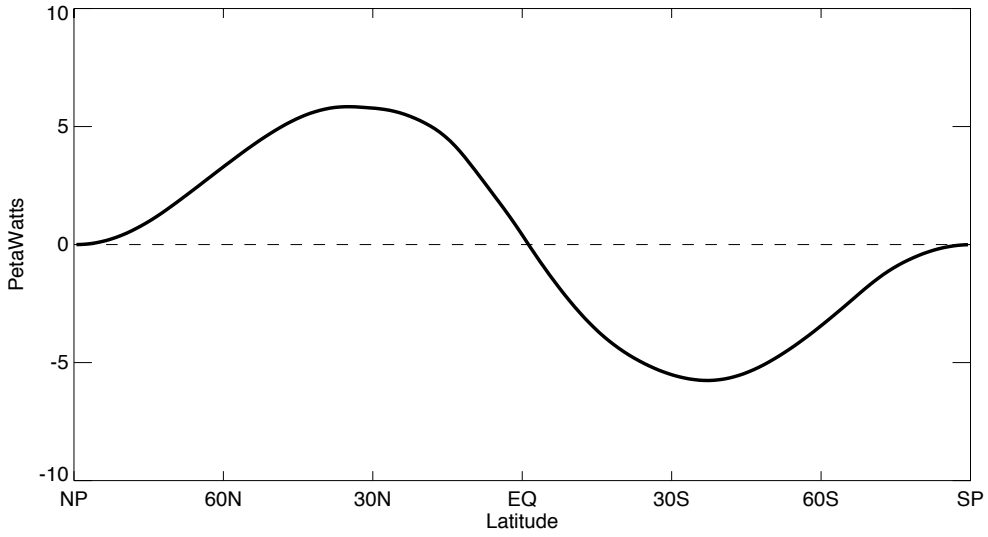

Figure 2.4: The annually averaged northward energy transport by the atmosphere and ocean combined, $\overline{\Theta}^t(\varphi)$, as inferred from the observed annually averaged net radiation at the top of the atmosphere using (2.9). A Petawatt is 10^{15} W. The plot was created using CERES data.

Pole? The answer is that we have forced it to be zero at the North Pole, by "correcting" the data. The observations show that the global mean of N_∞ is small compared to the local values. It is zero within the uncertainty of the measurements, but of course it is not exactly zero. Before computing $\overline{\Theta}^t(\varphi)$ from (2.9), we apply a small, globally uniform correction to N_∞, such that after the correction the global mean of N_∞ is exactly zero. As can be seen from (2.9), this is sufficient to ensure that $\overline{\Theta}^t(\varphi)$ is zero at the North Pole.

The value of N_∞ is is not exactly zero for several reasons:

- The Earth is not in perfect energy balance. As mentioned earlier, observations suggest that the global mean of N_∞ is about 0.5 W m^{-2} (Loeb et al., 2012; Trenberth et al., 2014).
- The data has been averaged over just a few decades, so even if the long-term global mean of N_∞ was exactly zero, the time derivative term of (2.2) might not be not completely negligible.
- The data are not perfectly accurate.

We can say that the "job" of the global circulations of the atmosphere and oceans is to carry out the meridional energy transport shown in Fig. 2.4. If the transport of energy from place to place by the atmosphere and oceans could somehow be prevented, then each part of the Earth would have to come into local energy balance, by adjusting its temperature, water vapor, and cloudiness so that the outgoing longwave radiation locally balanced the absorbed solar radiation. Such a hypothetical state is referred to as "radiative-convective

equilibrium;" modeling studies of radiative-convective equilibrium are discussed in Chapter 8. Radiative-convective equilibrium would presumably entail much warmer temperatures in the tropics, and much colder temperatures at the poles. The global circulation of the atmosphere and oceans has a moderating effect on the global distribution of temperature, tending to warm the higher latitudes and cool the tropics. As discussed in Chapter 7, these same thermal contrasts represent a source of energy (called "available potential energy") that makes the global circulations of the atmosphere and oceans possible.

If we consider that the global circulation of the atmosphere exists in order to produce the energy transports shown in Fig. 2.4, then we can imagine that the "strength of the circulation," as measured for example by its total kinetic energy, is determined by the magnitude of the required energy transports.

Much further discussion of the observations and theory of energy transports by the atmosphere and oceans is given later in this book.

2.3 Surface boundary conditions

The the global atmospheric circulation is strongly affected by the properties of the Earth's surface, and their geographical variations. The most important properties of the Earth's surface are as follows:

2.3.1 Temperature

The temperature of the Earth's surface varies strongly and rapidly over land, and considerably less over the oceans. The reason for this difference between land and sea will be discussed below, in the subsection on the surface heat capacity.

The oceans cover about two thirds of the Earth's surface. Their average depth is about 4 km. Water is heavy stuff; the mass of 1 m^3 of water is 10^3 kg. The mass of the oceans is about 1.3 x 10^{21} kg. For comparison, the mass of the atmosphere is about 250 times less, roughly 5 x 10^{18} kg.

Not only is water dense, it has a very high specific heat: about 4200. In contrast, the specific heat of air (at constant pressure) is a little less than a quarter of that, i.e., 1000. The total heat capacity of the oceans is thus about 1000 times larger (250 x 4) than the total heat capacity of the atmosphere. When the oceans say "Jump," the atmosphere says "How high?"

The density of the atmosphere decreases exponentially upward with height, and can change by 10 per cent or so in the course of a year, at a given location, due to changes in temperature and pressure. In contrast, the density of sea water varies by only a few percent throughout the entire ocean; it is a complex but fairly weak function of temperature, salinity, and pressure. Because of the near-incompressibility of water, pressure effects (called "thermobaric" effects) are relatively unimportant; variations of the density are mainly due

to changes in temperature and salinity. Warmer and fresher water is less dense and tends to float on top; colder and saltier water is more dense and tends to sink. Surface cooling and evaporation create dense water; surface heating and precipitation create light water. Note that the properties of the water are altered mainly near the surface; below the top hundred meters or so, the properties of water parcels remain nearly invariant, even over decades or centuries.

In the study of the atmosphere, we often treat the sea-surface temperature (SST) as a seasonally varying lower boundary condition. Fig. 2.5 shows the observed distributions of the SST for January and July. Note the warm currents off the east coasts of North America and Asia, and the cold currents off all west coasts. The warm SSTs, at a particular latitude, are generally associated with poleward currents; the two best-known of these are the Gulf Stream and the Kuroshio. The colder SSTs are generally associated with either equatorward flow (as for example in the case of the California current) or with upwelling (again, in the region of the California current, and also along the Equator in the eastern Pacific).

As discussed in Chapter 9, the pattern of upwelling is very closely related to the low-level winds, and at the same time the low-level winds are strongly tied to the spatial distribution of the SST. The seasonal change of the SST is largest in the Northern Hemisphere, particularly on the western sides of the ocean basins. Note that the seasonal forcing is capable of changing the SSTs by tens of degrees in some middle and high latitude locations. The depth to which this seasonal change penetrates is of course variable, but is typically on the order of 100 m. Of course, the temperature of the water at great depth undergoes virtually no seasonal change. In the study of the global atmospheric circulation we often consider the spatial and seasonal distribution of the SST to be "given," but of course in reality it is determined in part by what the atmosphere is doing, or rather what the atmosphere has been doing over time. For example, the distribution of cloudiness strongly affects the flow of solar radiation into the upper ocean, and over time this can tend to reduce the SST where clouds are prevalent and the solar insolation at the top of the atmosphere is strong, relative to what the SST would be if the cloudiness were somehow prevented from occurring. The role of clouds in determining the distribution of the SST is a major complication hindering our understanding of the atmosphere and ocean as a coupled system.

2.3.2 Wetness

One of the most important properties of the Earth's surface is that roughly 70 per cent of it is permanently wet, and so represents a huge source of moisture. The vapor pressure immediately above a wet surface, called the "saturation vapor pressure," is a strong function of temperature only. It is approximately given by

$$e_{sat}(T) \cong 6.11 \exp\left[\frac{L}{R_v}\left(\frac{1}{273}-\frac{1}{T}\right)\right] \quad \text{hPa}\,, \tag{2.11}$$

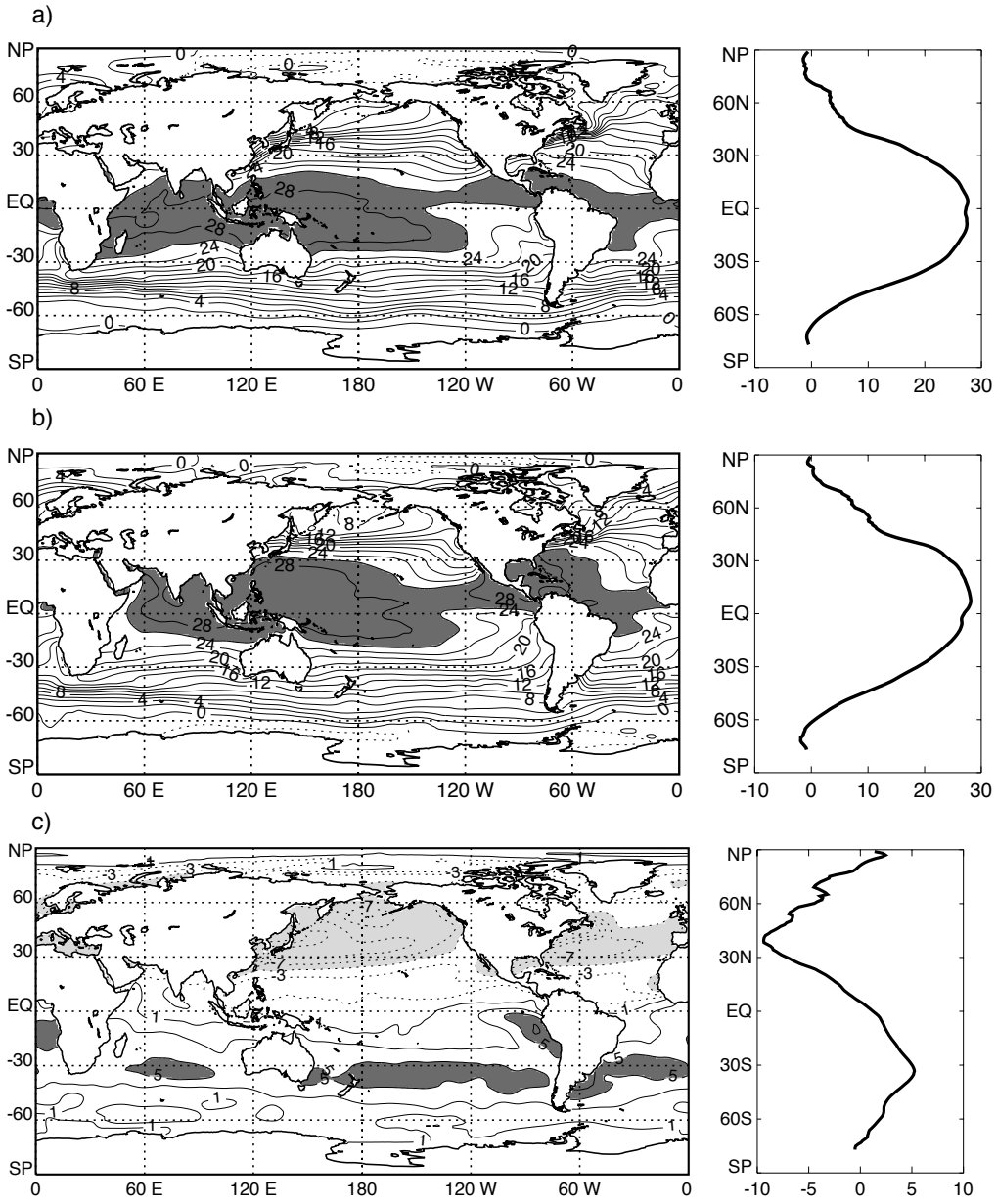

Figure 2.5: a) SST distribution for January. The contour interval is 2°C, with shading for values higher than 28° C. b) Same for July. c) SST difference between March and September, with light shading for values below -5° C and dark shading for values above 5°C. In each panel, zonal means are shown on the right.

where the temperature is given in K, $L = 2.52$ x 10^6 J kg^{-1} is the latent heat of water vapor, and = 461 J K^{-1} kg^{-1} is the gas constant for water vapor. The enormous value of the latent heat of water vapor is one of the reasons why moisture strongly influences the Earth's climate and the global circulation of the atmosphere. The strong temperature-

dependence of is shown in Fig. 2.6. Held and Soden (2006) pointed out that for typical surface temperatures, the rate of increase is a spectacular 7% per Kelvin. Fig. 2.7 shows the geographical variation of based on the SSTs plotted in Fig. 2.5. As discussed later, near the surface over the oceans the actual vapor pressure of the air, i.e., the partial pressure of water vapor, "tries" to be , but usually falls short by 20% or so. At any rate, the "effective wetness" of the ocean increases rapidly with the SST. The largest values of occur in the tropics, of course, and are close to 40 hPa. In those very humid regions, about 4% of the near-surface air is water vapor.

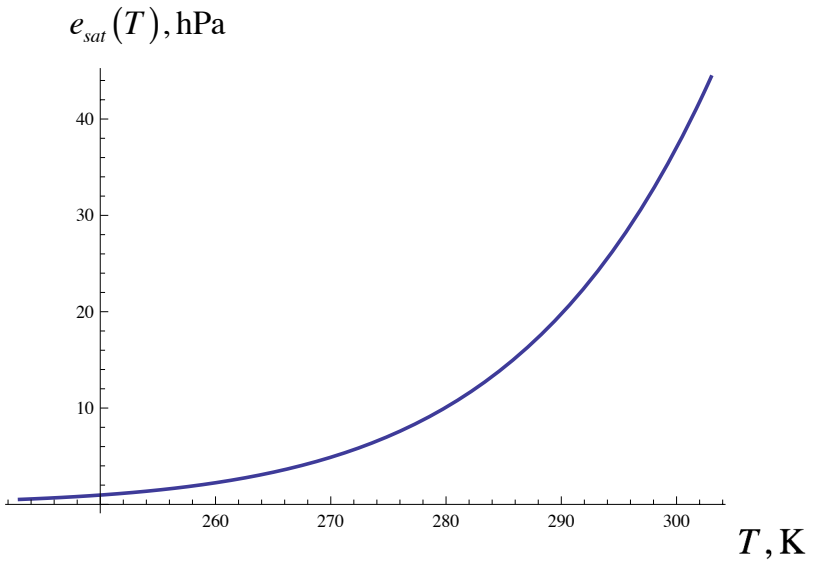

Figure 2.6: The saturation vapor pressure, e_{sat}, as a function of temperature.

The availability of land-surface moisture to the atmosphere is much more complicated, and is discussed separately below.

2.3.3 Topography

You will not be surprised to hear that mountains have a strong effect on the global atmospheric circulation. Fig. 2.8 shows the locations of the Earth's mountain ranges. Mountains block the wind; this can be called a mechanical forcing. The air can flow around a mountainous obstacle, or it can flow over. Which actually happens depends in part on the scale of motion. The distribution of surface pressure across a mountain range can exert a net force on the solid Earth, and an equal and opposite net force on the atmosphere. Chapter 6 explains how this works.

Mountains can also exert a thermal forcing on the atmosphere, because the surface of a mountain can have a temperature quite different from that of the surrounding air at the same height. For example, during the northern summer the Tibetan plateau produces a "warm spot" in the middle troposphere, and this represents an important aspect of the thermal

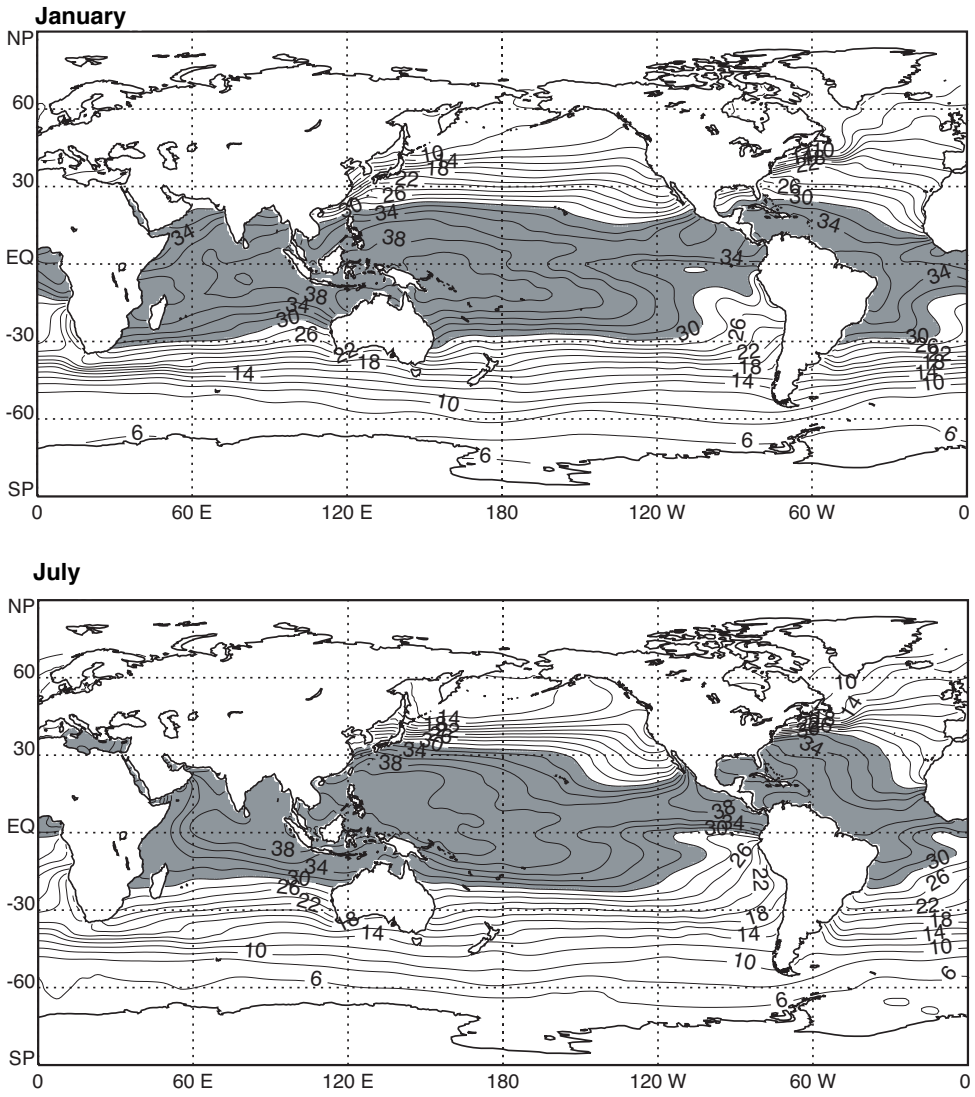

Figure 2.7: The geographical pattern of e_{sat} based on the SSTs shown in Fig. 2.5. The contour interval is 2 hPa. Values larger than 30 hPa are shaded.

forcing that produces the Indian summer monsoon. Further discussion is given in Chapter 9.

Finally, mountains strongly influence the geographical distribution of precipitation. Rain and snow are enhanced where topography forces the air to flow uphill, and also where surface heating on sunlit slopes promotes moist convection. On the other hand, precipitation is often reduced on the downstream side of mountainous regions, because the air tends

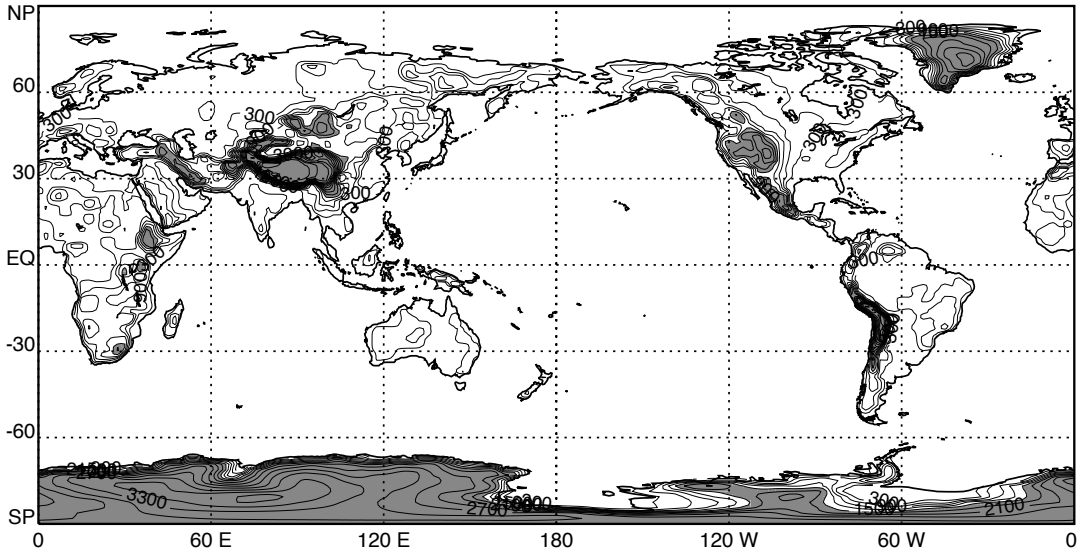

Figure 2.8: The Earth's orography, averaged onto a mesh with a grid spacing of 1° of longitude by 1° of latitude. The contour interval is 300 m. Values higher than 1500 m are shaded.

to be sinking there, and also because the moisture content of the air can be depleted by upstream precipitation maxima.

2.3.4 Heat capacity

The heat capacity of the Earth's surface is the amount of energy needed to change the "skin temperature" of the surface by a given amount. Here the skin temperature, T_S, is defined as the temperature of an equivalent black body that would emit infrared radiation at a rate equal to the actual infrared emission by the Earth's surface. The heat capacity is highly variable in space, and also varies somewhat less dramatically with time. The concept of heat capacity sounds simple, but it is actually somewhat subtle. The time change of the skin temperature satisfies an equation very similar to (2.2), i.e.,

$$C\frac{\partial T_S}{\partial t} = N_S - \nabla \cdot \mathbf{G}_S \tag{2.12}$$

Here C is the heat capacity of the surface, N_S is the net downward energy flux at the Earth's surface (due to radiation and other processes discussed later), and $\mathbf{G}_S$ is the horizontal energy transport "inside" the Earth's surface. For the land, we can assume that $\mathbf{G}_S = 0$, but for the oceans we expect that energy transport by currents will lead to $\mathbf{G}_S \neq 0$. The heat capacity, C, depends on the composition of the material both at and below the surface, because energy flowing into the surface can be stored through a finite depth. It also depends on the speed with which energy is transported down into the material below the surface.

In general, the oceans have very high heat capacity. The geographical distribution of SST does fluctuate seasonally, however, and varies considerably with both longitude and latitude, as shown in Fig. 2.5.

The land-surface has a much smaller heat capacity. This implies that the net surface energy flux averages to nearly zero over land, even for a single day. To understand why, note that with $C \to 0$ and $\mathbf{G}_S = 0$ (appropriate for land), Eq. (2.12) implies that $N_S = 0$. For the ocean, with large values of C, daily mean values of N_S can be much larger. The large heat capacity of the ocean means that the SST changes slowly, because

$$\frac{\partial T_S}{\partial t} = \frac{N_S - \nabla \cdot \mathbf{G}_S}{C} \tag{2.13}$$

i.e., a large value of C in the denominator on the right-hand side of (2.13) reduces $\partial T_S/\partial t$ for a given value of $N_S - \nabla \cdot \mathbf{G}_S$. Because of this, for some purposes, e.g., short-range weather forecasts, the SST can be considered a "fixed" lower boundary condition on the atmosphere.

2.3.5 Albedo

The degree to which the surface reflects solar radiation obviously affects its response to the sun. The surface albedo depends on surface composition and sun angle, among other things. The ocean has an albedo close to 0.06 when the sun is high in the sky, i.e., it is quite dark. At low sun angles, however, the ocean can reflect considerably more of the incident solar radiation. The albedo of the land surface varies widely, due to differing compositions of the soil or rock at the surface, differing types and amounts of vegetation cover (discussed further below), and of course the presence or absence of snow.

2.3.6 Roughness

"Rough" surfaces exert a drag on the wind more readily than smooth ones. The surface roughness is another example of a lower boundary condition that is at least partially mechanical in nature. The ocean is relatively smooth, depending on the wind speed, and presents little "roughness" to stimulate momentum exchange with the atmosphere. The land surface is much rougher than the ocean.

2.3.7 Vegetation

The vegetation on the land-surface regulates the flow of moisture from the soil, as discussed further below. It also affects both the roughness and albedo of the surface. The pattern of vegetation on the land surface affects the atmosphere in very complicated ways. Fig. 2.9 shows a highly simplified distribution of vegetation types on the land surface, and Fig.

2.10 shows the "leaf area index," which is a measure of the greenness of the vegetation. Obviously, the type, density, and even the health of the land-surface vegetation can affect the surface albedo and surface roughness. These characteristics of the vegetation vary with season, especially in middle latitudes. They can also vary interannually. The degree to which the plants allow moisture to transpire from leaves into the atmosphere strongly regulates the surface fluxes of sensible and latent heat; strong transpiration cools the surface and reduces the sensible heat flux. Sellers et al. (1997) provide an introductory overview.

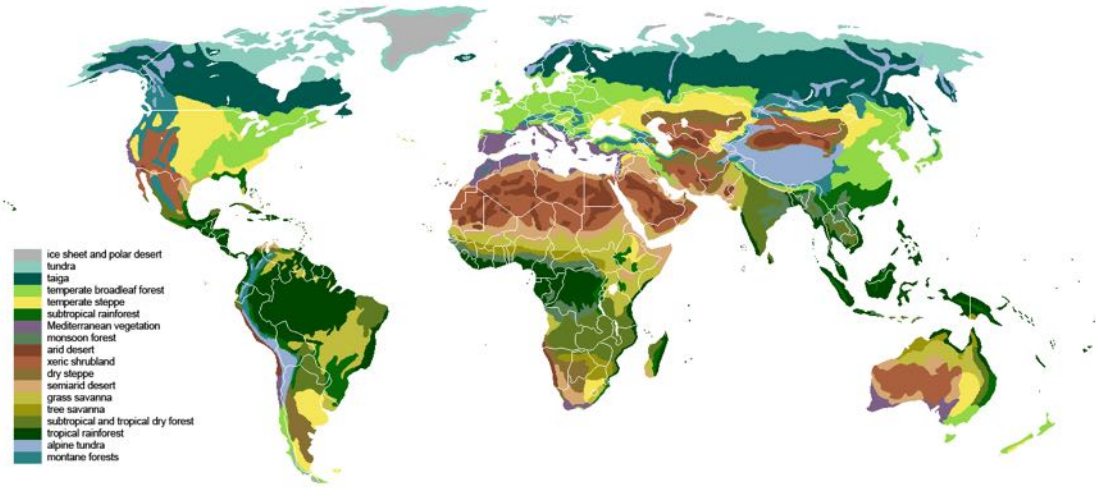

Figure 2.9: A simplified map of vegetation types on the land surface. From `https://en.wikipedia.org/wiki/Biome`.

2.3.8 Sea ice

The distribution of sea ice (Fig. 2.11) also acts as a thermal lower boundary condition. There are strong seasonal changes in ice cover in the Southern Hemisphere, but not in the Northern Hemisphere. In addition to the obvious strong effect of sea ice on the surface albedo, the ice also acts as an insulator that separates the relatively warm ocean water from the air. Because sea ice is a good insulator, its upper boundary can be much colder than the water beneath. Sea ice is also very smooth, so that little surface drag occurs for a given wind speed. Until recently, the Arctic ocean has been ice-covered all year, while the North Atlantic and the Southern Oceans have long experienced seasonal melting. Of course, the thickness of the ice also varies both geographically and seasonally, and the thickness strongly determines the insulating power of the ice. In addition, several percent of open water typically occurs, especially when the ice is thin. Some of the open water is found in cracks in the ice, called "leads." The water in the leads can be much warmer than the ice nearby, especially in winter. Under such conditions, the large-scale average sensible and latent heat fluxes can be dominated by the contributions from the leads, even though leads may cover only a few percent of the area. Snow that falls on the sea ice insulates it and

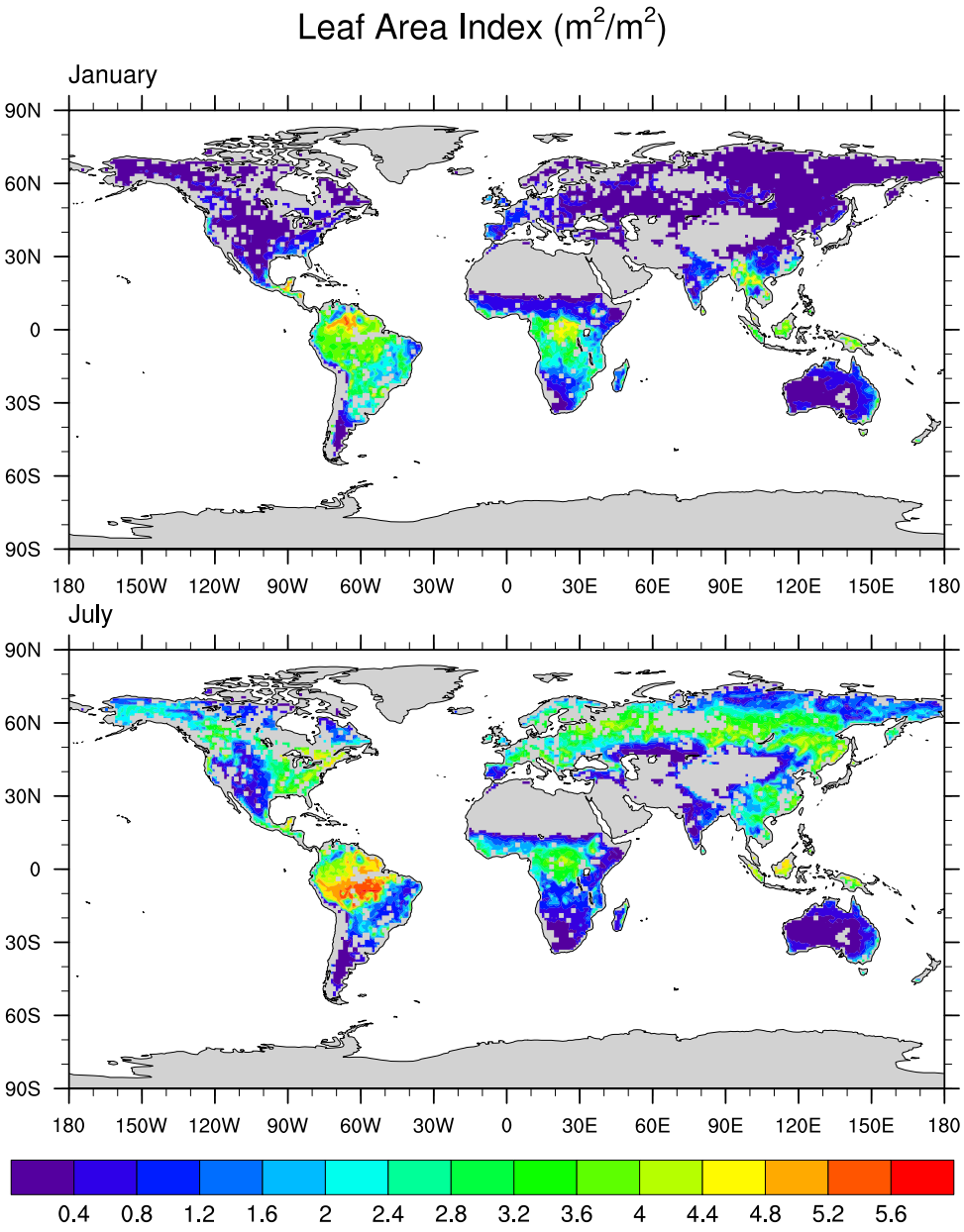

Figure 2.10: The leaf area index, a measure of greenness, for January and July. The data were obtained from https://daac.ornl.gov/VEGETATION/guides/Mean_Seasonal_LAI.html, and have been plotted with one-degree resolution.

protects it from the effects of the sun, helping to prevent the ice from melting.

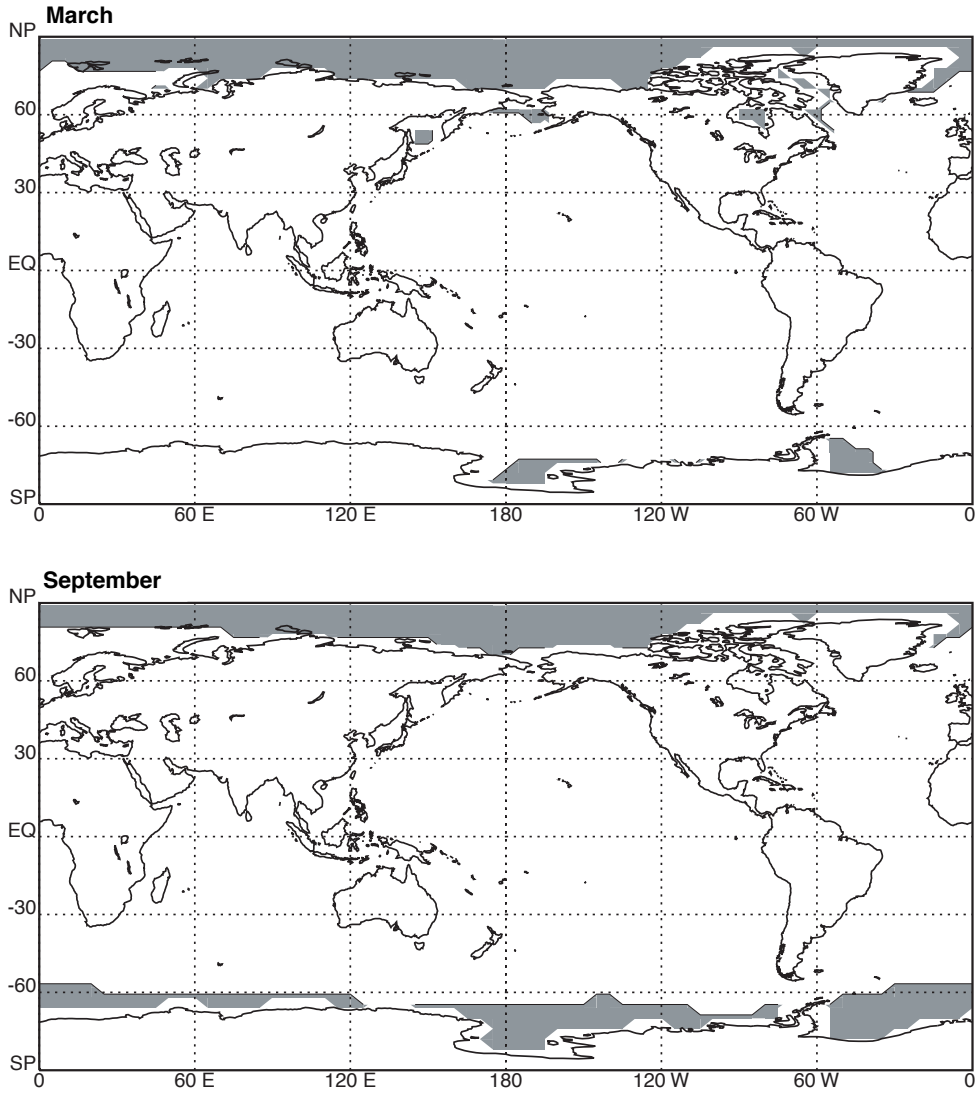

Figure 2.11: The distributions of sea ice (shown in grey) for March and September. The data represent averages for grid cells 5° of longitude wide and 4° of latitude high. The data shown here are representative of the mid 20th century. As you probably know, in more recent years, the September Arctic sea ice has been less extensive than shown here.

2.3.9 Land ice

The land-sea distribution and the locations of "permanent" (or, more accurately, non-seasonal) land ice (e.g., the ice sheets that cover Antarctica and Greenland) strongly affect the surface albedo. Over land, the geographical and seasonal variations of the surface albedo are largely determined by the distribution of vegetation, but of course they also depend on snow cover. Permanent land ice is mainly confined to Antarctica and Greenland,

in the present climate, although there are many smaller glaciers throughout the world. The Greenland and Antarctic ice sheets are thousands of meters thick in places, and so increase the effective local topographic height of the Earth's surface by substantial amounts. The distribution of land ice can vary dramatically on time scales of thousands of years and longer (e.g., Imbrie and Imbrie, 1986; Crowley and North, 1991).

2.4 Energy and moisture budgets of the surface and atmosphere

Some aspects of the global atmospheric circulation can be regarded as more or less direct responses to the various boundary conditions mentioned above. Examples include the equator-to-pole energy flux by the atmosphere, planetary waves produced by flow over mountains, and monsoons that are strongly tied to the land-sea distribution and the seasonally varying insolation. Of course, there are many additional time-dependent features of the circulation that are less directly tied to the boundary conditions, but instead arise from the internal dynamics of the atmosphere, which include winter storms, tropical cyclones, and many other things.

Table 2.2: Components of the globally and annually averaged surface energy budget, after Trenberth et al. (2009). A positive sign means that the surface is warmed.

Absorbed solar radiation	161 W m^{-2}
Downward terrestrial radiation	333 W m^{-2}
Upward terrestrial radiation	-396 W m^{-2}
Net terrestrial radiation	-63 W m^{-2}
Net radiation	98 W m^{-2}
Latent heat flux	-80 W m^{-2}
Sensible heat flux	-17 W m^{-2}

The planetary radiation budget has already been briefly discussed. We now consider the energy and moisture budgets of the Earth's surface and the atmosphere, as shown in Table 2.2. The numbers in this table are known to two significant digits. Of the 239 W m^{-2} that is absorbed by the Earth-atmosphere system, 161 W m^{-2} is absorbed by the Earth's surface. Thus only about 239 - 161 = 78 W m^{-2} of solar radiation is absorbed by the atmosphere. That is only about 1/3 of the total solar radiation absorbed by the Earth-atmosphere system. The surface receives a total ($LW\downarrow$ + SW; see the notation defined in Table 2.2) of 494 W m^{-2} of "incoming radiation. Note that $LW\downarrow$ is about twice as large as SW! This is the "greenhouse" effect on the surface energy budget. The incoming energy due to longwave

and solar radiation absorbed by the surface is given back to the atmosphere in the form of $LW\uparrow$, LH and SH. By far the largest of these is $LW\uparrow$. The oceans can transport energy from one place to another, so the energy absorbed by the oceans is not necessarily given back in the same place where it is absorbed. Also, the large heat capacity of the upper ocean allows energy storage on seasonal time scales. In contrast, the continents cannot transport energy laterally at any significant rate, and their limited heat capacity forces near energy balance, everywhere, on time scales of a few days at most. Table 2.2. shows that the net radiative heating of the surface, which amounts to 98 W m^{-2}, is balanced primarily by evaporative cooling of the surface at the rate of 80 W m^{-2}. In other words, the surface cools itself off by evaporating water.

Table 2.3: The globally and annually averaged energy budget of the atmosphere. obtained by combining the numbers in Tables 2.1 and 2.2. A positive sign means that the atmosphere is warmed.

Absorbed solar radiation	78 W m^{-2}
Net loss of terrestrial radiation	-176 W m^{-2}
Net radiative heating	-98 W m^{-2}
Latent heat input	80 W m^{-2}
Sensible heat input	17 W m^{-2}

The globally averaged energy budget of the atmosphere is shown in Table 2.3. An interpretation of Table 2.3 is that the atmosphere sheds energy through infrared radiation at the rate required to balance the various forms of energy input, and the temperature of the atmosphere adjusts to allow the necessary infrared emission. The net radiative cooling of the atmosphere, at the rate of -98 W m^{-2}, is primarily balanced by the latent energy source due to surface evaporation. Of course, the latent energy is converted into sensible heat when water vapor condenses. A fraction of the condensed water re-evaporates inside the atmosphere. The net condensation rate within the atmosphere is closely balanced by the rate of precipitation at the Earth's surface; this means that the amount of condensed water in the atmosphere is neither increasing nor decreasing with time. The rate at which evaporation introduces moisture into the atmosphere has to be balanced by the rate at which precipitation removes it. Keep in mind that these various balances apply in a globally averaged sense, rather than locally in space, and in a time-averaged sense, rather than instantaneously.

The globally averaged rate of precipitation, and the globally averaged rate of evaporation, are measures of the "speed" or intensity of the hydrologic cycle. The preceding discussion suggests a second interpretation of the atmospheric energy budget: To a first approximation, the speed of the hydrologic cycle is "determined by" the rate at which the

atmosphere is cooling radiatively. Of course, this does not mean that the geographical and temporal distributions of precipitation are determined by the corresponding distribution of radiative cooling; in fact, the local rate of precipitation tends to be negatively correlated with the local atmospheric radiative cooling, because precipitation systems produce high, cold clouds (see below) that reduce the infrared emission to space.

The local rate of precipitation is controlled mainly by dynamical processes, and the rate of evaporation from the Earth' surface is influenced by the surface wind speed. To some extent, the overall strength of the global circulation of the atmosphere is determined by, or at least must be consistent with, the speed of the hydrologic cycle that is required to balance the globally averaged rate of atmospheric radiative cooling.

The net radiative cooling of the atmosphere is strongly affected by the high, cold cirrus clouds, many of which are formed within precipitating cloud systems. The cirrus clouds absorb the infrared radiation emitted by the warm atmosphere and surface below; the cirrus themselves emit much more weakly because they are very cold. This means that the cirrus effectively trap infrared radiation inside the atmosphere. For this reason, as the cirrus cloud amount increases, the radiative cooling of the atmosphere decreases.

Consider together the following points, which have been made in the last few paragraphs:

- The radiative cooling of the atmosphere is primarily balanced by latent heat release in precipitating cloud systems.
- Precipitating weather systems produce cirrus clouds.
- Cirrus clouds tend to reduce the radiative cooling of the atmosphere.

In combination, these ideas suggest a negative feedback loop that tends to regulate the strength of the hydrologic cycle. To see how this works, consider an equilibrium in which atmospheric radiative cooling and latent heat release are in balance. Suppose that we perturb the equilibrium by increasing the speed of the hydrologic cycle, including the rate of latent heat release. The same perturbation will (presumably) increase the rate of cirrus cloud production, which will reduce the rate at which the atmosphere is radiatively cooled. The radiative cooling acts to promote cloud formation through moist convection, so when the radiative cooling rate decreases, cloud activity slows down. In this way, the initial perturbation is damped. Further discussion is given in Chapter 6.

The "effective altitude" for infrared emission by the Earth-atmosphere system is near 5 km above sea-level. This simply means that the outgoing longwave radiation at the top of the atmosphere is equivalent to that from a black body whose temperature is that of the atmosphere near the 5 km level. Roughly speaking, then, atmospheric motions must carry energy upward from the surface through the first 5 km of the atmosphere, and infrared emission carries the energy the rest of the way out to space. This upward energy transport by moving air occurs on both small scales, notably in boundary-layer turbulence and cu-

mulus convection, and also on large scales, notably through midlatitude baroclinic eddies and the tropical Hadley circulation., which are discussed in later chapters. In short, the atmospheric circulation carries energy upward as well as poleward.

We now examine in more detail the fluxes of various quantities at the Earth's surface. In addition to the surface solar and terrestrial radiation, we must also consider the turbulent fluxes of momentum, sensible heat, and latent heat. In principle, we should also consider the fluxes of various chemical species, but this important aspect of the climate system is neglected here.

An example of the seasonal variations of the surface shortwave and longwave radiation at a particular station is given in Fig. 2.12, which shows the variations of the upward and downward shortwave (SW) and longwave (LW) near-surface radiation at a field site in Oklahoma. The data cover the three years 2006 - 2008. The seasonal cycle is clearly evident. High frequency fluctuations are primarily due to cloudiness. Note that the upward solar radiation has ocasional maxima during the winter. These are associated with the increased albedo of the ground following snow storms.

Data like those shown in Fig. 2.12 are available for only a few stations around the world. Most of our ideas about the global pattern of surface radiation are based on various estimates, which have been carefully worked out but are subject to significant errors (e.g., Wielicki et al., 1996). Panel A) of Fig. 2.13 shows the meridional distribution of the zonally averaged solar radiation absorbed by the Earth's surface, as a function of latitude, and for January, July, and the annual mean. Seasonal changes are clearly visible and easy to interpret. Near 50° N in July there is a slight dip or "shoulder" in the meridional profile of the surface absorbed solar radiation. This is associated with cloudiness, and indicates that the clouds are having a major impact on the energy budget of the ocean in those latitudes. Cloudiness also leads to a weak tropical minimum, just north of the Equator. The annual mean curve is fairly symmetrical about the Equator, but shows a minimum near 10° N associated with tropical rain systems. Note also that in the annual mean the southern high latitudes absorb less than the northern high latitudes.

The zonally averaged net surface longwave energy flux is shown in panel B) of Fig. 2.13. In January, the strongest cooling occurs over Antarctica, and in the subtropics of the winter hemisphere. The weakest cooling occurs in cloudy regions, e.g. over the Southern Oceans and in the storm tracks of both hemispheres. Although the surface temperature is warmer in summer than in winter, at some latitudes the net longwave cooling of the surface is actually stronger in winter than in summer! The explanation is that the downward radiation from the atmosphere to the surface increases from winter to summer due to both the warming of the air and the increase in the atmospheric emissivity due to seasonally increased water vapor content and also seasonal changes in cloudiness. This increase in the downward component is so strong that it sometimes overwhelms the increase in the upward component, giving a net decrease in surface infrared cooling from winter to summer. Panel C) shows the zonally averaged net surface radiation (solar and terrestrial combined). High

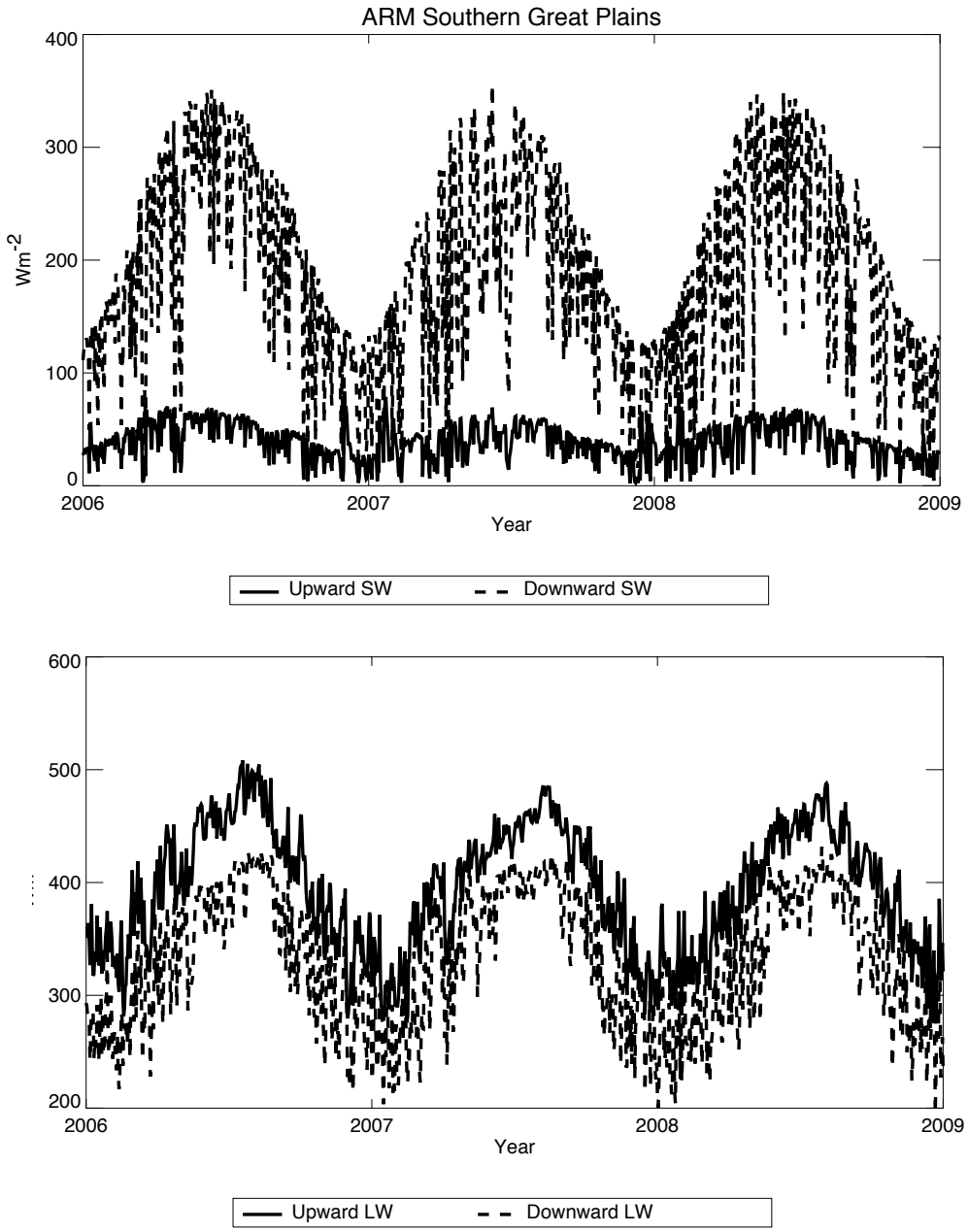

Figure 2.12: Observations of the upward and downward solar (SW) and terrestrial (LW) radiation at the Southern Great Plains observing facility of the Atmospheric Radiation Measurement Program, in Oklahoma, USA. The data are for the years 2006 - 2008.

latitudes experience net radiative cooling of the surface in winter, as would be expected. The annual mean net radiation into the surface is positive at all latitudes. It follows that the surface must cool by non-radiative means.

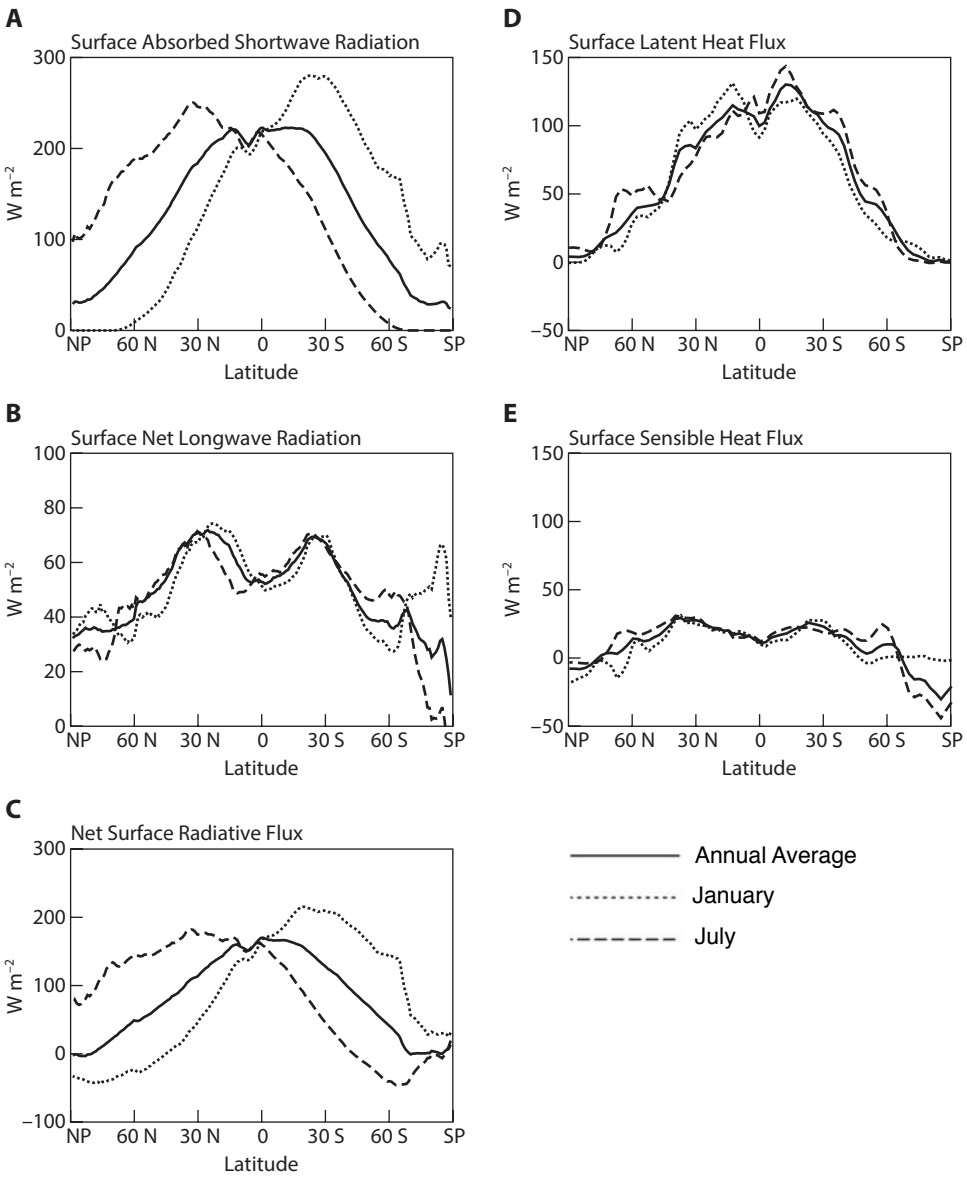

Figure 2.13: A summary of the zonally averaged energy budget of the Earth's surface. A) The zonally averaged (land and ocean) net solar radiation absorbed by the Earth's surface. B) The zonally averaged (land and ocean) net infrared cooling of the Earth's surface. C) The zonally averaged net surface radiation, obtained by combining the data from panels A) and B). D) The zonally averaged surface latent heat flux, positive upward. E) The zonally averaged surface sensible heat flux, positive upward. Panels A) - C) are based on Wielicki et al. (1996). Panels E) - F) are based on the ECMWF reanalysis. Note: These data are not true observations, although they are based on observations.

Panel D) shows the zonally averaged net latent heat flux. Positive values represent a moistening of the atmosphere and a cooling of the surface. The latent heat flux compen-

sates, to a large extent, for the net radiative heating of the surface shown in the previous figure. Note that the maxima of the latent heat flux occur in the subtropics. Recall that the precipitation maxima occur in the tropics and middle latitudes. This implies that moisture is transported from the subtropics into the tropics, and from the subtropics into middle latitudes. Panel E) shows the corresponding curves for the surface sensible heat flux. Note that the surface sensible heat flux is generally smaller than the surface latent heat flux. Maxima occur in the winter hemisphere, especially in the Northern winter in association with cold-air outbreaks over warm ocean currents at the east coasts of North America and Asia. Local heat flux maxima associated with such cold outbreaks can be on the order of 1000 W m^{-2}, on individual days.

We close this chapter with a figure that illustrates the globally and annually averaged vertical flows of energy by various processes. We use CERES data for the net vertical flux of energy due to radiation, as a function of height. The net radiation curve is constrained by measurements of the radiation at the top of the atmosphere, but the vertical profile is computed using a radiative transfer model with the observed state of the atmosphere as input. The net radiation is zero at the top of the atmosphere, and downward at all other levels. This downward radiative energy flux must be balanced by upward fluxes due to other processes. The energy flux due to large-scale circulations was computed from the ECMWF Interim reanalysis, and is snown by the red curve. It reaches a maximum in the lower middle troposphere, around 700 hPa, and decreases above. This means that the large-scale ciruclation removes energy from the lower troposphere and deposits it in the upper troposphere. The energy flux due to convection and turbulence, plotted as a green curve, was computed as a residual, using the assumption that the total globally and annually averaged flux of energy must be zero at all heights. It is largest at the surface, and decreaes upward at all levels. All three curves hug zero at and above the 100 hPa level.

The surface value of the net radiation shown in the figure differs from the value shown in Table 2.2, and surface flux due to convection and turbulence in the figure also differs from the sum of the sensible and latent heat fluxes shown in Table 2.2. These differences reflect various uncertainties in the calculations.

A key conclusion from the figure is that *the globally and annually averaged upward flux of energy due to convection and turbulence exceeds that due to large-scale motions throughout the lower and middle troposphere*. The two fluxes are approximately equal in the upper troposphere. Remember, however, that the convective activity is determined in part by the large-scale circulation, and vice versa. These two contributions to the upward energy flux are jointly produced by what amounts to a single, strongly coupled system of processes, operating on a wide range of spatial and temporal scales. That is a major theme of this book.

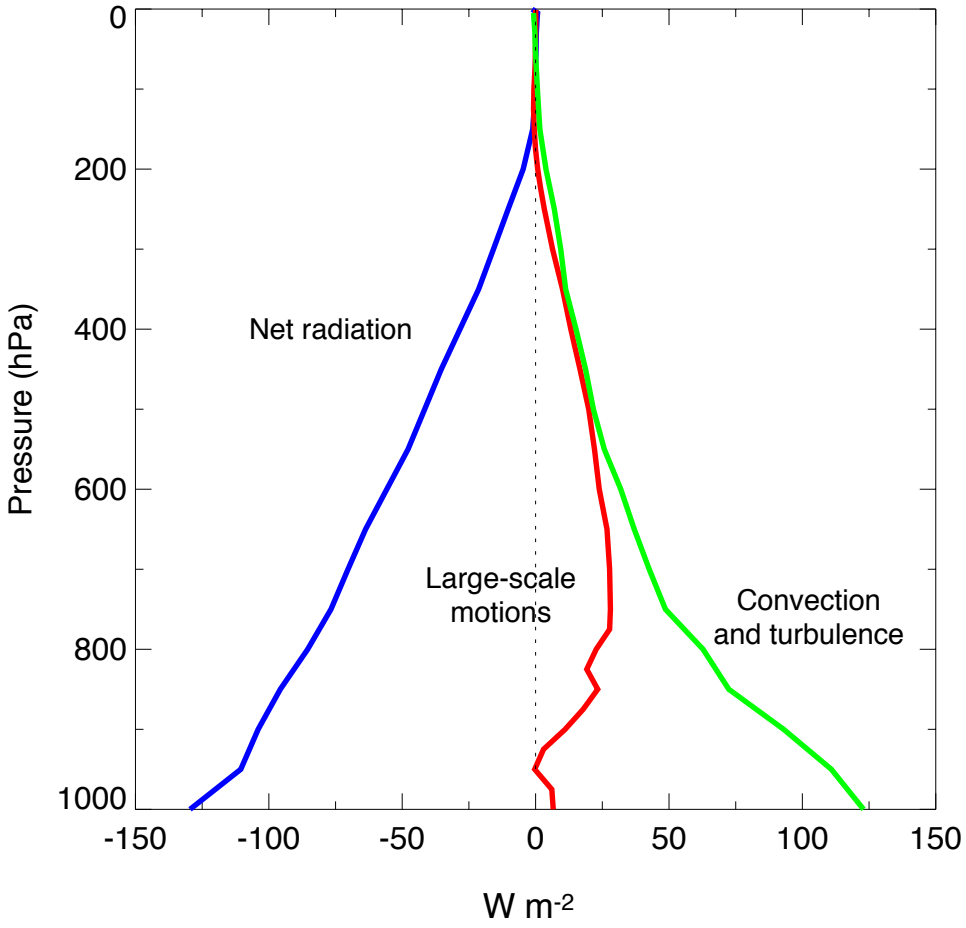

Figure 2.14: Estimates of the globally and annually averaged vertical flows of energy due to radiation, large-scale motions, and convection and turbulence. The radiation fluxes are based on CERES data. The fluxes due to large-scale motions are computed from the ECMWF reanalysis. The fluxes due to convection and turbulence are computed as a residual.

2.5 Segue

This chapter provides a brief overview of the energy fluxes at the top of the atmosphere, at the Earth's surface, and across the atmosphere. The meridional structure of the net radiation at the top of the atmosphere implies transports by the ocean-atmosphere system. The meridional structure of the net surface energy flux implies energy transports by the ocean. The meridional structure of the net flow of energy into the atmosphere, across its upper and lower boundaries, implies a net transport of energy by the atmosphere. In later chapters we will discuss the nature of these energy transports in more detail, and as well as the meridional transports of angular momentum and moisture.

Among the most important points in this chapter is that the net radiative heating of the

Earth's surface is balanced mainly by evaporative cooling, and the net radiative cooling of the atmosphere is balanced mainly by latent heat release. We also mentioned the important effects of water vapor and clouds on the Earth's radiation budget. Finally, we discussed the lower boundary conditions on the global atmospheric circulation associated with the distributions of continents and oceans, sea surface temperature, topography, vegetation, and ice and snow.

With this preparation, we are now ready to take a look at some of the observed features of the global circulation.

2.6 Problems

1. (a) Prove that, for any vector $\mathbf{Q}$,

$$\int_S \nabla \cdot \mathbf{Q}\, dS = 0, \tag{2.14}$$

where the integral is taken over a closed surface, e.g., the surface of a sphere. We assume that $\mathbf{Q}$ is everywhere tangent to the surface, i.e., it "lies in" the surface and so can be described as a "horizontal" vector. Eq. (2.14) shows that the globally averaged divergence of any horizontal vector is zero.

(b) Also prove that

$$\int_S \mathbf{k} \cdot (\nabla \times \mathbf{Q})\, dS = 0, \tag{2.15}$$

where the integral is taken over a closed surface. Here $\mathbf{k}$ is a unit vector everywhere perpendicular to the surface. Eq. (2.15) implies that the global mean of the vertical component of the vorticity is zero.

2. (a) Suppose that 1 W m^{-2} is supplied to a column of water 100 m deep. Assume that the temperature changes uniformly with depth throughout the entire column. How much time is needed to increase the temperature of the water by 1 K?

(b) Estimate the heat capacity of the entire global ocean in J K^{-1}. If all of the solar radiation incident at the top of the atmosphere were used to warm the ocean uniformly, how long would it take for the temperature of the entire ocean to increase by 1 K?

Chapter 3

A quick overview of the circulation

3.1 Introduction

This chapter is intended to provide a brief summary of some of the important phenomena of the observed seasonally varying global circulation of the atmosphere, with a few additional comments about non-seasonal variability. Selected fields will be shown and described, with an emphasis on mass, the winds, temperature, and moisture. Among the most important phenomena introduced are the tropical Hadley and Walker circulations, the monsoons, planetary waves, and some aspects of the hydrologic cycle. All of these things will be discussed in more detail in later chapters. Lots of questions will be raised, but for the most part the answers will be deferred until later.

Many of the plots shown in this and later chapters are based on analyses (actually, reanalyses) created at the European Centre for Medium Range Weather Forecasts (ECMWF; Uppala et al., 2005). The existence of such analyses, and their ready availability online, makes a book like this one enormously easier to create now than in decades past. The nature of a reanalysis is briefly explained in Chapter 6.

3.2 The global distribution of atmospheric mass

Mass is arguably the most fundamental quantity in any physical description of the atmosphere. The density, ρ, is defined as the mass of air per unit volume. With high accuracy, the surface pressure is equal to the weight of the air above, per unit area, which is given by

$$p_S = \int_{z_S}^{\infty} \rho g dz. \tag{3.1}$$

.

Here p is pressure, the subscript S denotes a surface value, g is the acceleration of gravity,

and z is height. The surface pressure varies from place to place, in part due to the effects of topography and in part due to the circulation of the atmosphere. An example is shown in Fig. 3.1. The figure shows surface pressure scatter-plotted against surface elevation, for 00Z (i.e., midnight in Greenwich, England) on January 1 and July 1, 2000. The main point of the figure is that a large fraction of the spatial variability of surface pressure is due to topography; you already knew this, but perhaps you have never seen the data plotted this way before. For each hemisphere, the data fall roughly onto two curves. The Northern Hemisphere points on the upper curve come mainly from Greenland, mainly for January, and the Southern Hemisphere points on the upper curve come mainly from Antarctica. The scatter of the data about their mean for each surface elevation indicates the dynamical variability of the surface pressure. The range of variability is particularly large when the surface height is zero, which means that it is large for the oceans. An interpretation is that weather systems are particularly vigorous over the oceans.

Maps of surface pressure are dominated by minima associated with mountain ranges. Because of this, maps of surface pressure maps do not clearly show how the horizontal pressure-gradient force varies with changes in the weather. To get around this problem, it is conventional to define "sea-level pressure," which is computed by adding to the surface pressure a correction that is designed to represent the additional pressure that would occur if the mountains were not present. Fig. 3.2 shows monthly mean maps of sea-level pressure for January and July. These maps are much smoother than weather maps plotted for particular observation times, because the moving highs and lows that represent individual weather systems have been smoothed out by the time-averaging. The plots on the right side of Fig. 3.2 show the corresponding zonally averaged distributions of the sea-level pressure for January and July.

Throughout this book, we will distinguish between the zonally averaged circulation, one aspect of which is the zonally averaged sea-level pressure shown in the right-side panels of Fig. 3.2, and departures from the zonal average, which we will call *"eddies"*. The highs and lows of the sea-level pressure that can be seen in Fig. 3.2 are associated with eddies.

Especially in the Northern Hemisphere, there is a very pronounced tendency for low pressure over the oceans and high pressure over the continents in winter, and vice versa in summer. This seasonal shift of mass between the oceans and continents is associated with a seasonal shift in surface temperature. Fig. 3.3 shows the departure of the surface temperature from its zonal mean at each latitude, for January and July. We can say that these are plots of the "eddy surface temperature." The figures show that in middle latitudes, especially in the Northern Hemisphere, the surface air temperature is generally colder over the continents than over the oceans in winter, and vice versa in summer. Particularly cold temperatures occur on the eastern sides of the Northern Hemisphere continents in January. This is partly because the flow is generally from west to east, so that the air on the east sides of the continents has traveled all the way across the cold continent in order to reach the eastern side, gradually cooling along the way. The strong temperature contrast on the east coasts of the Northern Hemisphere continents in winter leads to the frequent formation

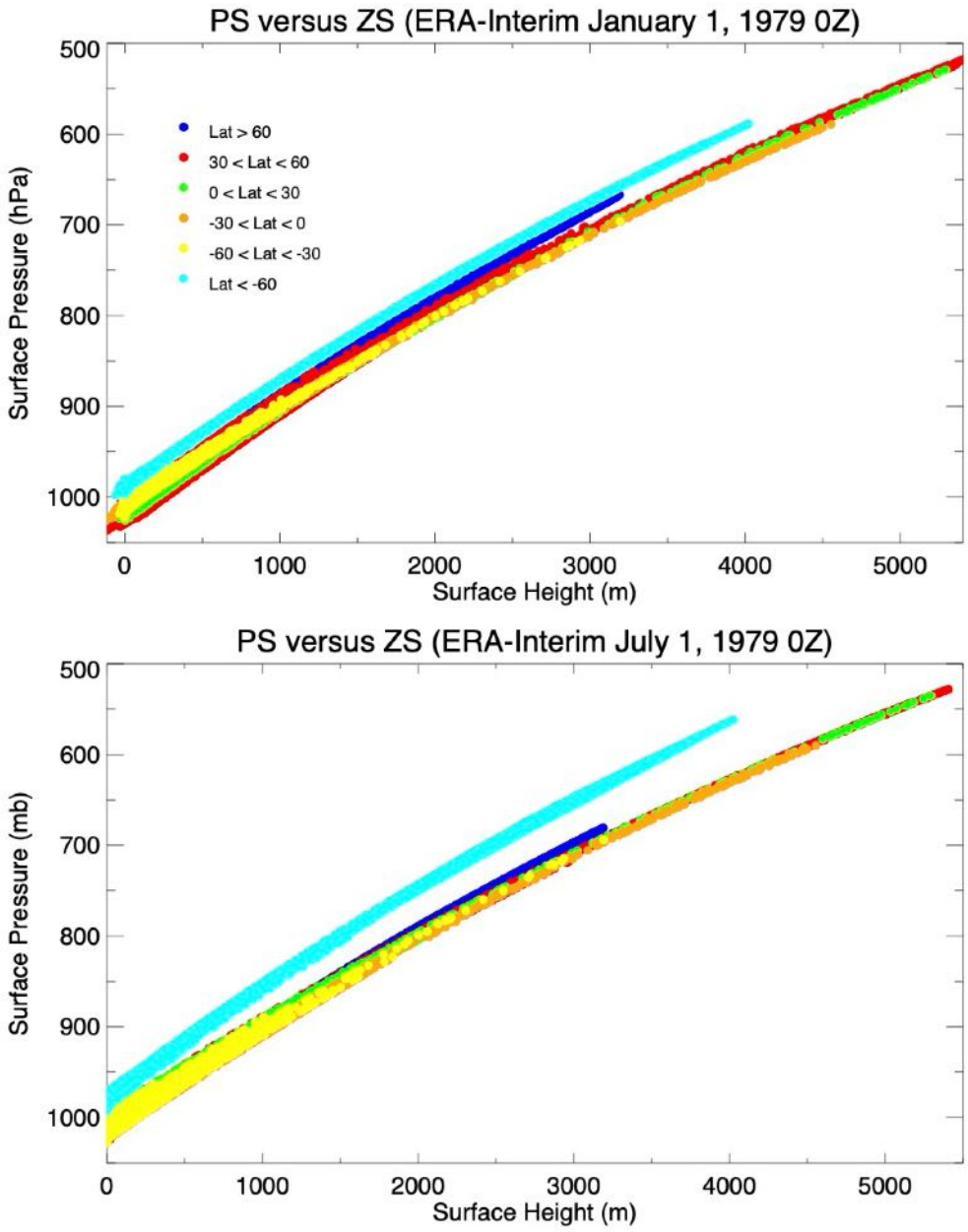

Figure 3.1: Surface pressure plotted against surface height, for particular observation times. Note that the vertical scale decreases upward. Color is used to indicate roughly which latitudes the data points come from. The dots along the dark blue curve come from Greenland, and the dots along the light blue curve come from Antarctica. The data were taken from a latitude-longitude grid, so the individual points do not represent equal areas.

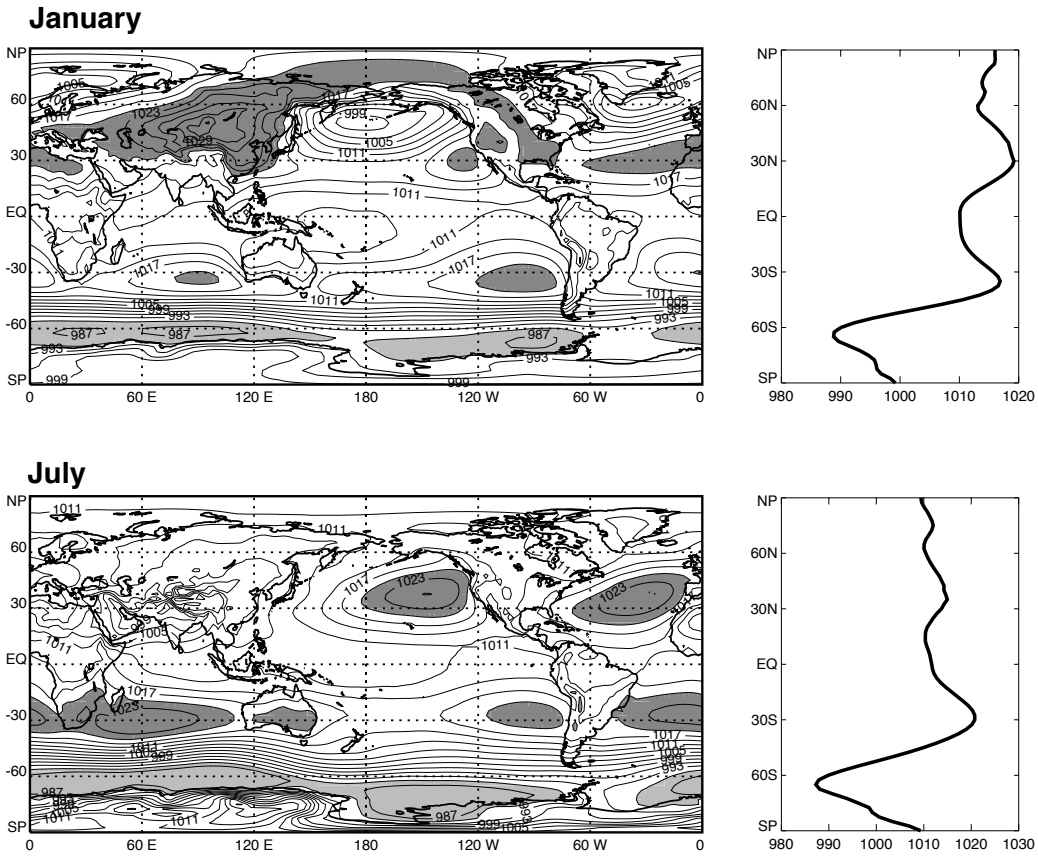

Figure 3.2: Sea-level pressure maps. The contour interval is 3 hPa. Values higher than 1020 hPa have dark shading, and those lower than 990 hPa have light shading. Averages with respect to longitude are shown on the right.

of winter storms, which are often called "baroclinic eddies." Further discussion is given later.

Comparison of Figs. 3.2 and 3.3 shows that there is a tendency for high sea-level pressures to be associated with cold surface temperatures, and vice versa. To understand this, recall that cold air has a higher density than warm air (for a given pressure), so that a "pile" of cold air of a given geometrical thickness will contain more mass, and therefore weigh more, than a pile of warm air of the same geometrical thickness. This can be seen mathematically by combining the ideal gas law with (3.1) to obtain

$$p_S = \int_{z_S}^{\infty} \left(\frac{pg}{RT} \right) dz. \tag{3.2}$$

.

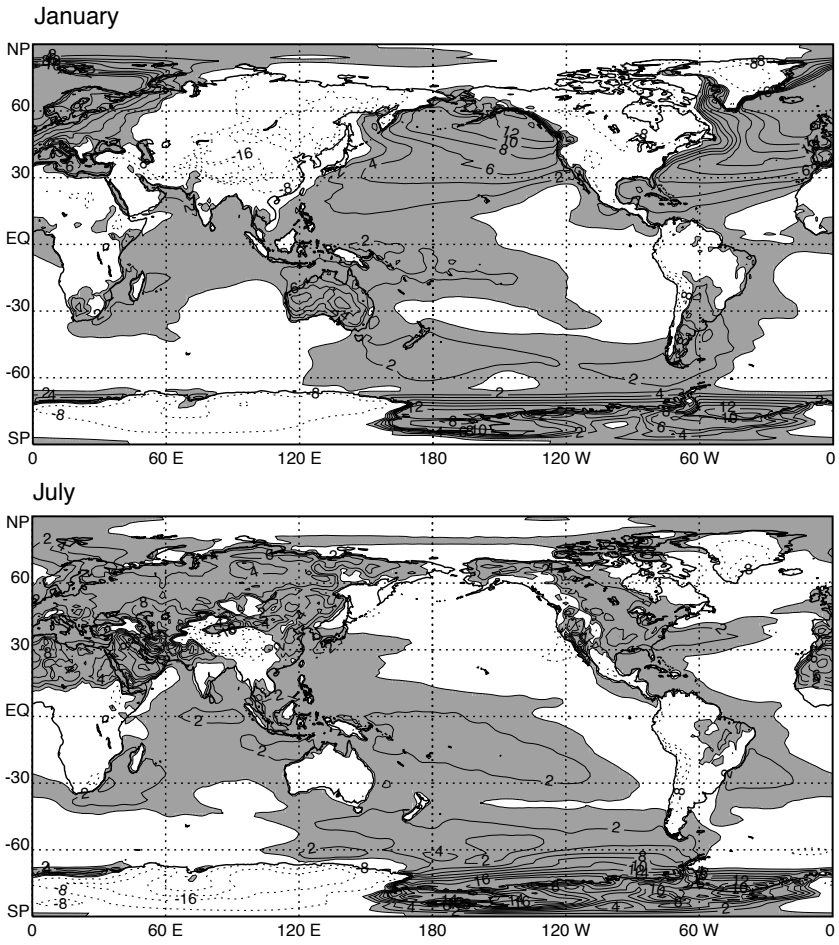

Figure 3.3: The departure of the 2 m temperature from its zonal mean at each latitude, for January and July. Positive values are shaded. The contour interval is 2 K.

Here R is the gas constant for dry air, and T is temperature.

Fig. 3.2 shows that for both January and July there is a tendency for high sea-level pressure to occur in the subtropics, near $\pm 30^\circ$. These subtropical highs typically appear as "cells," e.g., in the North Atlantic and North Pacific in July, or off the west coast of South America in January. In many cases, the subtropical highs are found over the eastern parts

of the oceans. In the Northern Hemisphere, they are particularly strong in the northern summer (Hoskins, 1996). Strong highs are also apparent in middle latitudes during winter, e.g., in Siberia and western North America. Both regions are quite mountainous.

In spherical coordinates, and using pressure as the vertical coordinate, geostrophic balance is expressed by

$$0 = f v_g - \frac{1}{a \cos\varphi} \left(\frac{\partial \phi}{\partial \lambda} \right)_p , \tag{3.3}$$

and

$$0 = -f u_g - \frac{1}{a} \left(\frac{\partial \phi}{\partial \varphi} \right)_p , \tag{3.4}$$

where u_g and v_g are the zonal and meridional components of the geostrophic wind, respectively; f is the Coriolis parameter, and ϕ is the geopotential. With appropriate caution, we can use (3.3) and (3.4) to relate the pressure gradients to the winds. For example, throughout the year, there is a zonally oriented belt of low pressure across the tropics. Geostrophy tells us that the decrease of sea-level pressure from the subtropics towards the Equator implies tropical easterlies near the surface, although we have to be careful about invoking geostrophy near the Equator, where the Coriolis parameter passes through zero. Because the sea-level pressure generally decreases from the subtropics to middle latitudes, the geostrophic relation leads us to expect surface westerlies on the poleward side of the subtropical highs. The relatively high pressure over the poles suggests surface easterlies near the south pole, although the "sea-level" pressures plotted for Antarctica must be taken with a grain of salt because the surface of Antarctica is far above sea level.

In the Northern Hemisphere during northern winter, prominent low-pressure cells appear, most notably near the Aleutian Islands and Iceland. These are regions where storm systems are often found on individual days. There is a tendency for a minimum of the sea-level pressure near 60°N, especially in January but also to some extent in July. A very pronounced belt of low pressure is found over the "southern ocean" north of Antarctica, throughout the year, although it is more intense in July (winter) than January (summer).

Generally there is less seasonal change in the Southern Hemisphere than in the Northern Hemisphere. Also, the departures from the zonal means are much stronger in the Northern Hemisphere than the Southern Hemisphere.

The tropical sea level pressure distribution is generally very smooth and featureless, compared to that of middle latitudes. A simple explanation for this was given by Jule Charney (1963), in terms of the differences in dynamical balance between the tropics. Charney

Figure 3.4: Jule G. Charney, whose many achievements include scale analyses of both extratropical and tropical motions, development of the quasi-geostrophic theory, development (in his Ph.D. thesis at the University of California at Los Angeles) of a classical theory of baroclinic instability, pioneering work on numerical weather prediction, analysis of the interactions of cumulus convection with large-scale motions in tropical cyclones, development of a theory of planetary waves propagating through shear, analysis of blocking, and a theory of desertification. Figure used with permission of the MIT Museum.

(Fig. 3.4) was one of the giants of twentieth-century meteorology. His work is discussed for the first time in this chapter, but his name will come up again and again throughout the remainder of this book. Charney's explanation of the flatness of tropical sea-level pressures is based on the fact that in middle latitudes the effects of the Earth's rotation are much more important than particle accelerations, while the opposite is true in the tropics. He began his scale analysis (see Appendix B) with the equation of horizontal motion, which can be written in simplified form as

$$\frac{D\mathbf{v}}{Dt} + f\mathbf{k}\times\mathbf{v} = -\nabla_p\phi. \tag{3.5}$$

Here $\mathbf{v}$ is the horizontal wind vector, and $\mathbf{k}$ is a unit vector pointing upward. The three terms shown in (3.5) represent most of the "action" throughout most of the atmosphere. For middle latitudes, their orders of magnitude can be estimated as follows:

$$\left|\frac{D\mathbf{v}}{Dt}\right| \sim \frac{V^2}{L}, \tag{3.6}$$

$$|f\mathbf{k}\times\mathbf{v}| \sim f_{midlat}V, \tag{3.7}$$

$$\left|\nabla_p\phi\right| \sim \frac{|\delta\phi|}{L}. \tag{3.8}$$

Here V is a "velocity scale," which might be on the order of 10 m s^{-1}, L is a length scale, which might be on the order of 10^6 m, and $|\delta\phi|$ is the magnitude of a typical fluctuation of the geopotential height. Note that $|\delta V| \sim V$, but $|\delta\phi|$ is generally much less than ϕ. The numerical values of these scales have been chosen to be representative of "large-scale" motions on the Earth; if we wanted to analyze small-scale motions, we would choose different numerical values. The same numerical values of V and L can be used for both the tropics and middle latitudes because the term "large-scale" is used in the same way for both regions.

In middle latitudes, the acceleration following a particle, $D\mathbf{v}/Dt$, is usually negligible in (3.5), compared to the rotation term. A typical value of $D\mathbf{v}/Dt$ can be estimated as $V^2/L \sim 10^2/10^6 = 10^{-4}$ m s^{-2}. A representative midlatitude value of the Coriolis parameter is 10^{-4} s^{-1}, so that $f_{midlat}V \sim 10^{-3}$ m s^{-2}, about one order of magnitude larger than $D\mathbf{v}/Dt$. Geostrophic balance is, therefore, approximately satisfied in mid-latitudes, i.e.,

$$f_{midlat}V \sim \frac{(\delta\phi)_{midlat}}{L}, \tag{3.9}$$

or

$$(\delta\phi)_{midlat} \sim f_{midlat} V L. \tag{3.10}$$

According to (3.10), rotation can balance pressure gradients in midlatitudes.

The Coriolis parameter vanishes on the Equator, so it is reasonable to expect that sufficiently close to the Equator geostrophic balance breaks down (a point discussed further in Chapter 9), and particle accelerations tend to balance the pressure gradient force, much as they do on small scales almost everywhere in the atmosphere, and in many engineering contexts (e.g., the flow of water in a pipe):

$$\frac{V^2}{L} \sim \frac{(\delta\phi)_{tropics}}{L}, \tag{3.11}$$

or

$$(\delta\phi)_{tropics} \sim V^2. \tag{3.12}$$

Comparing (3.11) and (3.12), we see that

$$\frac{(\delta\phi)_{tropics}}{(\delta\phi)_{midlat}} \sim \frac{V}{f_{midlat} L} \equiv \mathrm{Ro}_{midlat}, \tag{3.13}$$

where Ro_{midlat} is a midlatitude Rossby number. By substituting the numerical values given above, we find that $\mathrm{Ro}_{midlat} \cong 0.1$. Eq. (3.13) therefore tells us that geopotential height fluctuations on pressure surfaces are much smaller in the tropics than in middle latitudes. It follows that pressure fluctuations on height surfaces are an order of magnitude smaller in the tropics than in middle latitudes. The real message is that the horizontal pressure-gradient force is much smaller in the tropics than in middle latitudes. This conclusion holds at any level, so it holds at all levels.

At this point, we can bring in the hydrostatic equation to show that large-scale fluctuations of temperature and surface pressure are also much smaller in the tropics than in middle latitudes. Suppose that the pressure-gradient force is small at some particular height. If the temperature changes rapidly in the horizontal, this will imply large horizontal pressure gradients at other heights. The implication is that if the horizontal pressure gradient is small *at*

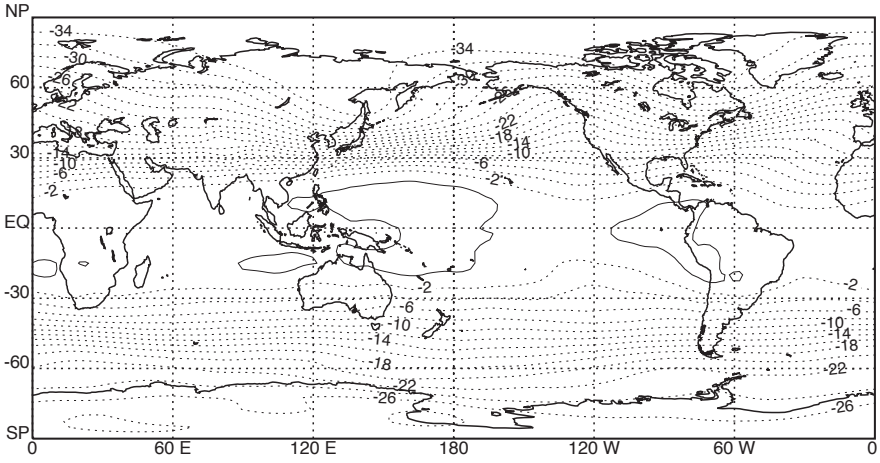

Figure 3.5: The departure of the 500 hPa temperature from its value at Darwin, Australia, for January. The contour interval is 2 K, and the zero contour is solid while negative contours are dashed. Note the amazing uniformity of the tropical temperatures. This is a consequence of the smallness of the Coriolis parameter in the tropics, as explained by Charney (1963).

all levels, then the horizontal temperature gradients must also be small. Fig. 3.5 illustrates this.

The smallness of horizontal temperature gradients in the tropics is now widely invoked to justify what is called the "weak temperature gradient approximation" (e.g., Sobel et al., 2001). It is important to remember, however, that, as explained above, Charney's primary conclusion is that horizontal *pressure* gradients are weak in the tropics; the weakness of the tropical horizontal temperature gradients is a secondary conclusion (Romps, 2012).

3.3 Zonal wind

Fig. 3.6 shows the latitude-height distribution of the zonally averaged zonal wind for January and July, respectively. The plot extends from the surface to the middle stratosphere. We plot the wind components and other variables against height, rather than pressure, because the pressure coordinate tends to "squash" the stratosphere into a thin region at the top of the plot, obscuring its structure. Although the stratosphere contains only a small fraction of the mass of the whole atmosphere, it is home to some spectacular phenomena, and its dynamical influence extends downward into the troposphere. The stratosphere should be of interest even to people who are mainly interested on the global circulation of the troposphere.

In both January and July, easterlies extend through the entire depth of the tropical troposphere. They are somewhat stronger in July. They are concentrated in the Northern Hemisphere in July and the Southern Hemisphere in January. The near-surface easterlies are stronger in the winter hemisphere.

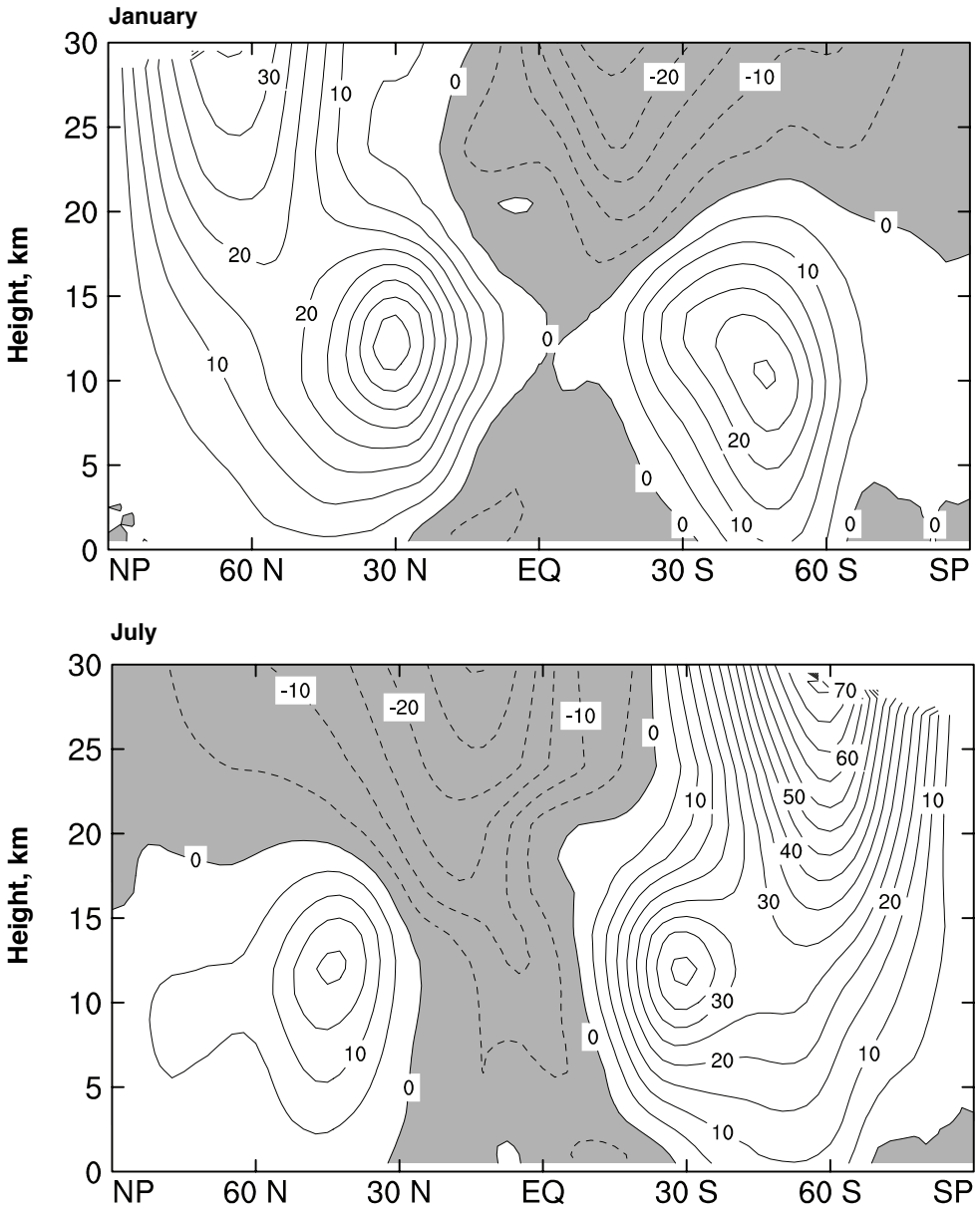

Figure 3.6: Latitude-height section of the zonal wind. The contour interval is 5 m s^{-1}. Easterlies are shaded.

Westerly jet streams are quite prominent in the upper troposphere, especially in the winter hemisphere. These are called the subtropical jets, and they reach their maximum strength during winter at about 30° latitude. Directly below the winter subtropical jet, the surface zonal wind is very weak. The jet extends poleward, however, with a hint of a second maximum in the troposphere near 50 or 60° from the Equator, where the zonally averaged

surface wind is definitely westerly. The subtropical jets are weaker in summer, and are shifted to about 45° latitude. The subtropical jet maxima are consistently found near the 200 hPa level, which is the cruising altitude of commercial airliners.

Suppose that the zonal surface wind is nearly geostrophic. Then, in the absence of mountains (e.g., over the oceans) the surface pressure must have a meridional maximum at a latitude where u_S passes through zero, i.e., where surface easterlies meet surface westerlies. Comparison of Fig. 3.2 with Fig. 3.6 shows that in fact the subtropical surface-pressure maxima occur at about the same the latitudes where the zonal component of the surface wind passes through zero. The subtropical highs sit under the subtropical jets.

Strong westerly jets also occur in the winter stratosphere. In the Southern Hemisphere in July, there is a clear minimum in the westerlies near 150 hPa, at about 40°S. Above and poleward of this minimum is a very powerful stratospheric westerly jet, called the polar night jet. As shown below, these strong stratospheric westerlies are associated with very cold stratospheric temperatures over the poles. A similar but weaker polar night jet occurs in the Northern Hemisphere winter. The stratospheric jets are separated from the troposphere jets by a (weak) minimum of the westerlies.

Easterlies fill the summer-hemisphere stratosphere. As discussed later, the summer stratosphere is radiatively controlled, while the winter stratosphere is strongly influenced by dynamics, including upward wave propagation from the troposphere.

XX add discussion of radiatie heating figure

The zonally averaged surface winds are quite weak near the poles.

Fig. 3.8 shows maps of the 850 hPa zonal wind for January and July, respectively. Again, keep in mind that many intense small-scale (∼1000 km) features would appear in daily maps, but have been smoothed out here by time averaging. The monthly mean maps show very obvious alternating bands of easterlies and westerlies, which are qualitatively reminiscent of Jupiter (see Fig. 3.9), although Jupiter has more bands; generally speaking, the Earth's atmosphere features easterlies in the tropics, westerlies in middle latitudes, and easterlies again near the poles. We can also see features associated with the strong cells in the sea level pressure maps, e.g., the easterlies in the extreme North Pacific in January, associated with the Aleutian Low. Again, variations with longitude are much more apparent in the Northern Hemisphere than the Southern Hemisphere. Generally speaking, however, the features seen in the maps have a very zonal orientation, with strong north-south gradients and relatively weak east-west gradients. Note the intensification of both the zonal-mean flow and the eddies of the midlatitude westerlies in winter, in each hemisphere. In winter, the Northern Hemisphere westerlies are particularly strong over the oceans.

The strong positive maximum in the Arabian Sea in July is associated with the Indian monsoon; this is discussed in Chapter 9. The westerlies north of Australia (but south of the Equator) in January are indicative of the Winter Monsoon. In both regions, the sign of the zonal wind reverses seasonally.

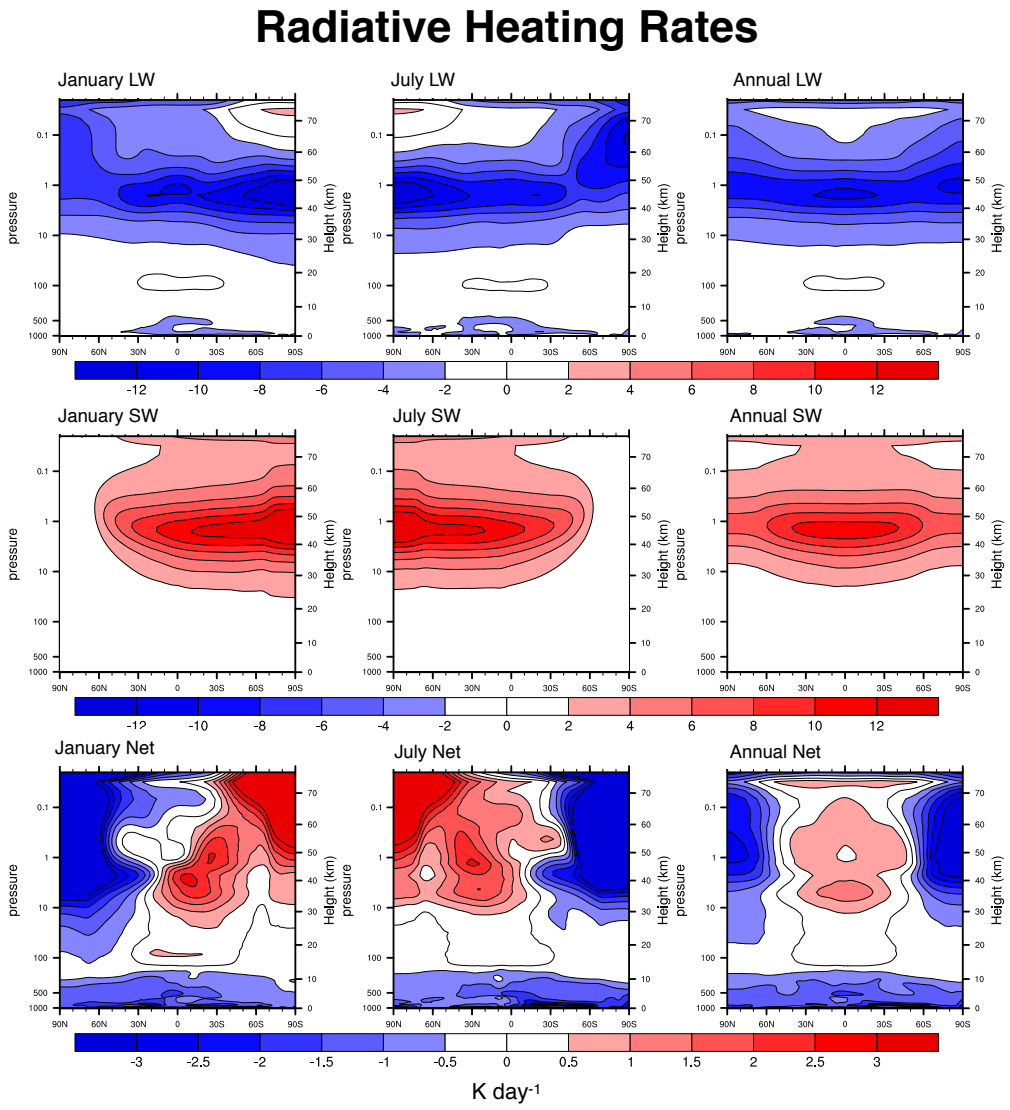

Figure 3.7: Latitude-height sections of longwave (LW), shortwave (SW) and net radiative heating rates for January, July, and the annual mean. The color bar for the net heating differs from the other two color bars. These data are from the ERA5 reanalysis, so they are not true measurements but they have been influenced by measurements.

Fig. 3.10 shows the corresponding maps for 200 hPa. The winds are generally stronger aloft than near the surface; this is true of both the zonal-mean flow and the eddies. Note the very prominent January westerly jet maxima off the east coasts of North America and, especially, Asia. There is also a westerly jet maximum at about 30° S, near the Date Line. In the Northern winter, there are "dipoles" consisting of easterly-westerly pairs, straddling the equator, near the Americas and also near the longitude of Australia. At some longitudes, the westerlies extend to the Equator in January. In July, there are equatorial easterlies at all longitudes, and the westerlies have intensified in the midlatitudes of the

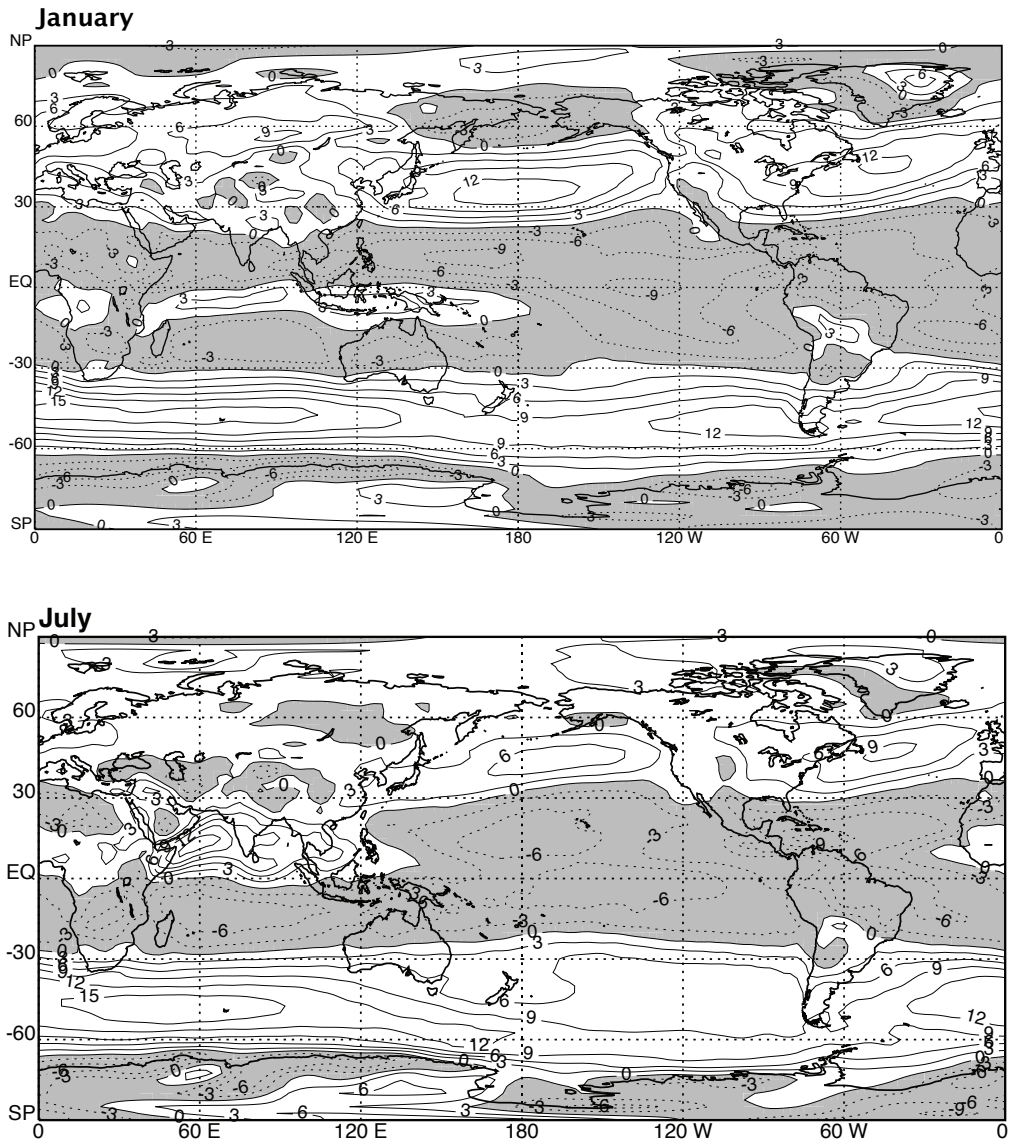

Figure 3.8: Maps of the 850 hPa zonal wind, for January and July. The contour interval used is 3 m s^{-1}. Easterlies are shaded.

Southern Hemisphere, and weakened in the midlatitudes of the Northern Hemisphere. Two intrusions of westerlies are seen in the Northern Hemisphere tropics: one just east of the Date Line, and another over the Atlantic Ocean. As discussed later, these regions of mean westerlies allow waves to propagate from middle latitudes into the tropics.

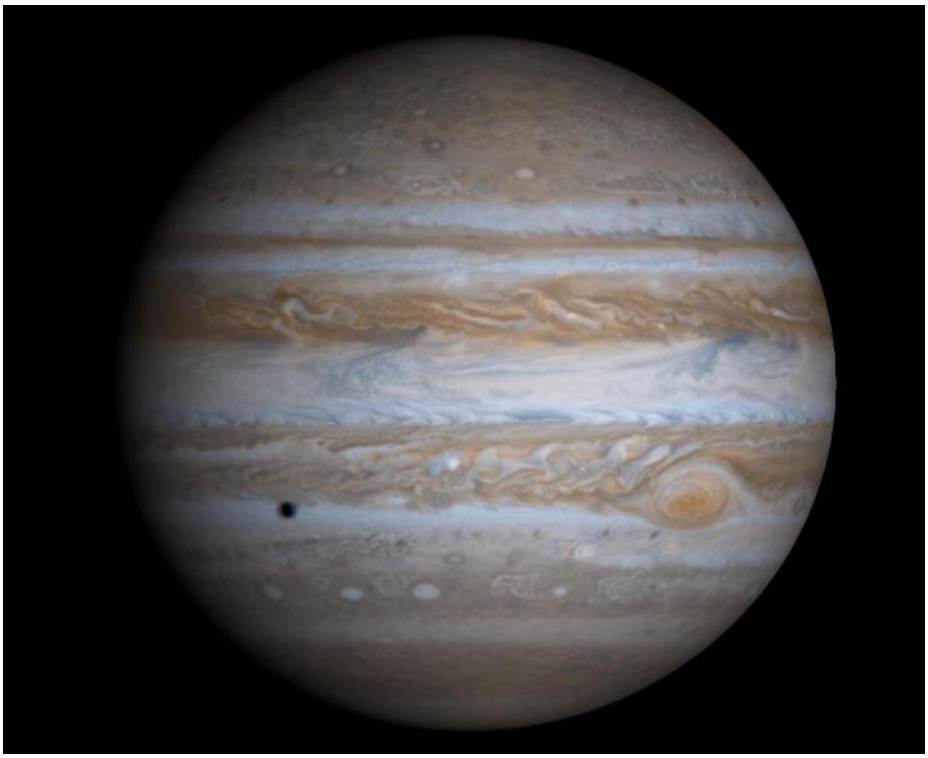

Figure 3.9: An image of Jupiter obtained from the Cassini probe on December 7, 2000. Note the zonal bands, and the Great Red Spot in the southern hemisphere. The black dot is the shadow of Jupiter's moon Europa. From https://www.jpl.nasa.gov/spaceimages/details.php?id=PIA02873.

3.4 Meridional wind

Fig. 3.11 shows the latitude-height distribution of the zonally averaged meridional wind for January and July, respectively. The zonal means reach about 2 m s^{-1} in absolute value; the strongest values occur in the tropics. In the winter-hemisphere tropics, in both months, there is a conspicuous dipole structure, with poleward flow aloft and equatorward flow near the surface. Evidently there is convergence near the equator at low levels, and divergence aloft. The convergence zone near the surface shifts from the Southern Hemisphere in January to the Northern Hemisphere in July. These features are associated with the Hadley circulation, which is discussed later in this chapter and again in Chapter 6. Poleward flow is also found near the surface in middle latitudes, with weak equatorward flow above. We can also see weak regions of low-level convergence near 60°S and 60°N.

As with most other fields, the seasonal changes of the meridional wind in the mid-latitudes of the Southern Hemisphere are quite weak, relative to those in the Northern Hemisphere.

The mass-weighted vertical mean of the time- and zonally averaged meridional wind

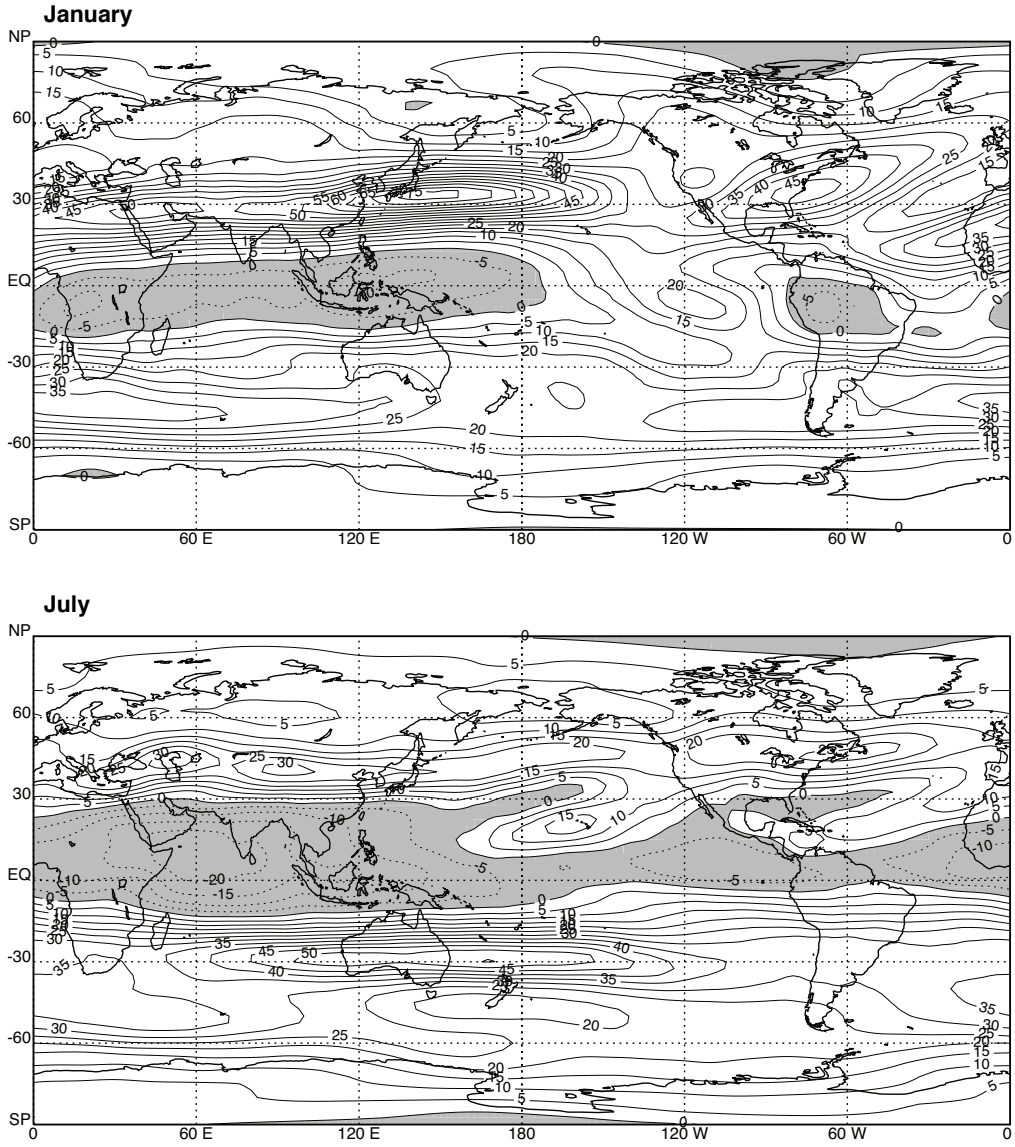

Figure 3.10: Maps of the 200 hPa zonal wind for January and July. The contour interval is 5 m s^{-1}. Easterlies are shaded.

must be very close to zero at all latitudes. This can be understood from the surface pressure-tendency equation,

$$\frac{\partial p_S}{\partial t} + \nabla \cdot \left(\int_0^{p_S} \mathbf{v} dp \right) = 0, \tag{3.14}$$

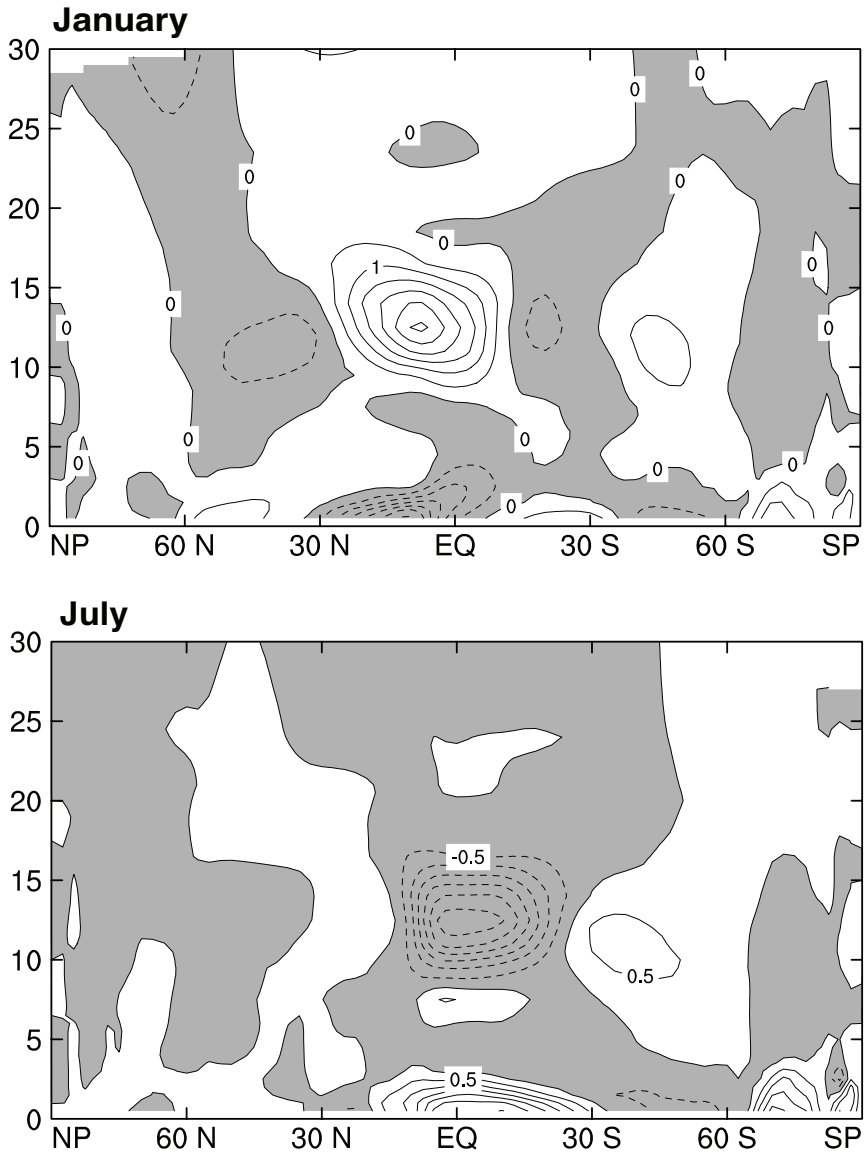

Figure 3.11: Latitude-height plots of the zonally averaged meridional wind, for January and July. The contour interval is 0.5 m s^{-1}.

which is derived in Chapter 4. In (3.14), $\mathbf{v}$ is the horizontal wind vector. The physical meaning of (3.14) is that the surface pressure changes in time due to the convergence or divergence of mass in the column above. Averaging (3.14) around a latitude circle gives

$$\frac{\partial \overline{p_S}^{\lambda}}{\partial t} = \frac{-1}{a\cos\varphi}\frac{\partial}{\partial\varphi}\left(\overline{\int_0^{p_S} v\,dp}^{\lambda}\cos\varphi\right). \tag{3.15}$$

In an average over a sufficiently long time, $\frac{\partial \overline{p_S}^{\lambda}}{\partial t}$ must become negligible at each latitude, because p_S is bounded within a fairly narrow range, so that (3.15) reduces to

$$\frac{\partial}{\partial \varphi}\left(\overline{\int_0^{p_S} v dp}^{\lambda,t} \cos\varphi\right) = 0. \tag{3.16}$$

Eq. (3.16) means that $\overline{\int_0^{p_S} v dp}^{\lambda,t} \cos\varphi$ is independent of latitude. Since $\cos\varphi = 0$ at both poles, we conclude that

$$\boxed{\overline{\int_0^{p_S} v\,dp}^{\lambda,t} = 0 \text{ at all latitudes.}} \tag{3.17}$$

The physical interpretation of (3.17) is very simple. Suppose, for example, that $\overline{\int_0^{p_S} v dp}^{\lambda,t}$ was positive at the Equator, so that air was systematically flowing out of the Southern Hemisphere and into the Northern Hemisphere. That can really happen at a given instant, but if it continued over time the surface pressure in the Southern Hemisphere would eventually decrease to zero and the surface pressure in the Northern Hemisphere would increase to roughly double its normally observed average value. The pressure-gradient force would of course resist such a scenario. The implications of (3.17) for angular momentum transport are discussed in Chapter 6.

It follows from (3.3) that the zonally averaged meridional component of the geostrophic wind is *exactly* zero:

$$\boxed{\overline{v_g}^{\lambda} = 0} \tag{3.18}$$

on each pressure surface. Eq. (3.18) implies that all zonally averaged meridional circulations are completely ageostrophic. An implication is that the important large-scale circulations are not necessarily close to geostrophic balance. We note, however, that the strongest features in Fig. 3.11 are found in the tropics, where geostrophy is expected to lose its grip.

Eq. (3.15) shows that the mass-weighted vertical integral of the meridional wind (i.e., the vertically integrated meridional mass flux) can lead to systematic changes with time in the meridional distribution of atmospheric mass. Fig. 3.12 shows the variation with season of the vertically and zonally averaged meridional velocity, as inferred from the seasonal changes of the distribution of mass. The top panel shows variations with latitude, and the bottom panel shows the seasonal cycle at the Equator. The values are tiny: on the order of 1 millimeter per second.

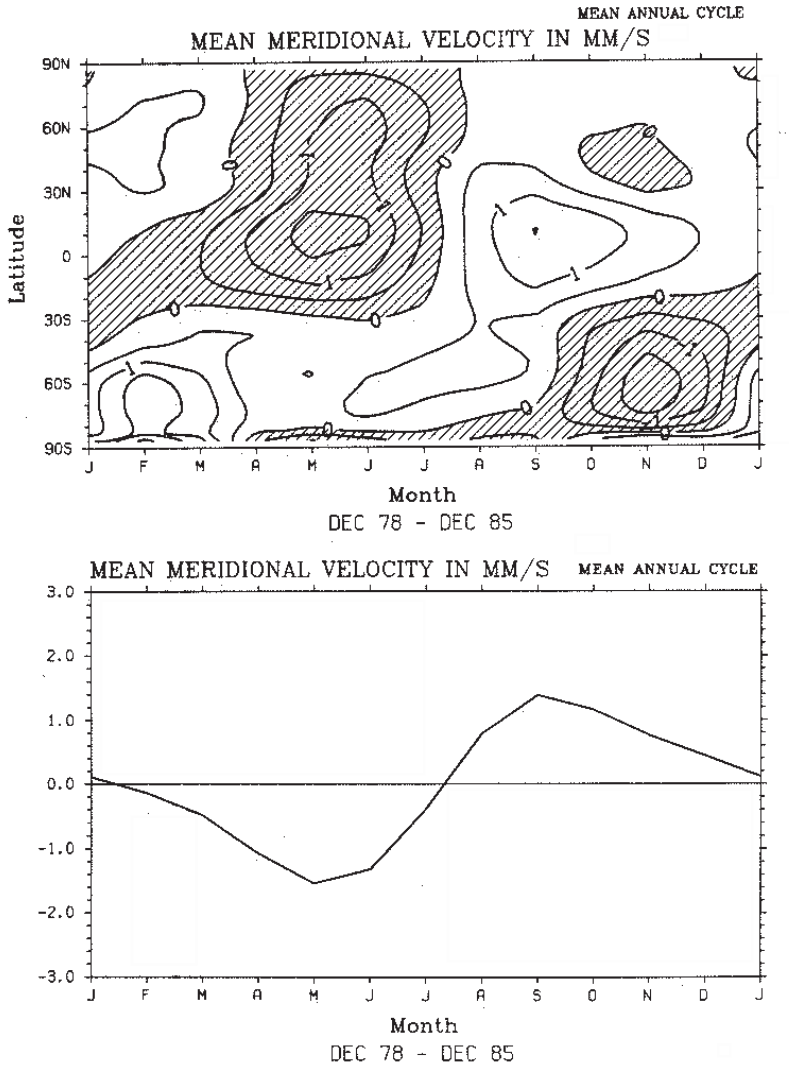

Figure 3.12: Seasonal variations of the mass-weighted vertically averaged meridional velocity, as inferred from the seasonally changing meridional distribution of surface pressure. The top panel shows variations with latitude, and the bottom panel shows the climatological seasonal cycle at the Equator. From Trenberth et al. (1987).

The globally averaged surface pressure is very nearly invariant with time, apart from small changes associated with the seasonal cycle of atmospheric water vapor. Trenberth

et al. (1987) discuss observations of the seasonal changes of the hemispherically averaged and globally averaged surface pressures associated with dry air and with water vapor. These are shown in Fig. 3.13. The fluctuations are on the order of 0.1% of the atmosphere's mass. Further discussion of the observed distribution of water vapor is given later in this chapter.

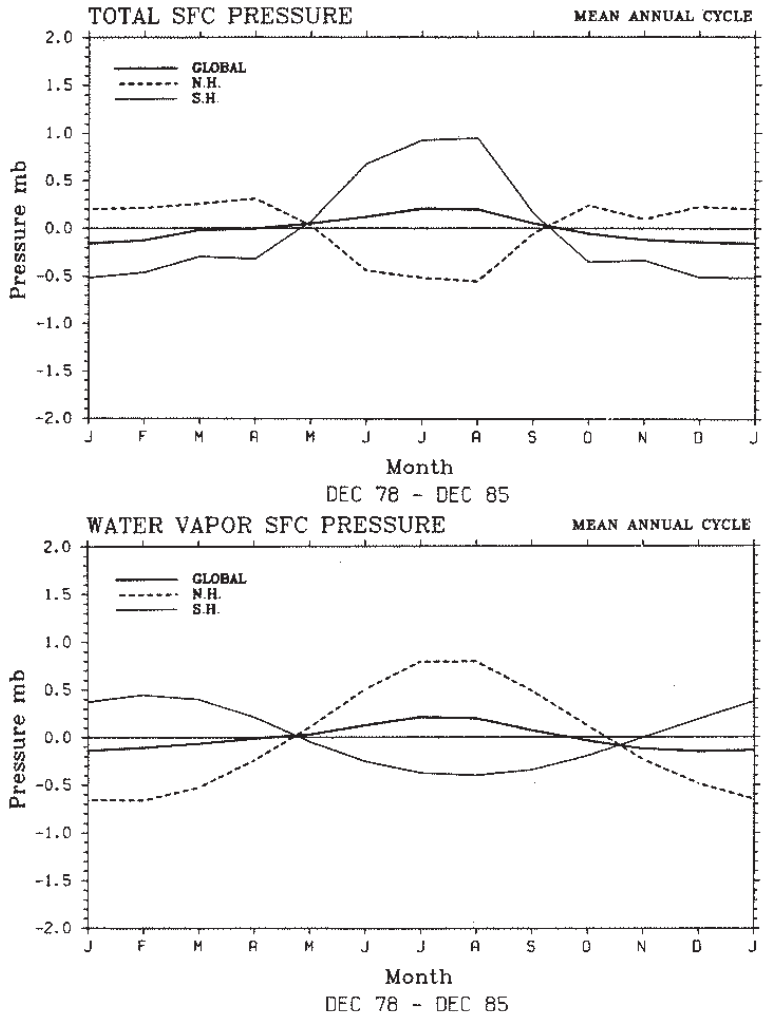

Figure 3.13: The variations with season of the hemispherically averaged and globally averaged surface pressures associated with dry air and with water vapor. From Trenberth et al. (1987).

Fig. 3.14 shows maps of the 850 hPa meridional wind for January and July, respectively. Fig. 3.15 shows the corresponding maps for the 200 hPa surface. Unlike the zonal wind, the time-averaged meridional wind does not show a banded, east-west structure; the east-west gradients are at least as strong as the north-south gradients. In the Northern Hemisphere, there is a tendency for alternating southerly and northerly flows, with a structure that resembles zonal wave number 3 or 4, i.e., 3 or 4 maxima and minima around a latitude

circle. The time-averaged meridional currents in the Southern Hemisphere are generally weaker than those in the Northern Hemisphere. The intensities of the meridional currents are stronger at 200 hPa than at 850 hPa. In the Northern Hemisphere especially, there is a tendency for stronger features in winter than in summer.

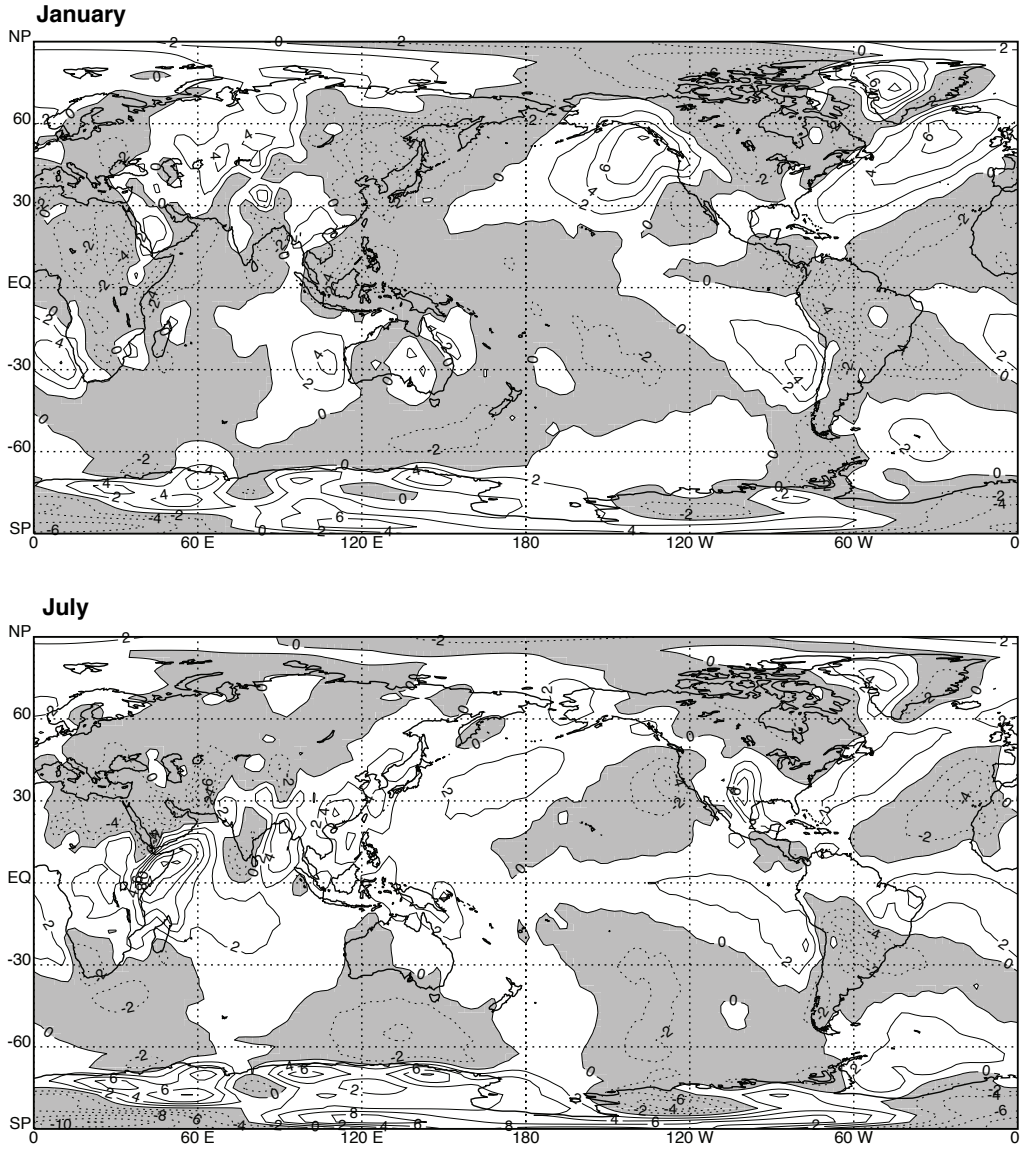

Figure 3.14: Maps of the 850 hPa meridional wind, for January and July. The contour interval is 2 m s^{-1}. Northerlies are shaded.

As can be seen in Fig. 3.11, the zonally averaged meridional flow in the tropics of the winter hemisphere is generally toward the summer pole at low levels, and toward the winter pole aloft. This is not very apparent in Fig. 3.14 or Fig. 3.15, however. Fig 3.14 shows

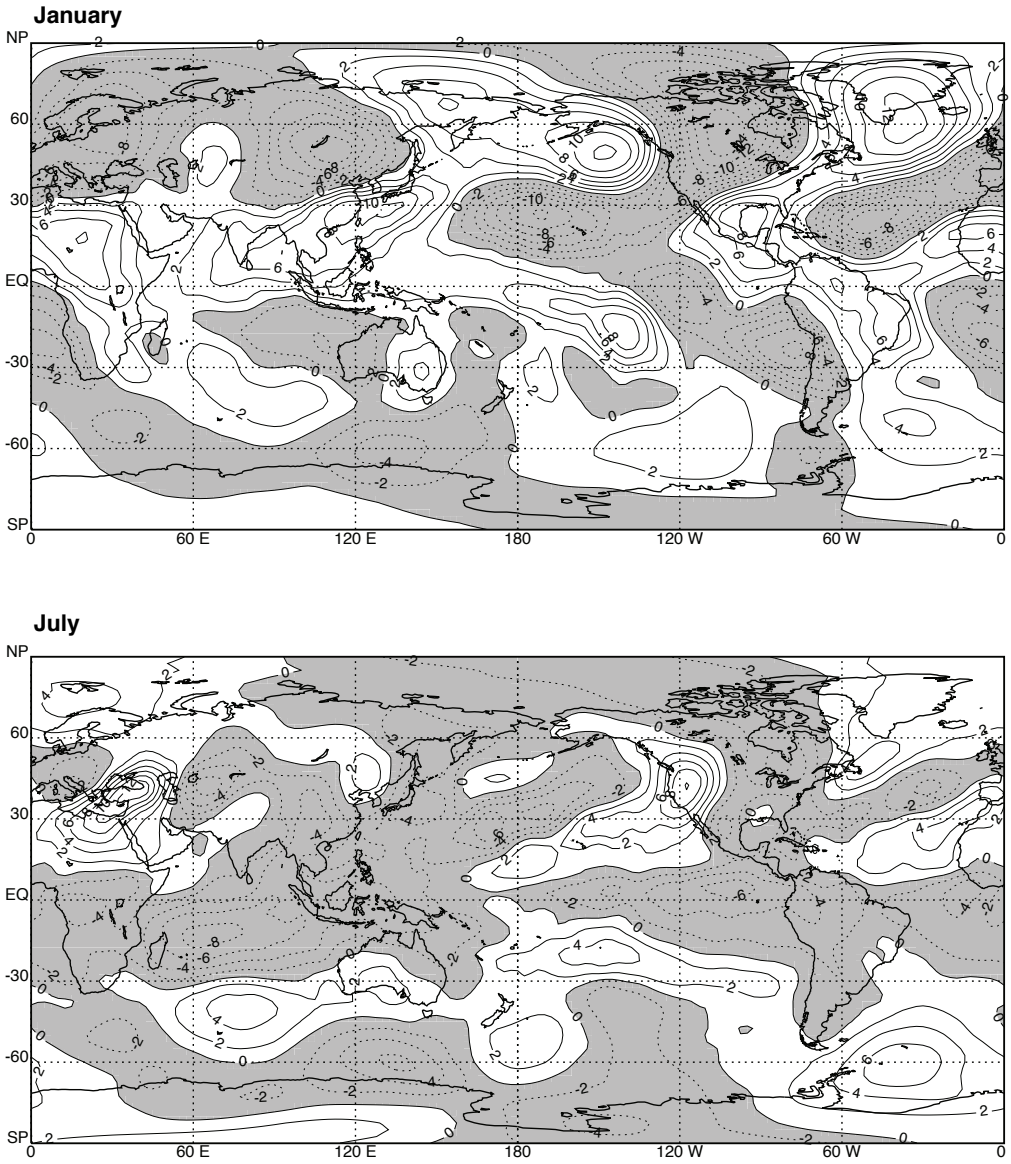

Figure 3.15: Maps of the 200 hPa meridional wind, for January and July. The contour interval is 2 m s^{-1}. Northerlies are shaded.

a strong southerly flow at 850 hPa just north of the Equator in July, associated with the Indian summer monsoon. The northerly flow near 120°E in January is associated with the winter monsoon, but is relatively inconspicuous.

In many parts of the world, the mean meridional wind reverses seasonally. Examples include the Arabian Sea, most of the North Pacific, and the southern Great Plains of North America.

Fig. 3.16 shows the streamlines at 850 hPa, for January and July, and Fig. 3.17 shows the corresponding streamlines at 200 hPa. Streamlines indicate direction but not magnitude. Such features as the subtropical highs and midlatitude lows of sea-level pressure are clearly evident in the 850 hPa winds. There are strong cross-equatorial flows at 850 hPa in both the Pacific and Indian Oceans, in July. The 200 hPa streamlines show the wavy patterns in the midlatitude winter, and also tropical phenomena including a strong monsoon-induced anticyclone over the Indian subcontinent in July.

3.5 Vertical velocity and the mean meridional circulation

The "mean meridional circulation" (MMC) is the name given to the circulation of mass in the the latitude-height plane. It can be analyzed by starting from the continuity equation in pressure coordinates, which is

$$\nabla_p \cdot \mathbf{v} + \frac{\partial \omega}{\partial p} = 0, \tag{3.19}$$

where ω is the vertical velocity as seen in pressure coordinates, i.e., the time rate of change of pressure following a particle of air. Taking the zonal average of (3.19), and using the form of the divergence operator in spherical coordinates as discussed in Chapter 2, we find that

$$\frac{1}{a\cos\varphi}\frac{\partial}{\partial\varphi}\left(\overline{v}^{\lambda}\cos\varphi\right) + \frac{\partial\overline{\omega}^{\lambda}}{\partial p} = 0. \tag{3.20}$$

It is useful to discuss the MMC in terms of a "stream function," ψ. Plots of ψ conveniently depict the zonally averaged vertical velocity and the zonally averaged meridional velocity, together in one diagram. The definition of ψ is embodied in the two equations

$$\overline{v}^{\lambda} 2\pi a\cos\varphi \equiv g\frac{\partial\psi}{\partial p}, \tag{3.21}$$

$$\overline{\omega}^{\lambda} 2\pi a^2\cos\varphi \equiv -g\frac{\partial\psi}{\partial\varphi}. \tag{3.22}$$

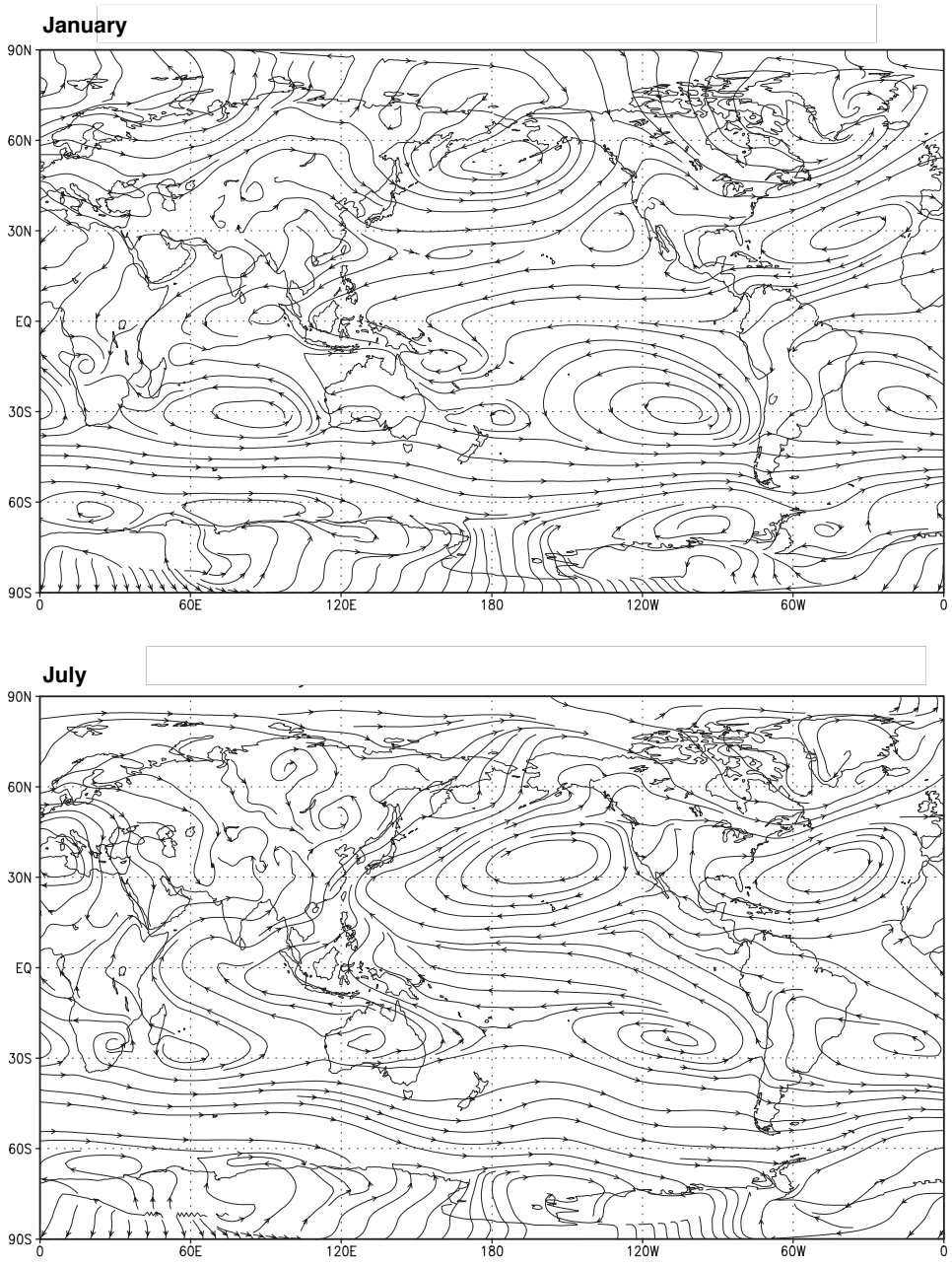

Figure 3.16: Streamlines of the 850 hPa wind, for January and July.

The motivation for this definition is that, for any given distribution of ψ, the zonally averaged continuity equation, (3.20), is automatically satisfied; this is easy to verify by substitution. Note that ψ is independent of longitude, because it is defined in terms of the zonal averages of v and ω. Because ψ is defined in terms of its derivatives, it can only be

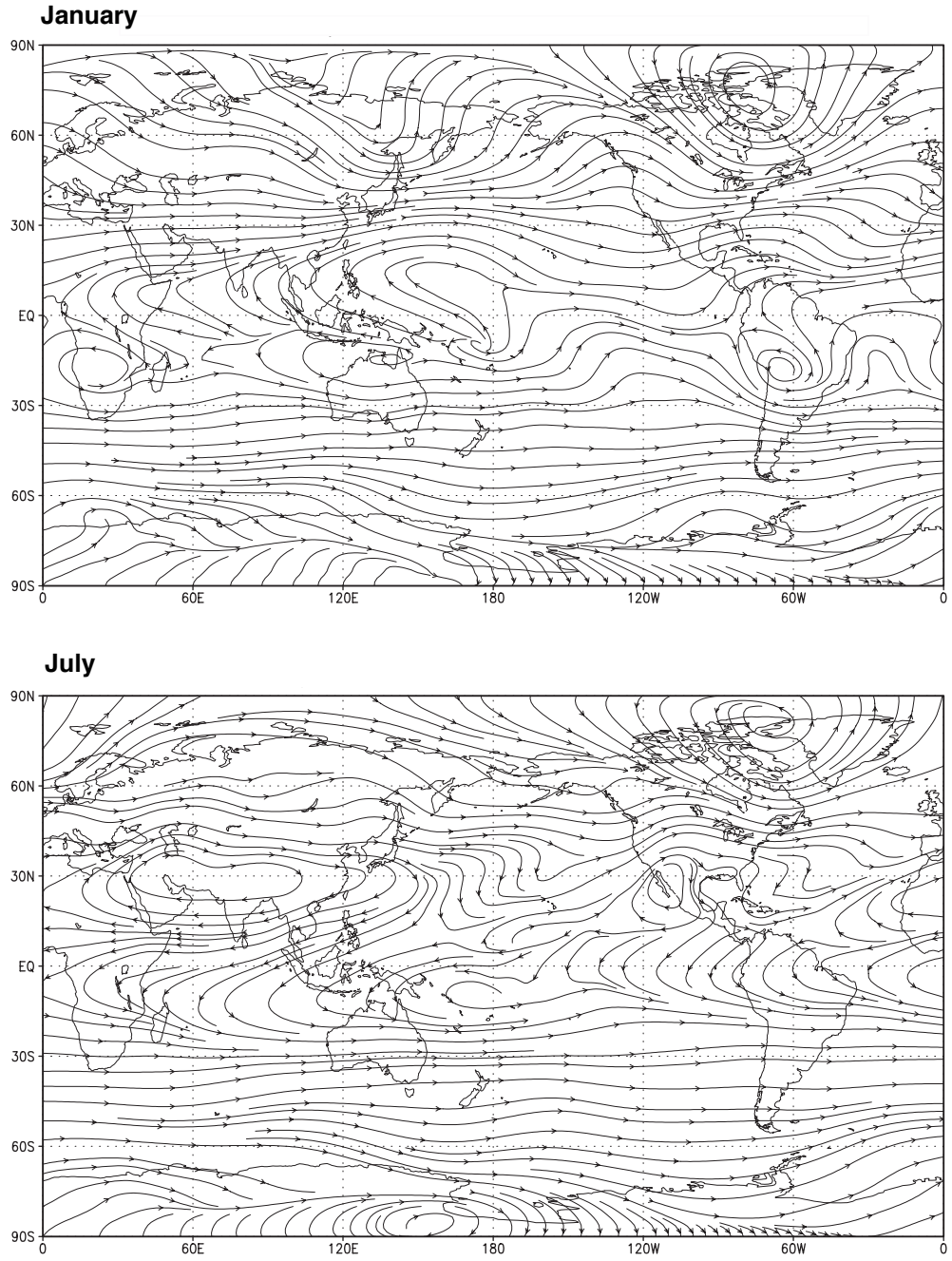

Figure 3.17: Streamlines of the 200 hPa wind, for January and July.

determined within an arbitrary constant. In other words, an arbitrary constant can be added to ψ without changing $\overline{v}^{\lambda}$ or $\overline{\omega}^{\lambda}$.

A minor technical difficulty is that the zonal averages used to define ψ cannot be carried

out for pressure surfaces that intersect the ground. We are going to ignore that issue. It can be skirted, for example by using a terrain-following vertical coordinate system, but the details are too technical to consider here.

In view of (3.21) and (3.22), we can compute ψ from either $\overline{v}^{\lambda}$ or $\overline{\omega}^{\lambda}$, but observations of $\overline{v}^{\lambda}$ are generally considered more reliable, so $\overline{v}^{\lambda}$ is the better choice. In order to do the vertical integration, we need a boundary condition. At $p = 0$, we have $\omega = 0$; this means that the atmosphere is neither gaining nor losing mass by exchanges with space. It follows that

$$\frac{\partial \psi}{\partial \varphi} = 0 \text{ at } p = 0, \tag{3.23}$$

i.e., the top of the atmosphere is a line of constant stream function. Similarly, lines of constant ψ cannot intersect the Earth's surface; if they did, that would imply a flow of air through the Earth's surface. We can therefore set

$$\frac{\partial \psi}{\partial \varphi} = 0 \text{ at } p = p_S, \tag{3.24}$$

In fact, since the zonal mean of the vertically integrated meridional wind is approximately zero in a time average, ψ must take *the same* latitude-independent value at $p = 0$ and $p = p_S$. It is conventional to choose this value to be zero, i.e., we use the upper boundary condition

$$\psi = 0 \text{ at } p = 0; \tag{3.25}$$

this choice determines the arbitrary constant mentioned above.

Note from (3.21) and (3.22) that

$$\psi \sim \left(\frac{\delta p}{g}\right) \cdot \frac{L}{t} \cdot L \sim \frac{M}{L^2} \cdot \frac{L^2}{T} = \frac{M}{T} \tag{3.26}$$

where M denotes dimensions of mass, L denotes dimensions of length, and T denotes dimensions of time. According to (3.26), ψ has dimensions of mass per unit time. It is

usually expressed in units of 10^{12} g s^{-1}, which is the same as 10^9 kg s^{-1}. This unit is sometimes called a "Sverdrup" (abbreviated Sv) in the oceanographic literature.

Fig. 3.18 shows the latitude-height distribution of the stream function of the MMC, for January and July, respectively. The observed meridional wind has been used to create these plots, by vertical integration of (3.21), and use of (3.25). The figure shows that deep rising motion occurs in the summer-hemisphere tropics, with sinking motion on either side. The strongest tropical rising motion is near 300 hPa, but notice that weak rising motion continues into the tropical stratosphere. The strongest subsidence is in the winter hemisphere subtropics, again near 300 hPa. Rising motion occurs in middle latitudes, and is strongest in the winter. Maximum values tend to occur near 500 hPa. Sinking motion is found near the poles, mainly in the lower troposphere. The cover of this book shows a portion of a Hadley cell over Africa in August, when the "large" Hadley cell has its rising branch north of the Equator, and its sinking branch in the southern subtropics. The rising branch of the is marked by the bright thunderstorms across Africa and extending out over the Atlantic Ocean, slightly north of the Equator. The sinking branch is associated with clear air over southern Africa, and shallow stratocumulus clouds over the South Atlantic.

The dominant cellular structures in the tropics are called "Hadley cells." They are very important branches of the global circulation. There is a "large" Hadley cell at each solstice, with its rising branch in the summer-hemisphere tropics and its body extending into the winter-hemisphere subtropics. Its peak magnitude is about 160 x 10^{12} g s^{-1}. A weaker Hadley cell is found in the summer hemisphere. Both Hadley cells are "direct" circulations, which means that their rising branches are warmer than their sinking branches. As discussed later, direct circulations convert potential energy into kinetic energy.

Because of the seasonal growth and decay of the Hadley cells in the two hemispheres, the zonally averaged meridional wind at the Equator reverses seasonally. Near the solstices it is from the winter hemisphere into the summer hemisphere at low levels, and from the summer hemisphere into the winter hemisphere in the upper troposphere. Bowman and Cohen (1997) discuss the inter-hemispheric transports associated with the seasonally changing Hadley circulations.

There are also indirect circulations in the middle latitudes, most clearly in the Southern Hemisphere in both seasons and both hemispheres. These are called "Ferrel cells." The sinking branches of the Ferrel cells are adjacent to the sinking branches of the Hadley cells; both are found in the subtropics, near 30° of latitude both north and south of the Equator. In these latitude belts, the sinking air diverges away horizontally, both toward the pole and toward the Equator. The poleward branch is the inflow to the rising motion of the Ferrel cell, and the Equatorward branch is the inflow to the rising branch of the Hadley cell. Recall that the zonally averaged sea-level pressure has its maximum in the subtropics; we can think of the diverging subtropical meridional flows as being pushed by the meridional pressure-gradient force, from the sea-level pressure maximum towards lower pressure on both sides. Further physical interpretation of the Ferrel cells is given later.

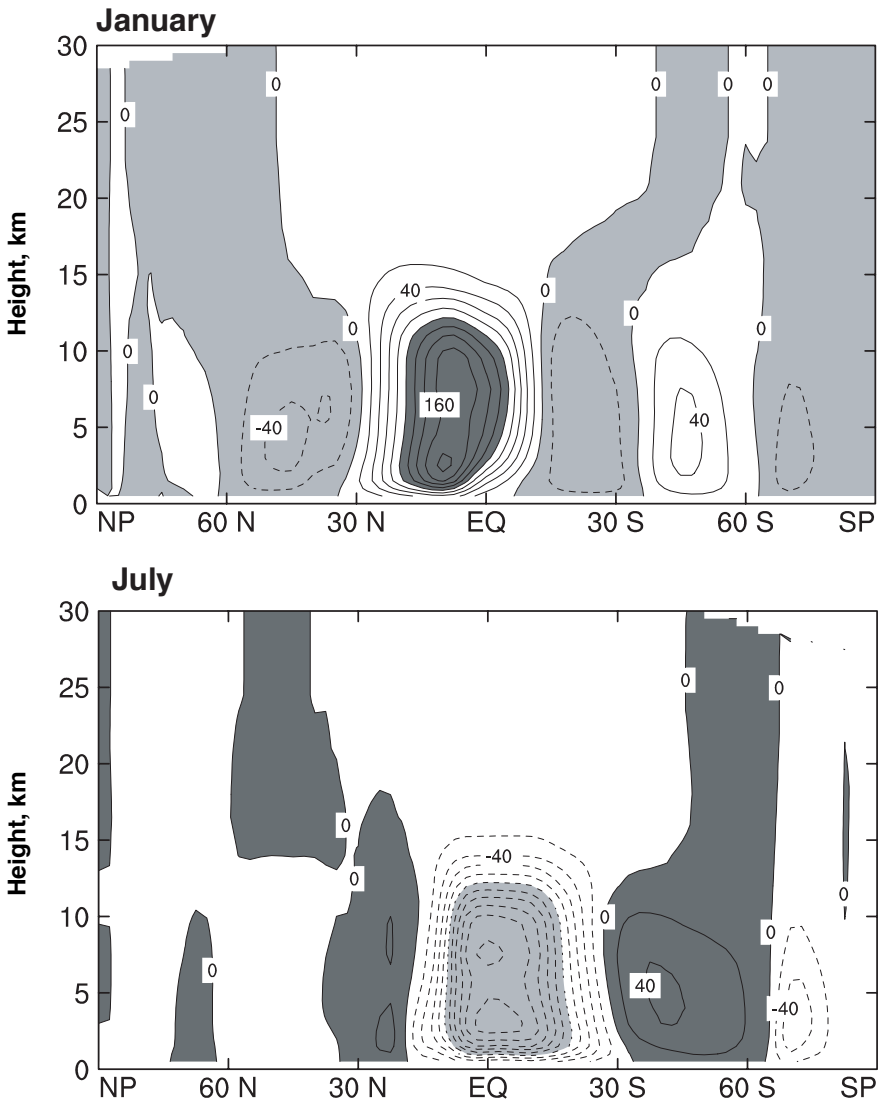

Figure 3.18: The stream function of the mean meridional circulation. Positive values represent counterclockwise circulations, while negative values represent clockwise circulations. The units are 10^{12} g s^{-1}.

Finally, the polar regions play host to weak direct circulations.

There is an important but very slow meridional circulation in the stratosphere, called the Brewer-Dobson circulation (Butchart, 2014). It is too weak to show up in Fig. 3.18, but it carries mass upward across the tropopause in the tropics, and then towards the winter pole. It produces important transports of ozone and angular momentum. It is discussed further in Chapter 11.

It is interesting to examine the seasonal change of the MMC, as shown in Fig. 3.19.

Rough symmetry between the hemispheres is seen approximately one month after the equinoxes. Near the solstices, the Hadley cells are best developed on the winter side, and least developed on the summer side. Explanations for this for this have been proposed by Lindzen and Hou (1988); Hack et al. (1989), and Dima and Wallace (2003). The rising motion on the summer side of the Equator, near the solstice, is associated with the summer monsoons (Newell et al., 1972; Schulman, 1973; Dima and Wallace, 2003), which are discussed in Chapter 9.

The correspondence between the zonally averaged vertical motion and the zonally averaged meridional motion is fairly evident. The meridional currents can be interpreted as outflows from or inflows to the vertical currents. Fig. 3.20 shows maps of the 500 hPa vertical velocity for January and July, respectively. The units are nanobars per second. The strongest maxima and minima have absolute values of roughly 1000 nanobars per second, which is about 100 hPa per day. Fig. 3.18 shows that there are regular bands of rising and sinking motion, arranged along latitude circles. The bands are apparent in Fig. 3.20, especially in the July data. There is some tendency for rising motion in the tropics; sinking motion in the subtropics, especially in the winter hemisphere; rising motion in middle latitudes; and sinking motion over the poles. Sinking motion tends to be associated with surface pressure maxima, and rising motion with surface pressure minima. For example, the subtropical highs are clearly identifiable as regions of large-scale sinking motion in the middle troposphere. The seasonal change of the large-scale vertical motion is very spectacular in the region of the Tibetan plateau. Rising motion occurs in summer, and sinking motion in winter. These changes are associated with the Indian monsoon, as discussed in Chapter 9. There are some cases of rising motion upstream of mountain ranges, and sinking motion downstream; examples are the Rocky Mountains and the Himalayas, in winter. Looking at the other major mountain ranges of the world, however, it is not easy to see a clear pattern of orographically forced vertical motions. They do exist, but a more refined analysis is needed to detect them.

Note the rising motion over southern Africa and tropical South America in January, in the same regions where we will see later that there are water vapor maxima at 850 hPa in January. There is a tendency for large water vapor mixing ratios in regions of rising motion, and small water vapor mixing ratios in regions of sinking motion. In particular, deserts, such as the Sahara, are regions of tropospheric sinking motion

3.6 Temperature

Fig. 3.21 shows the latitude-height distributions of the zonally averaged temperature for January and July, respectively. At low levels, the warmest air is near the Equator, but near 100 hPa the *coldest* air is over the Equator. In fact, some of the lowest temperatures in the atmosphere are found near the tropical tropopause. It is also true that the tropopause is highest in the tropics and lowest near the poles. The tropopause height is nearly discontinuous in the subtropics, particularly in the winter hemisphere. In the stratosphere, extremely

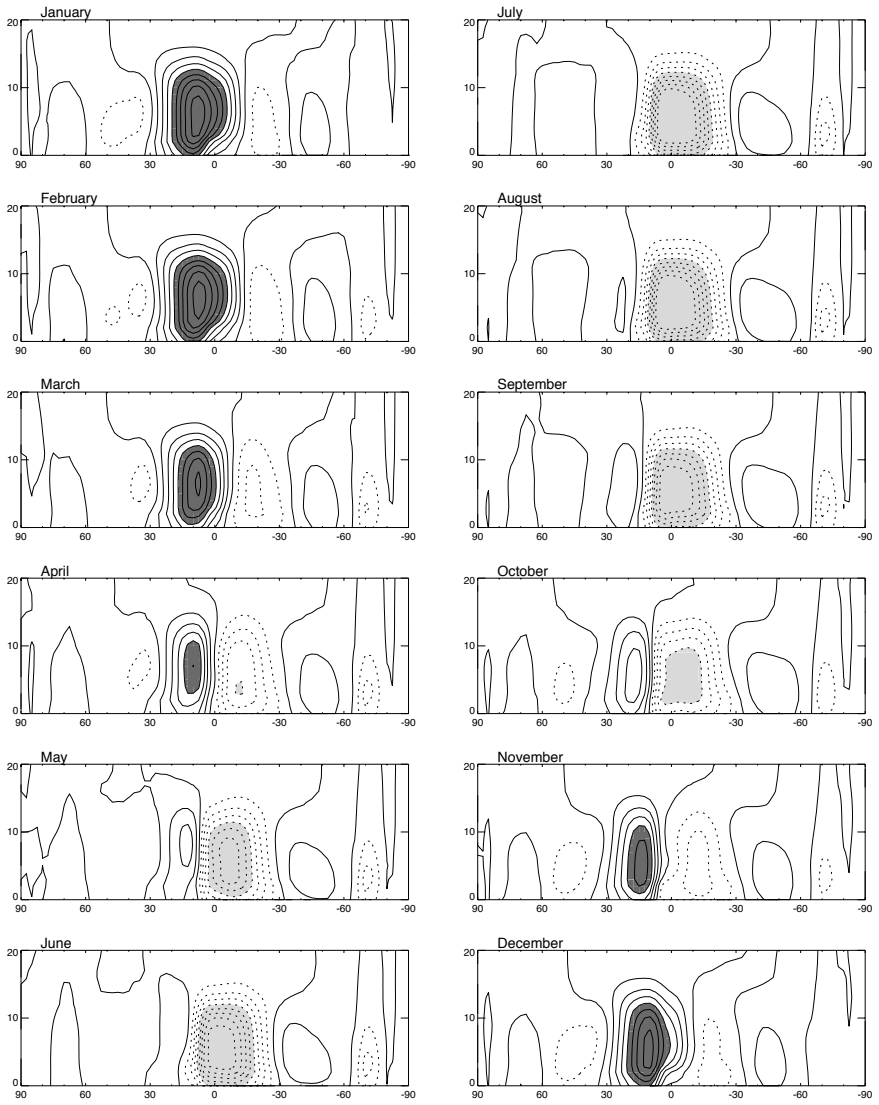

Figure 3.19: Seasonal change of the stream function of the mean meridional circulation. The contour interval is 25 x 10^{12} g s^{-1}. Shading is used for values larger than 100 x 10^{12} g s^{-1} and smaller than -100 x 10^{12} g s^{-1}. A similar figure appeared in Dima and Wallace (2003).

cold temperatures are found above the winter pole, especially in the Southern Hemisphere. The summer pole is much warmer due to the absorption of solar radiation by ozone.

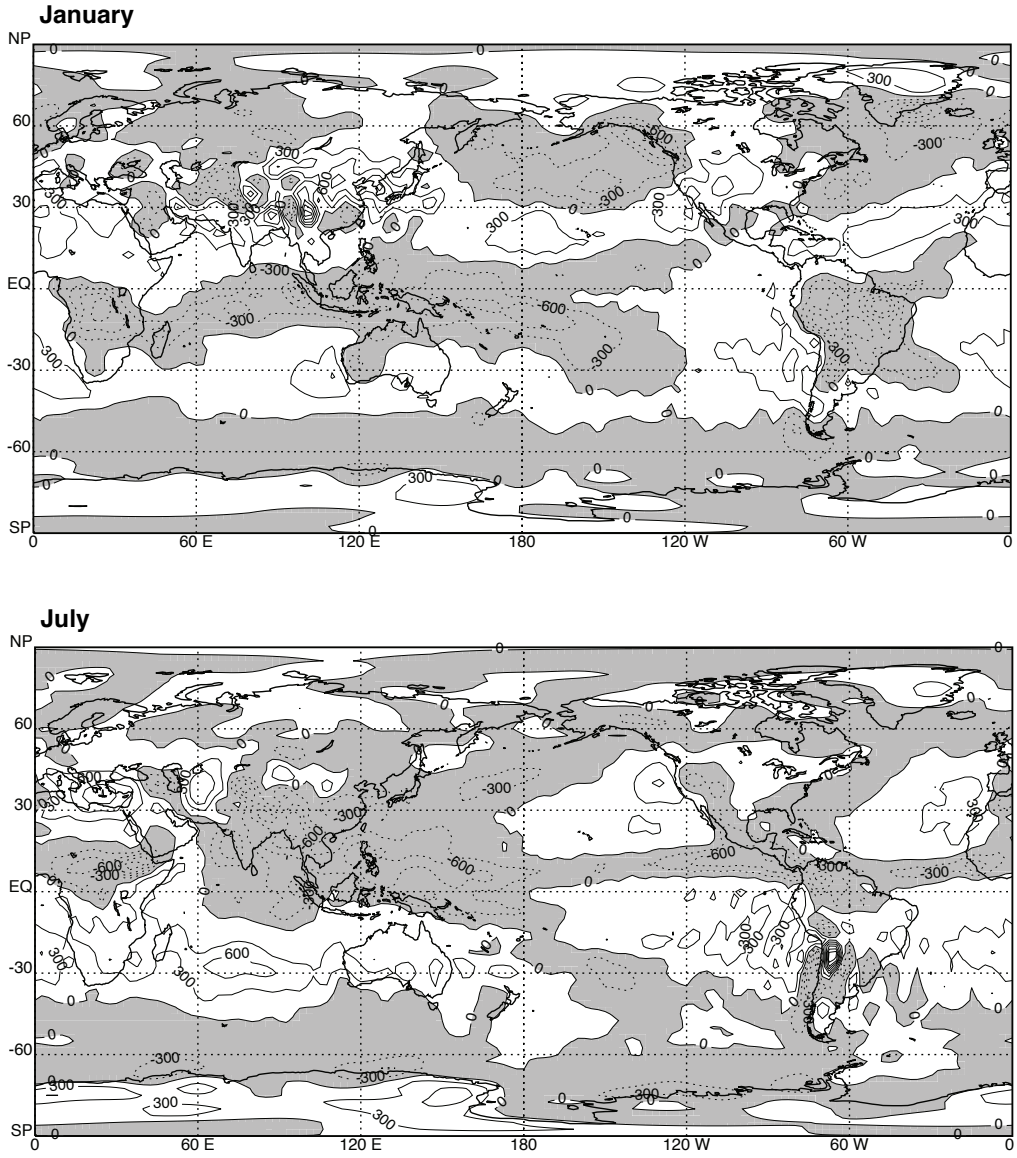

Figure 3.20: Maps of ω, the vertical "pressure velocity," for the 500 hPa surface. The units are nb s^{-1}. Negative values (corresponding to rising motion) are shaded.

It has been suggested that, for a wide class of sufficiently massive atmospheres, the tropopause must occur near the 100 hPa level, because at higher pressures the atmosphere is relatively opaque to the thermal infrared radiation, while at lower pressures it is relatively transparent (Robinson and Catling, 2013).

The midlatitude low-level temperature gradients are quite strong in the winter hemi-

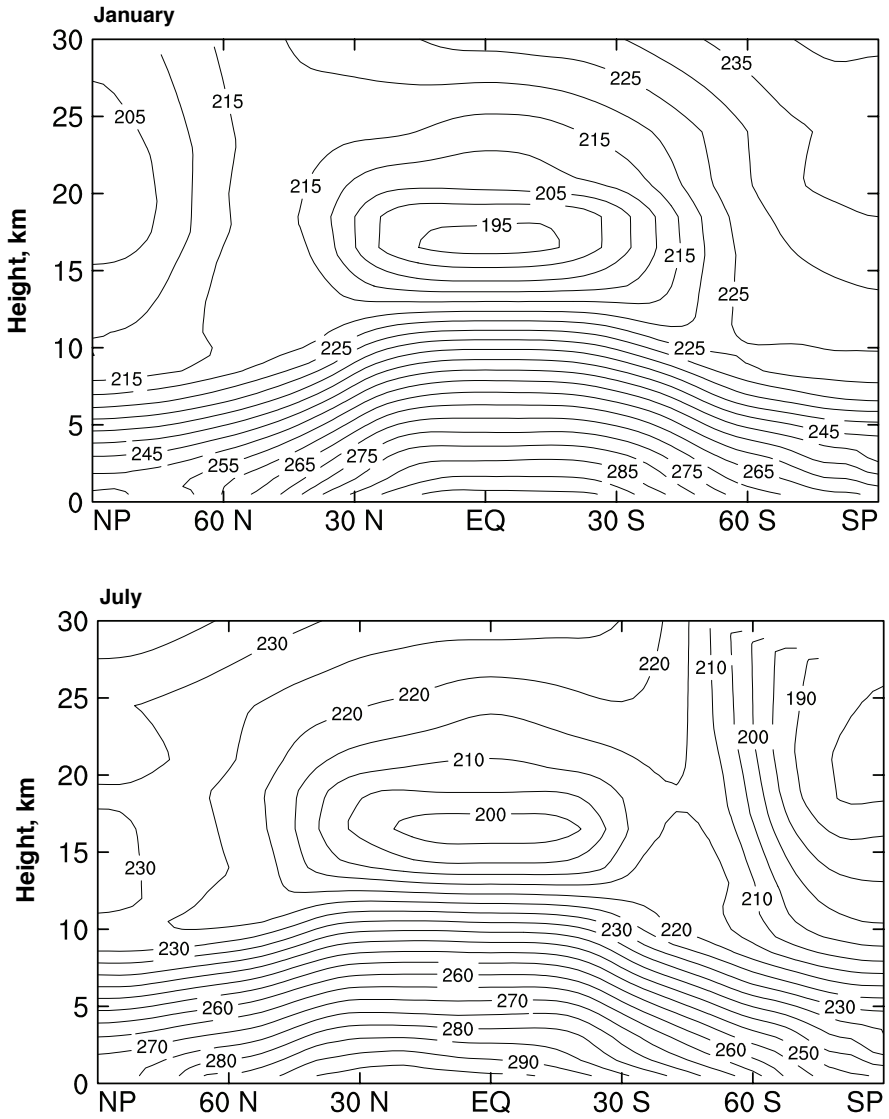

Figure 3.21: Latitude-height cross sections of temperature, for January and July. The contour interval is 5 K.

sphere. Above 200 hPa, the summer pole is considerably warmer than the winter pole; in fact, the zonally averaged temperature increases monotonically from the Equator to the summer pole near 100 hPa. This suggests easterlies in the summer stratosphere, which are observed. In the winter hemisphere, the warmest 100 hPa temperatures occur in middle latitudes. The strong decrease of temperature between midlatitudes and the poles is consistent with the polar night jets mentioned earlier.

Generally speaking, the lapse rate, $-\partial T/\partial z$, is largest in the tropics, and smaller (or even negative) near the poles. In January, a temperature "inversion" (i.e., temperature

increasing upward) appears at low levels near the North Pole.

The thermal wind equations relate the vertical shear of the geostrophic wind to the horizontal temperature gradient. They are given by

$$\frac{\partial u_g}{\partial p} = \frac{R}{fpa}\left(\frac{\partial T}{\partial \varphi}\right)_p \tag{3.27}$$

and

$$\frac{\partial v_g}{\partial p} = \frac{-R}{fpa\cos\varphi}\left(\frac{\partial T}{\partial \lambda}\right)_p. \tag{3.28}$$

Thermal wind balance between the meridional temperature gradient and the vertical shear of the zonal wind is well satisfied. This can be qualitatively confirmed by comparison of Fig. 3.6 and Fig. 3.21.

Fig. 3.22 shows maps of the 850 hPa temperature for January and July, and Fig. 3.23 shows the corresponding results for 200 hPa. The expected winter-to-summer warming at 850 hPa is clearly evident in the Northern Hemisphere, but not in the Southern Hemisphere, except over land. Monthly mean temperatures over the high Antarctic terrain reach about -50°C in July, while those over the Arctic ocean in January do not fall below -35°C. In the tropics there is very little seasonal change, and the temperature distribution is very uniform, for reasons that we have already discussed.

Naturally, the temperature gradient points mainly from the poles toward the tropics at 850 hPa, but wavy patterns are plainly visible in the Northern Hemisphere in January. There are some regions in which the mean temperature actually increases poleward, at 850 hPa, e.g., from Northern Africa across to India in July, and north of Australia in January. From thermal wind considerations, we might expect easterlies aloft in these regions. This expectation is borne out in Fig. 3.10. In winter, there is a tendency for the eastern sides of the Northern Hemisphere continents to be colder than the western sides. This leads to particularly strong meridional temperature gradients on the east coasts. We know that such strong temperature gradients favor a rapid upward increase of the westerlies; also, such highly baroclinic regions are preferred centers of cyclogenesis.

The strongest temperature gradients at 200 hPa are found in high latitudes, especially in winter. The wave-like eddy pattern is much stronger at 200 hPa than at 850 hPa. Particularly noticeable are the maxima over the North Pacific in January, over eastern North America in January, and over southern Asia in July. Note that in each of these regions the 200 hPa temperature increases as we move from the tropics towards middle latitudes. This implies a tendency for the westerlies to weaken above this level.

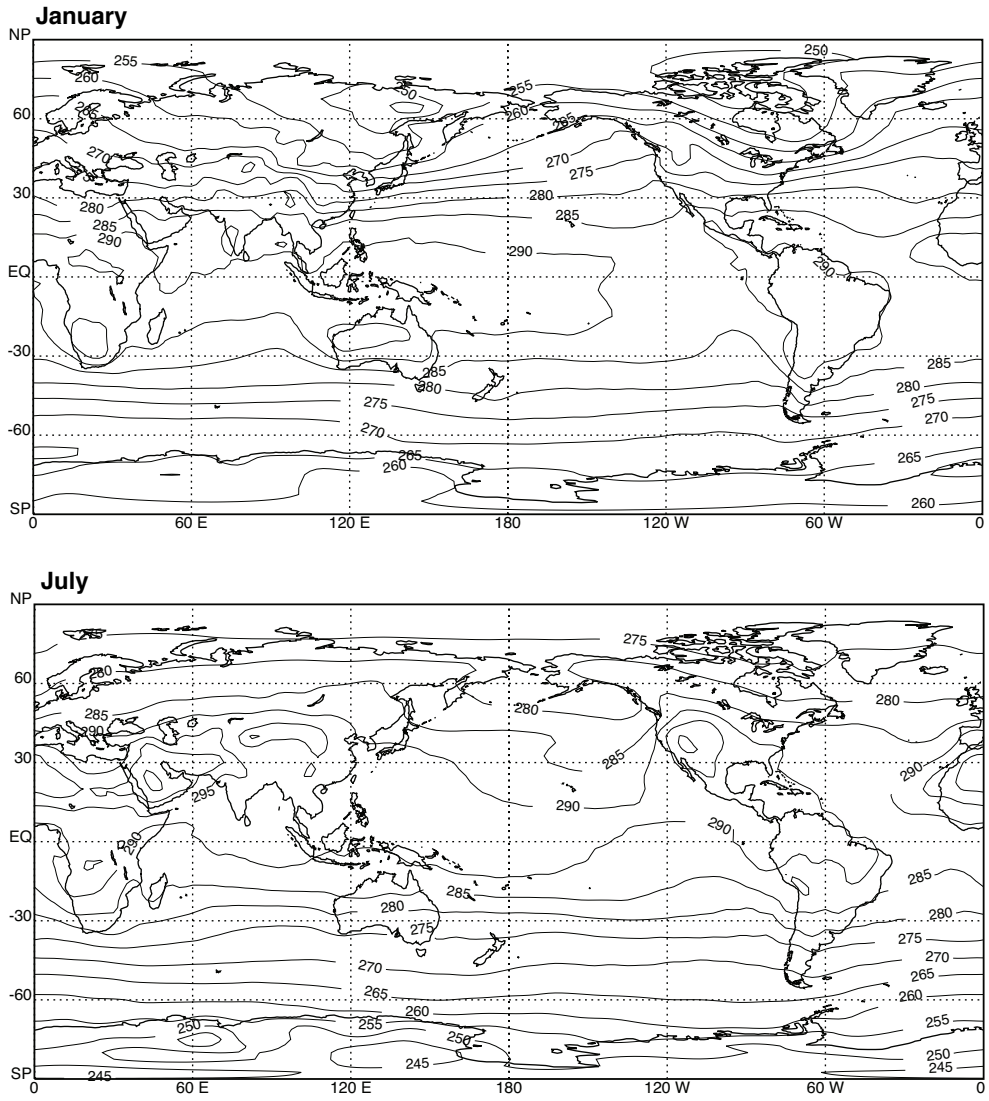

Figure 3.22: Maps of the 850 hPa temperature for January and July. The contour interval is 5 K.

Recall that the potential temperature is defined by

$$\theta \equiv T\left(\frac{p_0}{p}\right)^{\kappa}, \tag{3.29}$$

where p_0 is a constant reference pressure, usually chosen to be 1000 hPa, and $\kappa = R/c_p$, where R is the gas constant and c_p is the specific heat of air at constant pressure. As discussed in Chapter 4, important facts about the potential temperature are that it is conserved under dry adiabatic processes, and that (with minor exceptions) it increases upward

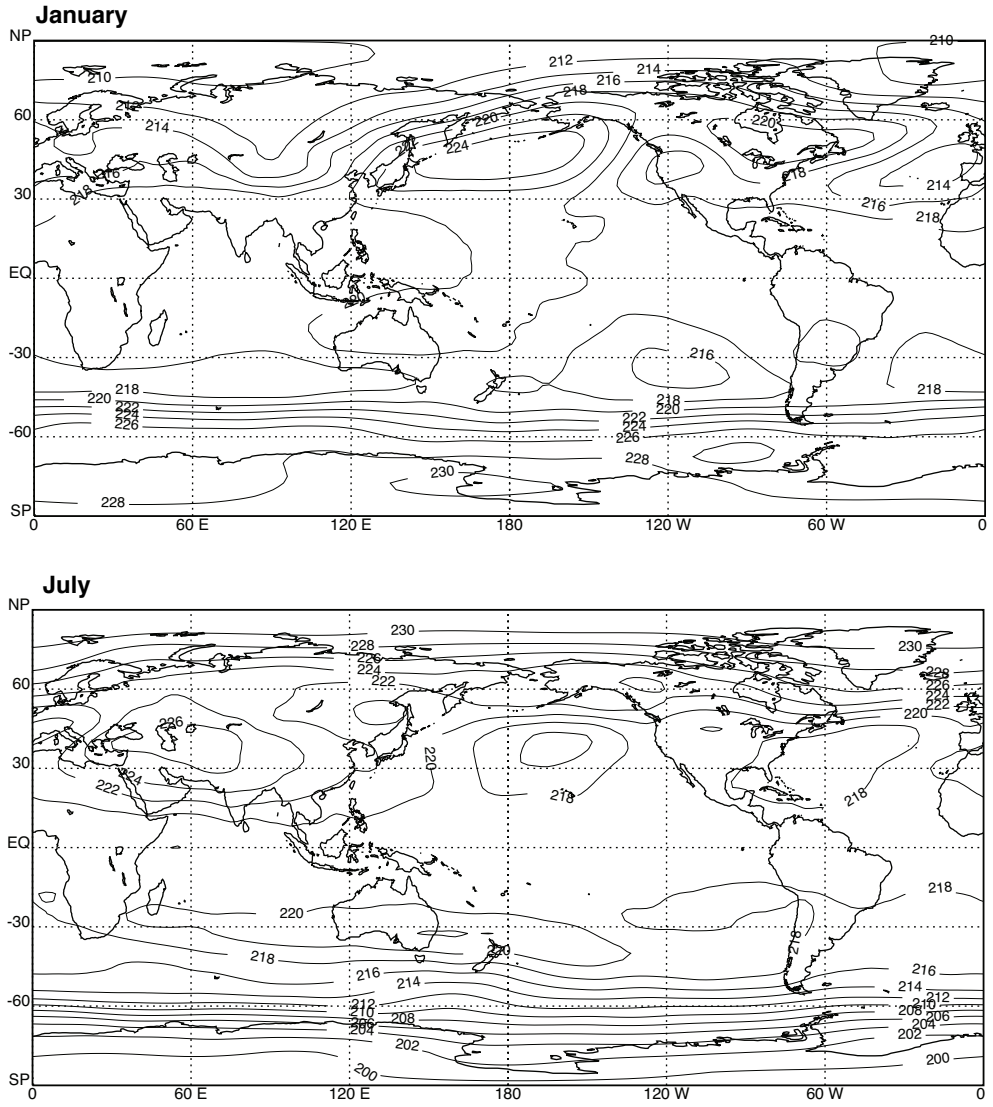

Figure 3.23: Maps of the 200 hPa temperature for January and July. The contour interval is 5 K.

throughout the atmosphere. This upward increase is evident in Fig. 3.24. In the troposphere, potential temperature surfaces slope downwards from the polar regions to the tropics, while in the stratosphere the opposite occurs. The stratosphere is easily identified because the potential temperature increases upward very sharply there, showing that the static stability is very strong. On the other hand, the static stability is particularly weak in the tropical upper troposphere.

Hoskins (1991) distinguishes the following three regimes, which can be identified in Fig. 3.24: There is an "Overworld," in which by definition the potential temperature sur-

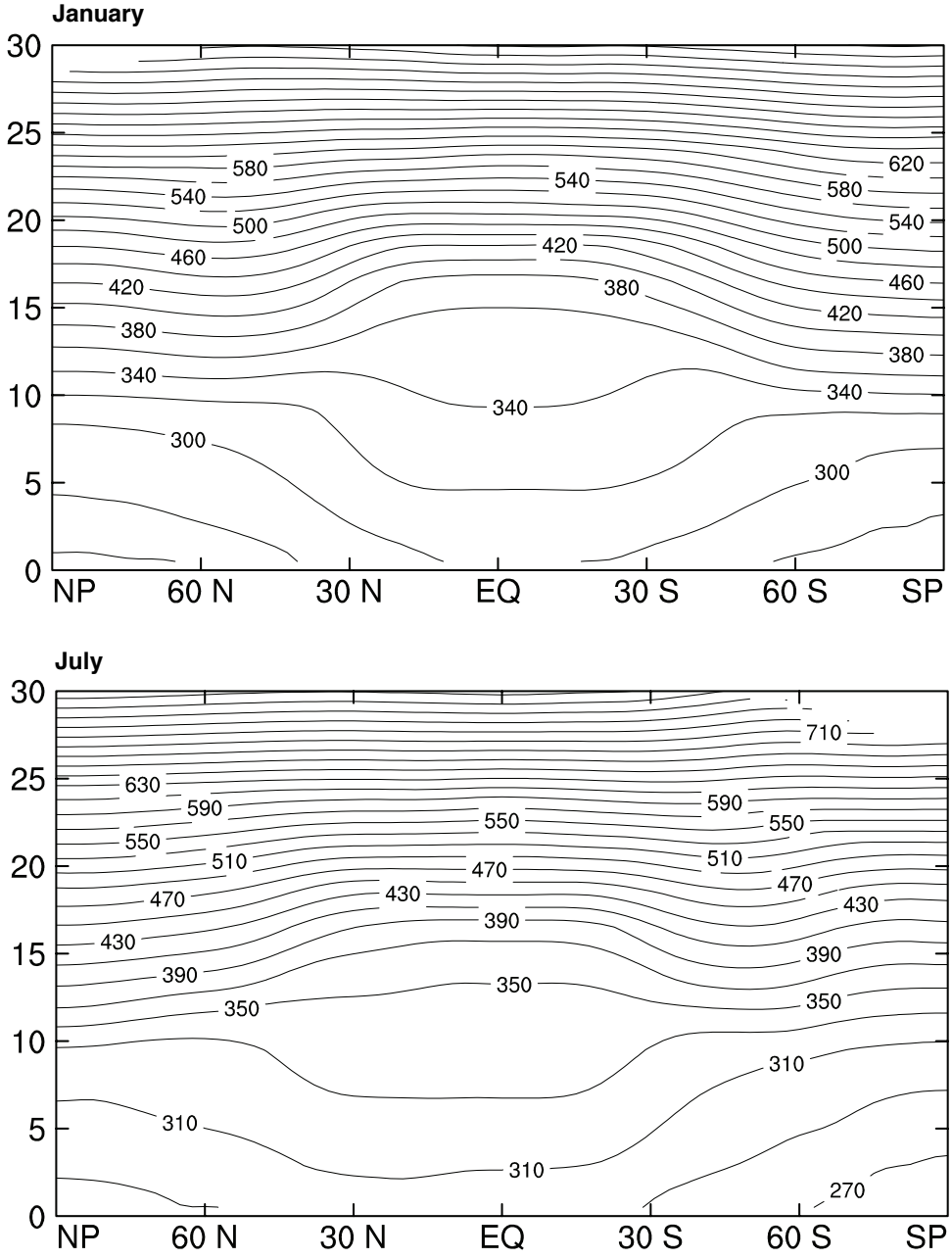

Figure 3.24: Latitude-height cross sections of potential temperature, for January and July. The contour interval is 10 K.

faces are everywhere above the tropopause. From the data, we see that such air has potential temperatures of about 390 K or larger, i.e., the tropical tropopause roughly coincides with the surface on which the potential temperature is 390 K. The "Middleworld" is defined to have potential temperature surfaces that cross the tropopause, which means that air moving

along isentropic surfaces in the Middleworld can move between the troposphere and the stratosphere. The Middleworld is found outside the tropics, in middle latitudes. Finally, the "Underworld" has potential temperature surfaces that intersect the Earth's surface, so that air moving isentropically in the Underworld can "sample" the properties of the Earth's surface and communicate these to the atmosphere. Much of the Underword is found in the high-latitude troposphere. From Fig. 3.24, it appears that the largest potential temperatures in the Underworld are on the order of 300 K, although in reality much larger values of the potential temperature do occur locally near the Earth's surface, e.g., on a summer afternoon in the Sahara desert.

As you may know, potential temperature can be used as a vertical coordinate, and such an approach has many advantages for interpreting the observations, for theoretical analyses, and for numerical modeling (e.g., Hoskins et al., 1985). We will frequently use potential temperature as a vertical coordinate in this book. Chapter 4 introduces the relevant concepts.

3.7 Storm tracks

We need a notation that allows us to distinguish between eddies and zonal means. We will occasionally (but not systematically) distinguish between "stationary" eddies, which are anchored to features (such as mountain ranges) on the Earth's surface, and so appear in time-averaged (e.g. monthly mean) maps, and "transient" eddies that move and so are smeared out to invisibility in sufficiently long time averages. We adopt the notations shown in Table 3.1, some of which have already been used. In the following discussion, we consider various statistics derived from the spatial and temporal distributions of fields called v and T. We use these symbols only for convenience. In principle, v and T can be any variables. They could be the same variable.

As discussed in Appendix C, the zonal mean of the product of two arbitrary variables v and T can be expanded as follows:

$$\overline{vT}^{t,\lambda} = \overline{v}^{t,\lambda}\overline{T}^{t,\lambda} + \overline{\overline{v^*}^t\,\overline{T^*}^t}^{\lambda} + \overline{\overline{v'}^{\lambda}\,\overline{T'}^{\lambda}}^{t} + \overline{v'^*T'^*}^{\lambda,t} \,. \tag{3.30}$$

Here a prime denotes a departure from a time average, and a star denotes a departure from the zonal mean. The terms of (3.30) have the following meanings:

- the term $\overline{v}^{t,\lambda}\overline{T}^{t,\lambda}$ represents the contribution to $\overline{vT}^{t,\lambda}$ from the product of the temporally and zonally averaged values of v and T;

Table 3.1: Terminology used in the discussion of the zonally averaged flow and eddy covariances.

Notation	Meaning
$\overline{(\ )}^t$	Time mean
$(\ )'$	Departure from the time mean, or *transient* component
$\overline{(\ )}^\lambda$	Zonal mean
$(\ )^*$	Departure from the zonal mean, or *eddy* component

- the term $\overline{\overline{v^*}^t\,\overline{T^*}^t}^\lambda$ represents the contribution from "stationary eddies," i.e., eddies that appear in time averages;
- the term $\overline{\overline{v'}^\lambda\,\overline{T'}^\lambda}^t$ represents the contribution from temporal fluctuations of the zonal means, sometimes called the transient symmetric contribution; and
- the term $\overline{v'^*T'^*}^{\lambda,t}$ represents the contribution from "transient eddies," including baroclinic waves in the extratropics.

Finally, the "total eddy" contribution is the sum of the stationary and transient eddy contributions.

Fig. 3.25 shows maps of the transient eddy meridional flux of temperature at 850 hPa, for January (upper panel) and July (lower panel). The plots on the right show the zonal averages. The maxima over the midlatitude oceans in winter are called the "storm tracks." They exist in summer too, but are much weaker (especially in the Nortern Hemisphere) and shifted poleward.

3.8 Moisture

The globally averaged evaporation and precipitation rates, which must balance in a time average, are not accurately known, but are a little less than 3 mm day^{-1}. It follows that

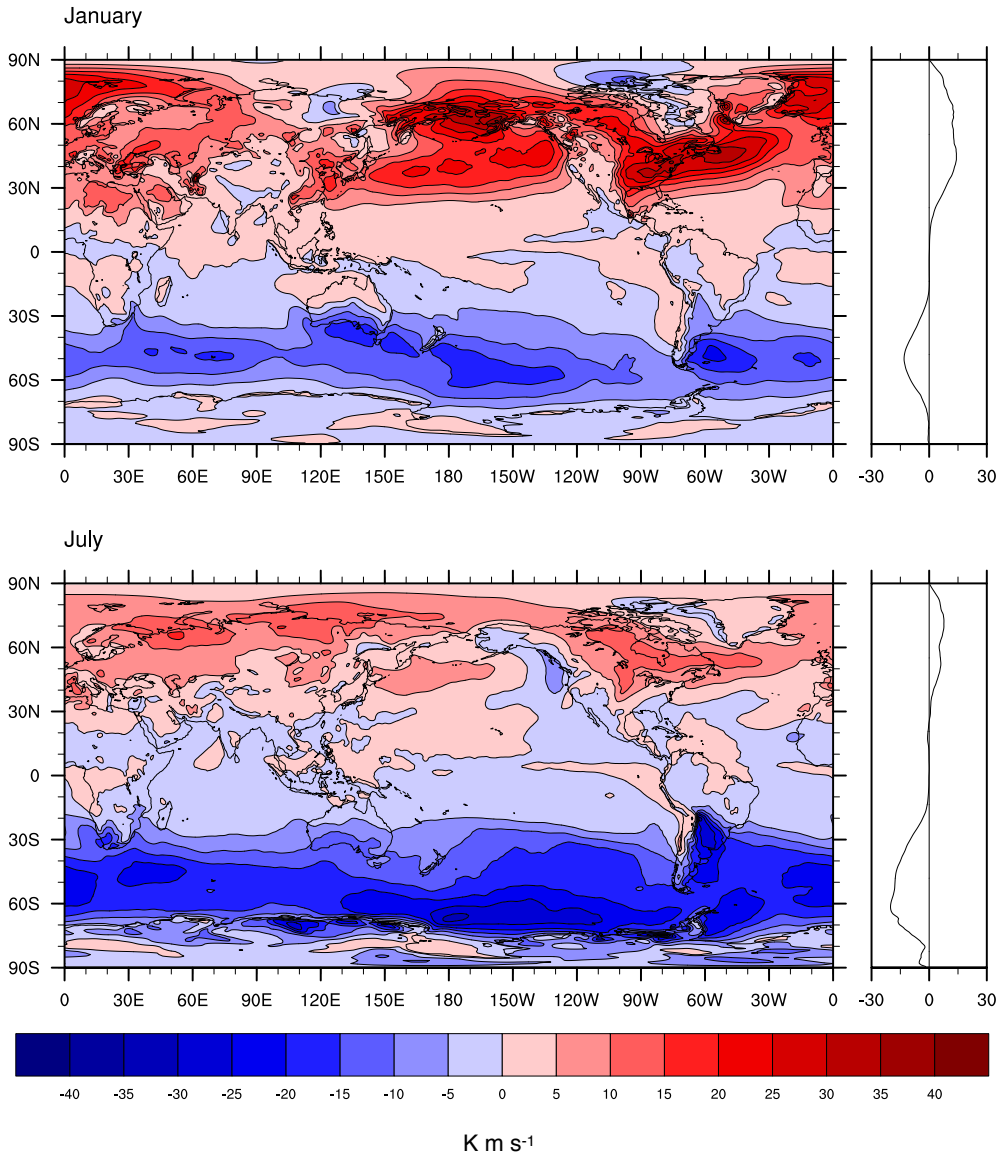

Figure 3.25: Maps of the transient eddy meridional flux of temperature at 850 hPa, for January (upper panel) and July (lower panel). The plots on the right show the zonal averages.

an average water molecule spends a "residence time" of about 8 days in the atmosphere, between its introduction by surface evaporation and its removal by precipitation.

The water vapor mixing ratio is the density of water vapor divided by the density of dry air. Fig. 3.26 shows the latitude-height distributions of the zonally averaged water vapor mixing ratio for January and July, respectively. Caution is needed here, because the data presented in these figures have been fed through the analysis/forecast system of a numerical weather prediction center, which can easily distort the distribution of water

vapor. The figures show the most humid air near the equator, and the driest air near the winter pole. The seasonal change in the Northern Hemisphere is quite dramatic. There is an extremely rapid upward decrease of the mixing ratio at all latitudes. The largest average values, near the surface in the tropics, are close to 18 g kg^{-1}, which means that about 2% of the air is water vapor. Even minute quantities of water vapor in the upper troposphere and stratosphere can be very important radiatively.

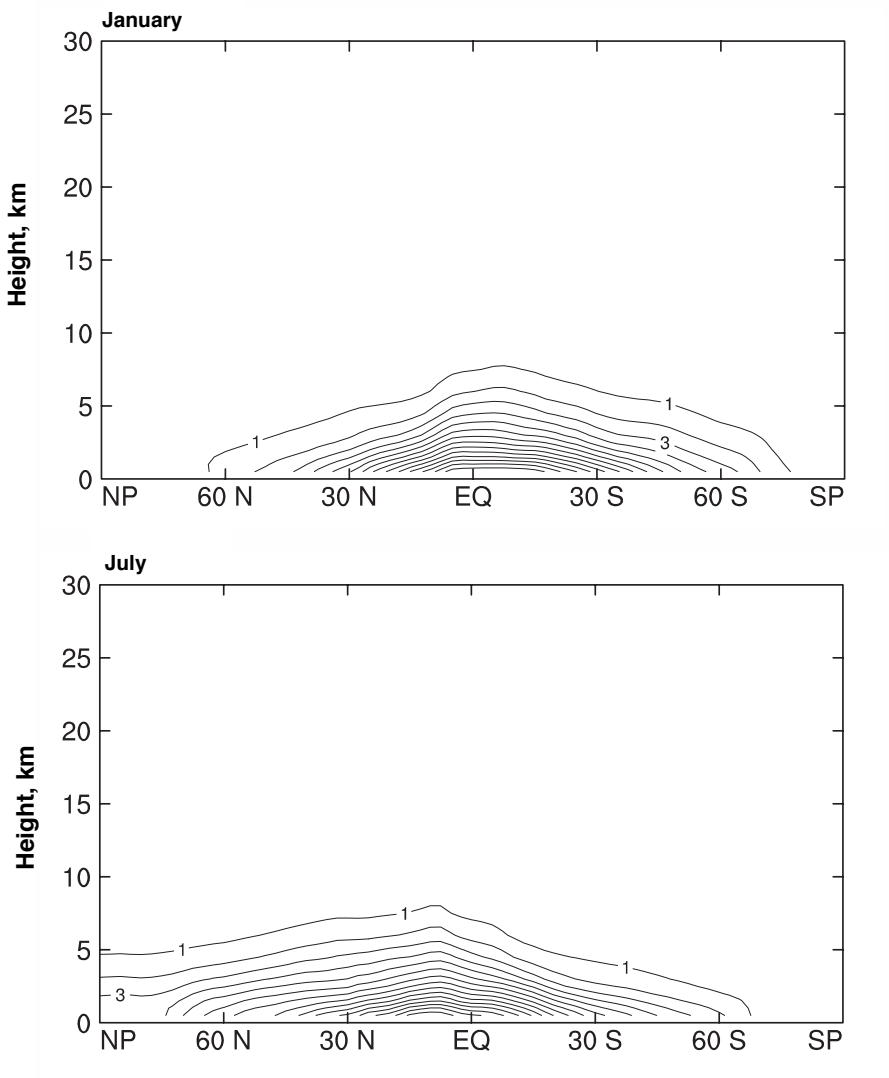

Figure 3.26: Latitude-height section of water vapor mixing ratio. The contour interval is 1 g kg^{-1}.

Because the mixing ratio is greatest near the surface, regions of low-level mass convergence, such as those apparent in the zonally averaged meridional wind, tend to be regions of vertically integrated moisture convergence as well. Although as much mass diverges at

upper levels as converges at lower levels, the diverging air aloft is dry, while the converging air near the surface is humid. A net convergence of water vapor occurs in such regions. The situation is reversed in desert regions, where the dry upper tropospheric air converges and descends.

The vertically integrated water vapor content of the air, with dimensions of mass per unit area, is called the "column water vapor" or "the precipitable water." Fig. 3.27 shows the seasonal cycle of the zonally averaged precipitable water, as a function of latitude. The tropical maxmimum shifts meridionally, favoring the summer hemisphere. The seasonal variations are especially pronouced in the Northern Hemisphere.

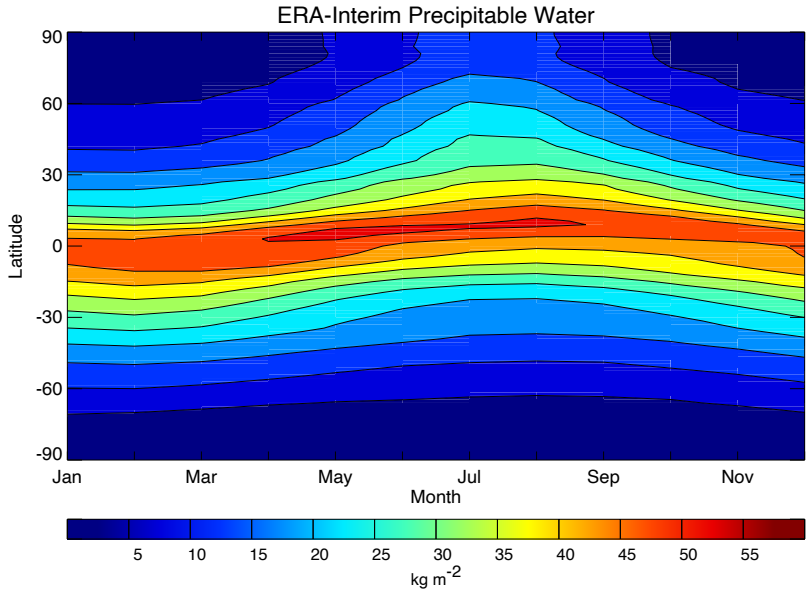

Figure 3.27: the seasonal cycle of the zonally averaged precipitable water, as a function of latitude.

Fig. 3.28 shows maps of the 850 hPa water vapor mixing ratio for January and July, respectively. As would be expected, the largest values occur in the tropics and the summer hemisphere. A very clear maximum extends around the circumference of the Earth in the tropics, mainly somewhat north of the Equator. Meridional moisture gradients are often quite sharp. There are also strong east-west variations, however. For example, in January there are strong maxima over southern Africa and in the Amazon basin. Minima are found in the subtropical highs. There are very dramatic seasonal changes over the midlatitude continents, with larger values in summer. Major desert regions like the Sahara and western North America are clearly associated with water vapor minima.

The relative humidity can be defined as the ratio of the actual water vapor pressure to the saturation vapor pressure; the latter is an increasing function of temperature only, and was introduced in Chapter 2. Locally, a relative humidity of 1 or more, corresponding to water

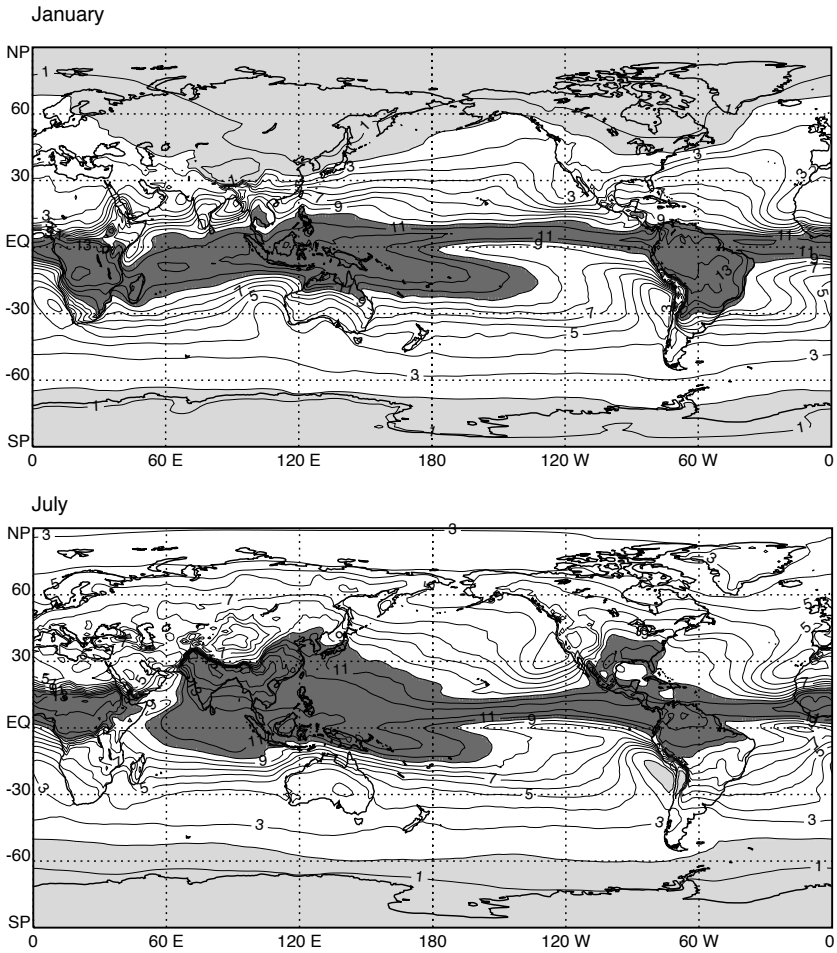

Figure 3.28: Maps of the 850 hPa water vapor mixing ratio. The contour interval is 1 g kg^{-1} . Values larger than 10 g kg^{-1} are darkly shaded.

vapor "saturation," normally indicates the presence of cloud. The zonally averaged relative humidity is shown in Fig. 3.29. The tropical troposphere is very humid in rainy regions of the tropics, and high relative humidities are also found in middle latitudes, especially in winter, where strong low-pressure systems are frequent.

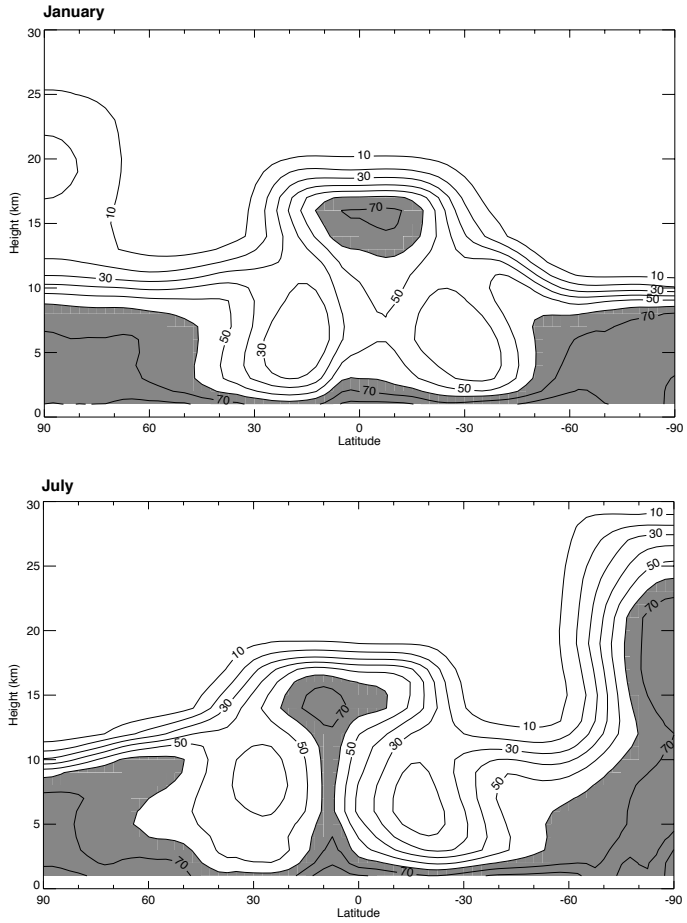

Figure 3.29: The observed latitude-height distribution of the zonally averaged relative humidity, in %, as analyzed by ECMWF. Values larger than 60% are shaded.

3.9 Lots of questions

This chapter is designed to impart some familiarity with basic features of the observed global circulation, but without much attempt to explain why the circulation appears as it does. The observations presented raise many questions. For example:

- What determines the magnitude of the pole-to-equator gradient of the surface temperature?
- Why are seasonal changes generally weaker in the Southern Hemisphere than in the Northern Hemisphere?
- What determines the observed lapse rate of temperature? Why does the lapse rate change as we move from the tropics to the middle latitudes to the poles?
- What determines the intensities and latitudes of the jet streams? Why do the winter

jet maxima occur at particular longitudes?

- Why are the subtropical highs typically found on the eastern sides of the ocean basins?
- Why is the Intertropical Convergence Zone mainly north of the Equator?
- What accounts for the observed patterns of large-scale rising and sinking motion?
- Why is there such a strong belt of low pressure around Antarctica? What determines the locations and intensities of the Aleutian and Icelandic Lows?
- What determines the vertical distribution of water vapor?
- Why is the upper-level circulation "wavy"? Why is the lower-level circulation "lumpy?"
- What determines the height of the tropopause, as a function of latitude? Why is the tropical tropopause so cold? Why does the tropopause height have a discontinuity near the subtropical jets?
- What mechanisms generate the observed variations with longitude of the monthly-mean fields?
- What accounts for the observed large-scale pattern of winds in a monsoon?
- How much do individual Januaries and Julys, for particular years, differ from the "average" January and July conditions shown in this chapter? What causes such year-to-year variations?
- What are the geographical patterns of the day-to-day weather fluctuations that accompany the monthly mean maps shown here, and how do these fluctuations affect the time means?
- Why does the global circulation appear "smooth," rather than "noisy?"

These and many other questions will be discussed in the remainder of this book. To address them, we will need the ideas presented in Chapter 4.

3.10 Problems

1. Estimate the total water vapor content of the atmosphere, in kg. Explain how you arrive at your answer.
2. Make a rough estimate of the total kinetic energy of the atmosphere, in joules. If all of the solar radiation absorbed by the Earth were used to supply this kinetic energy, how long would it take to accumulate the observed amount? Note: In reality the rate of kinetic energy generation in the atmosphere is (fortunately) much less than the rate at which the Earth absorbs solar radiation.

Bibliography

Andrews, D., and M. E. Mcintyre, 1976: Planetary waves in horizontal and vertical shear: The generalized eliassen-palm relation and the mean zonal acceleration. *Journal of Atmospheric Sciences*, **33 (11)**, 2031–2048.

Andrews, D. G., J. R. Holton, and C. B. Leovy, 1987: *Middle atmosphere dynamics*. 40, Academic press.

Arakawa, A., 2004: The cumulus parameterization problem: Past, present, and future. *Journal of climate*, **17 (13)**, 2493–2525.

Arakawa, A., and J.-M. Chen, 1986: Closure assumptions in the cumulus parameterization problem. *Journal of the Meteorological Society of Japan. Ser. II*, **64**, 107–131.

Arakawa, A., and C. S. Konor, 2009: Unification of the anelastic and quasi-hydrostatic systems of equations. *Monthly Weather Review*, **137 (2)**, 710–726.

Arakawa, A., and W. H. Schubert, 1974: Interaction of a cumulus cloud ensemble with the large-scale environment, part i. *Journal of the Atmospheric Sciences*, **31 (3)**, 674–701.

Baldwin, M., and Coauthors, 2001: The quasi-biennial oscillation. *Reviews of Geophysics*, **39 (2)**, 179–229.

Baldwin, M. P., and Coauthors, 2019: 100 years of progress in understanding the stratosphere and mesosphere. *Meteorological Monographs*, **59**, 27–1.

Baldwin, M. P., and Coauthors, 2021: Sudden stratospheric warmings. *Reviews of Geophysics*, **59 (1)**, e2020RG000 708.

Banfield, D., and Coauthors, 2020: The atmosphere of mars as observed by insight. *Nature Geoscience*, **13**, 190–198.

Bangalath, H., and O. Pauluis, 2020: A new mass flux correction procedure for vertically integrated energy transport by constraining mass, energy, and water budgets. *Geophysical Research Letters*, **47 (22)**, e2020GL089 764.

Barriopedro, D., and N. Calvo, 2014: On the relationship between enso, stratospheric sudden warmings, and blocking. *Journal of Climate*, **27 (12)**, 4704–4720.

Bauer, P., A. J. Thorpe, and G. Brunet, 2015: The quiet revolution of numerical weather prediction. *Nature*, **525**, 47–55.

Bengtsson, L., and J. Shukla, 1988: Integration of space and in situ observations to study global climate change. *Bulletin of the American Meteorological Society*, **69 (10)**, 1130–1143.

Bengtsson, L., and Coauthors, 2007: The need for a dynamical climate reanalysis. *Bulletin of the American Meteorological Society*, **88 (4)**, 495–501.

Benjamin, S. G., G. A. Grell, J. M. Brown, T. G. Smirnova, and R. Bleck, 2004: Mesoscale weather prediction with the ruc hybrid isentropic–terrain-following coordinate model. *Monthly Weather Review*, **132 (2)**, 473–494.

Beres, J. H., R. R. Garcia, B. A. Boville, and F. Sassi, 2005: Implementation of a gravity wave source spectrum parameterization dependent on the properties of convection in the whole atmosphere community climate model (waccm). *Journal of Geophysical Research: Atmospheres*, **110 (D10)**.

Berry, M., 2002: Singular limits. *Physics Today*, **55 (5)**, 10–11.

Bister, M., and K. A. Emanuel, 1998: Dissipative heating and hurricane intensity. *Meteorology and Atmospheric Physics*, **65 (3)**, 233–240.

Bjerknes, J., 1938: Saturated-adiabatic ascent of air through dry-adiabatically descending environment. *Quart. J. Roy. Meteor. Soc.*, **64**, 325–330.

Bjerknes, J., 1948: Practical application of h. jeffrey's theory of the general circulation. *Jeffreys' theory of the general circulation. Programme et R4sum6 des M6moires, R6union d'Osto, Assoc. M6t6or., UGGI, Geneva*, 13–14.

Blackmon, M. L., 1976: A climatological spectral study of the 500 mb geopotential height of the northern hemisphere. *Journal of the Atmospheric Sciences*, **33 (8)**, 1607–1623.

Bleck, R., 1973: Numerical forecasting experiments based on the conservation of potential vorticity on isentropic surfaces. *Journal of Applied Meteorology*, **12 (5)**, 737–752.

Bowman, K. P., and P. J. Cohen, 1997: Interhemispheric exchange by seasonal modulation of the Hadley circulation. *Journal of the atmospheric sciences*, **54 (16)**, 2045–2059.

Bretherton, C. S., and C. Schär, 1993: Flux of potential vorticity substance: A simple derivation and a uniqueness property. *Journal of the atmospheric sciences*, **50**, 1834–1834.

Bretherton, F. P., 1966: Critical layer instability in baroclinic flows. *Quarterly Journal of the Royal Meteorological Society*, **92 (393)**, 325–334.

Bryan, F. O., 1997: The axial angular momentum balance of a global ocean general circulation model. *Dynamics of atmospheres and oceans*, **25 (3)**, 191–216.

Bukowinski, M. S., 1999: Earth science: Taking the core temperature. *Nature*, **401 (6752)**, 432.

Businger, S., and J. A. Businger, 2001: Viscous dissipation of turbulence kinetic energy in storms. *Journal of the atmospheric sciences*, **58 (24)**, 3793–3796.

Butchart, N., 2014: The brewer-dobson circulation. *Reviews of geophysics*, **52 (2)**, 157–184.

Carissimo, B., A. Oort, and T. Vonder Haar, 1985: Estimating the meridional energy transports in the atmosphere and ocean. *Journal of Physical Oceanography*, **15 (1)**, 82–91.

Chandrasekhar, S., 2013: *Hydrodynamic and hydromagnetic stability*. Courier Corporation.

Chang, E. K., S. Lee, and K. L. Swanson, 2002: Storm track dynamics. *Journal of climate*, **15 (16)**, 2163–2183.

Charlton, A. J., and L. M. Polvani, 2007: A new look at stratospheric sudden warmings. part i: Climatology and modeling benchmarks. *Journal of climate*, **20 (3)**, 449–469.

Charney, J. G., 1963: A note on large-scale motions in the tropics. *Journal of the Atmospheric Sciences*, **20 (6)**, 607–609.

Charney, J. G., 1971: Geostrophic turbulence. *Journal of the Atmospheric Sciences*, **28 (6)**, 1087–1095.

Charney, J. G., 1990: On the scale of atmospheric motions. *The Atmosphere—A Challenge*, Springer, 251–265.

Charney, J. G., and J. G. DeVore, 1979: Multiple flow equilibria in the atmosphere and blocking. *Journal of Atmospheric Sciences*, **36 (7)**, 1205–1216.

Charney, J. G., and P. G. Drazin, 1961: Propagation of planetary-scale disturbances from the lower into the upper atmosphere. *Journal of Geophysical Research*, **66 (1)**, 83–109.

Chavas, D. R., and J. Peters, 2023: Static energy deserves greater emphasis in the meteorology community. *Bulletin of the American Meteorological Society*, **104 (10)**, E1918–E1927.

Chavas, D. R., and K. A. Reed, 2019: Dynamical aquaplanet experiments with uniform thermal forcing: System dynamics and implications for tropical cyclone genesis and size. *Journal of the Atmospheric Sciences*, **76 (8)**, 2257–2274.

Chikira, M., 2014: Eastward-propagating intraseasonal oscillation represented by chikira–sugiyama cumulus parameterization. part ii: Understanding moisture variation under weak temperature gradient balance. *Journal of the Atmospheric Sciences*, **71 (2)**, 615–639.

Cripe, D. G., and D. A. Randall, 2001: Joint variations of temperature and water vapor over the midlatitude continents. *Geophysical research letters*, **28 (13)**, 2613–2616.

Cronin, T. W., and D. R. Chavas, 2019: Dry and semidry tropical cyclones. *Journal of the Atmospheric Sciences*, **76 (8)**, 2193–2212.

Crowley, T. J., and G. R. North, 1991: *Paleoclimatology*. New York, NY (United States); Oxford University Press.

Dee, D. P., and Coauthors, 2011: The era-interim reanalysis: Configuration and performance of the data assimilation system. *Quarterly Journal of the royal meteorological society*, **137 (656)**, 553–597.

Defant, A., 1921: Die zirkulation der atmosphäre in den gemässigten breiten der erde: Grundzüge einer theorie der klimaschwankungen. *Geografiska Annaler*, **3 (3)**, 209–266.

Denning, A. S., I. Y. Fung, and D. Randall, 1995: Latitudinal gradient of atmospheric co2 due to seasonal exchange with land biota. *Nature*, **376 (6537)**, 240–243.

Denning, A. S., T. Takahashi, and P. Friedlingstein, 1999: Can a strong atmospheric co2 rectifier effect be reconciled with a "reasonable" carbon budget? keynote perspective. *Tellus B*, **51 (2)**, 249–253.

Dima, I. M., and J. M. Wallace, 2003: On the seasonality of the Hadley cell. *Journal of the atmospheric sciences*, **60 (12)**, 1522–1527.

Dole, R. M., 1986: The life cycles of persistent anomalies and blocking over the north Pacific. *Advances in Geophysics*, Vol. 29, Elsevier, 31–69.

Dove, H. W., 1837: *Meteorologische Untersuchungen*. Sanderischen Buchhandlung.

Dutton, J. A., 2002: *The ceaseless wind: An introduction to the theory of atmospheric motion*. Courier Corporation.

Edouard, S., R. Vautard, and G. Brunet, 1997: On the maintenance of potential vorticity in isentropic coordinates. *Quarterly Journal of the Royal Meteorological Society*, **123 (543)**, 2069–2094.

Egger, J., and K.-P. Hoinka, 2008: The angular momentum budget of the transformed eulerian mean equations. *Journal of the atmospheric sciences*, **65 (10)**, 3305–3314.

Egger, J., W. Metz, and G. Moller, 1986: Forcing of planetary-scale blocking anticyclones by synoptic-scale eddies. *Advances in Geophysics*, Vol. 29, Elsevier, 183–198.

Egger, J., K. Weickmann, and K.-P. Hoinka, 2007: Angular momentum in the global atmospheric circulation. *Reviews of Geophysics*, **45 (4)**.

Eliasen, E., and B. Machenhauer, 1965: A study of the fluctuations of the atmospheric planetary flow patterns represented by spherical harmonics. *Tellus*, **17 (2)**, 220–238.

Eliassen, A., and E. Palm, 1961: On the transfer of energy in stationary mountain waves. geofysike publikasjoner. *Geophysica Norvegica*, **22**.

Eliassen, A., and E. Raustein, 1968: A numerical integration experiment with a model atmosphere based on isentropic surfaces. *Meteorologiske Annaler*, **5**, 45–63.

Emanuel, K., and D. Raymond, 1993: *The presentation of cumulus convection in numerical models, Monogr*. American Meteorological Society.

Emanuel, K., and Coauthors, 2005: *Divine wind: the history and science of hurricanes*. Oxford university press.

Emanuel, K. A., 1979: Inertial instability and mesoscale convective systems. part i: Linear theory of inertial instability in rotating viscous fluids. *Journal of the Atmospheric Sciences*, **36 (12)**, 2425–2449.

Emanuel, K. A., 1982: Inertial instability and mesoscale convective systems. part ii. symmetric cisk in a baroclinic flow. *Journal of Atmospheric Sciences*, **39 (5)**, 1080–1097.

Emanuel, K. A., 1983: On assessing local conditional symmetric instability from atmospheric soundings. *Monthly weather review*, **111 (10)**, 2016–2033.

Emanuel, K. A., 1987: The dependence of hurricane intensity on climate. *Nature*, **326 (6112)**, 483–485.

Fovell, R., D. Durran, and J. Holton, 1992: Numerical simulations of convectively generated stratospheric gravity waves. *Journal of Atmospheric Sciences*, **49 (16)**, 1427–1442.

Gelaro, R., and Coauthors, 2017: The modern-era retrospective analysis for research and applications, version 2 (merra-2). *Journal of climate*, **Volume 30 Iss 13**, 5419–5454.

Gent, P. R., and J. C. Mcwilliams, 1990: Isopycnal mixing in ocean circulation models. *Journal of Physical Oceanography*, **20 (1)**, 150–155.

Gettelman, A., P. Hoor, L. Pan, W. Randel, M. I. Hegglin, and T. Birner, 2011: The extratropical upper troposphere and lower stratosphere. *Reviews of Geophysics*, **49 (3)**.

Gettelman, A., and Coauthors, 2009: The tropical tropopause layer 1960–2100. *Atmospheric Chemistry and Physics*, **9 (5)**, 1621–1637.

Gettelman, A., and Coauthors, 2019: The whole atmosphere community climate model version 6 (waccm6). *Journal of Geophysical Research: Atmospheres*, **124 (23)**, 12 380–12 403.

Gill, A. E., 1980: Some simple solutions for heat-induced tropical circulation. *Quarterly Journal of the Royal Meteorological Society*, **106 (449)**, 447–462.

Gleick, J., 2008: *Chaos: Making a new science*. Penguin.

Grell, G. A., Y.-H. Kuo, and R. J. Pasch, 1991: Semiprognostic tests of cumulus parameterization schemes in the middle latitudes. *Monthly weather review*, **119 (1)**, 5–31.

Hack, J. J., W. H. Schubert, and P. L. S. Dias, 1984: A spectral cumulus parameterization for use in numerical models of the tropical atmosphere. *Monthly weather review*, **112 (4)**, 704–716.

Hack, J. J., W. H. Schubert, D. E. Stevens, and H.-C. Kuo, 1989: Response of the Hadley circulation to convective forcing in the itcz. *Journal of Atmospheric Sciences*, **46 (19)**, 2957–2973.

Hansen, A. R., and T.-C. Chen, 1982: A spectral energetics analysis of atmospheric blocking. *Monthly Weather Review*, **110 (9)**, 1146–1165.

Harper, K. C., 2012: *Weather by the numbers: the genesis of modern meteorology*. mit Press.

Haynes, P. H., and M. E. McIntyre, 1987: On the evolution of vorticity and potential vorticity in the presence of diabatic heating and frictional or other forces. *Journal of the Atmospheric Sciences*, **44 (5)**, 828–841.

Held, I. M., and B. J. Hoskins, 1985: Large-scale eddies and the general circulation of the troposphere. *Advances in geophysics*, Vol. 28, Elsevier, 3–31.

Held, I. M., and B. J. Soden, 2006: Robust responses of the hydrological cycle to global warming. *Journal of climate*, **19 (21)**, 5686–5699.

Hersbach, H., and Coauthors, 2020: The era5 global reanalysis. *Quarterly Journal of the Royal Meteorological Society*, **146 (730)**, 1999–2049.

Hess, S., R. Henry, C. B. Leovy, J. Ryan, and J. E. Tillman, 1977: Meteorological results from the surface of mars: Viking 1 and 2. *Journal of Geophysical Research*, **82 (28)**, 4559–4574.

Hide, R., and J. O. Dickey, 1991: Earth's variable rotation. *Science*, **253 (5020)**, 629–637.

Holton, J. R., 1973: An introduction to dynamic meteorology. *American Journal of Physics*, **41 (5)**, 752–754.

Holton, J. R., 1980: The dynamics of sudden stratospheric warmings. *Annual Review of Earth and Planetary Sciences*, **8 (1)**, 169–190.

Holton, J. R., and R. S. Lindzen, 1972: An updated theory for the quasi-biennial cycle of the tropical stratosphere. *Journal of Atmospheric Sciences*, **29 (6)**, 1076–1080.

Hoskins, B. J., 1991: Towards a PV-θ view of the general circulation. *Tellus A: Dynamic Meteorology and Oceanography*, **43 (4)**, 27–36.

Hoskins, B. J., I. N. James, and G. H. White, 1983: The shape, propagation and mean-flow interaction of large-scale weather systems. *Journal of Atmospheric Sciences*, **40 (7)**, 1595–1612.

Hoskins, B. J., M. McIntyre, and A. W. Robertson, 1985: On the use and significance of isentropic potential vorticity maps. *Quarterly Journal of the Royal Meteorological Society*, **111 (470)**, 877–946.

Hsu, Y.-J. G., and A. Arakawa, 1990: Numerical modeling of the atmosphere with an isentropic vertical coordinate. *Monthly Weather Review*, **118 (10)**, 1933–1959.

Hu, Y., D. Yang, and J. Yang, 2008: Blocking systems over an aqua planet. *Geophysical research letters*, **35 (19)**.

Hung, M.-P., J.-L. Lin, W. Wang, D. Kim, T. Shinoda, and S. J. Weaver, 2013: Mjo and convectively coupled equatorial waves simulated by cmip5 climate models. *Journal of Climate*, **26 (17)**, 6185–6214.

Hurrell, J. W., and C. Deser, 2010: North atlantic climate variability: the role of the north atlantic oscillation. *Journal of marine systems*, **79 (3-4)**, 231–244.

Hurrell, J. W., Y. Kushnir, G. Ottersen, and M. Visbeck, 2003: An overview of the north atlantic oscillation. *Geophysical Monograph-American Geophysical Union*, **134**, 1–36.

Hurrell, J. W., Y. Kushnir, and M. Visbeck, 2001: The north atlantic oscillation. *Science*, **291 (5504)**, 603–605.

Igel, M. R., and J. A. Biello, 2020: The nontraditional coriolis terms and tropical convective clouds. *Journal of Atmospheric Sciences*, **77 (12)**, 3985–3998.

Imbrie, J., and K. P. Imbrie, 1986: *Ice ages: solving the mystery*. Harvard University Press.

Iribarne, J. V., and W. L. Godson, 1981: *Atmospheric thermodynamics*, Vol. 6. Springer Science & Business Media.

Jayne, S. R., D. Roemmich, N. Zilberman, S. C. Riser, K. S. Johnson, G. C. Johnson, and S. R. Piotrowicz, 2017: The argo program: present and future. *Oceanography*, **30 (2)**, 18–28.

Jeffreys, H., 1926: On the dynamics of geostrophic winds. *Quart. J. Roy. Meteor. Soc*, **52 (217)**, 85–104.

Johnson, D. R., 1989: The forcing and maintenance of global monsoonal circulations: An isentropic analysis. *Advances in Geophysics*, Vol. 31, Elsevier, 43–316.

Johnson, D. R., and L. W. Uccellini, 1983: A comparison of methods for computing the sigma-coordinate pressure gradient force for flow over sloped terrain in a hybrid theta-sigma model. *Monthly Weather Review*, **111 (4)**, 870–886.

Jones, T. R., and D. A. Randall, 2011: Quantifying the limits of convective parameterizations. *Journal of Geophysical Research: Atmospheres*, **116 (D8)**.

Juckes, M., 2001: A generalization of the transformed eulerian-mean meridional circulation. *Quarterly Journal of the Royal Meteorological Society*, **127 (571)**, 147–160.

Kalnay, E., and Coauthors, 1996: The ncep/ncar 40-year reanalysis project. *Renewable Energy*.

Kao, C.-Y. J., and Y. Ogura, 1987: Response of cumulus clouds to large-scale forcing using the arakawa-schubert cumulus parameterization. *Journal of Atmospheric Sciences*, **44 (17)**, 2437–2458.

Khairoutdinov, M., and K. Emanuel, 2013: Rotating radiative-convective equilibrium simulated by a cloud-resolving model. *Journal of Advances in Modeling Earth Systems*, **5 (4)**, 816–825.

Kim, D., and Coauthors, 2009: Application of mjo simulation diagnostics to climate models. *Journal of Climate*, **22 (23)**, 6413–6436.

Kim, D., and Coauthors, 2014: Process-oriented mjo simulation diagnostic: Moisture sensitivity of simulated convection. *Journal of Climate*, **27 (14)**, 5379–5395.

Klemp, J., and D. Lilly, 1978: Numerical simulation of hydrostatic mountain waves. *Journal of Atmospheric Sciences*, **35 (1)**, 78–107.

Kolmogorov, A. N., 1941: The local structure of turbulence in incompressible viscous fluid for very large reynolds numbers. *Cr Acad. Sci. URSS*, **30**, 301–305.

Krueger, A. J., and R. A. Minzner, 1976: A mid-latitude ozone model for the 1976 US Standard Atmosphere. *Journal of Geophysical Research*, **81 (24)**, 4477–4481.

Kunz, A., P. Konopka, R. Müller, and L. Pan, 2011: Dynamical tropopause based on isentropic potential vorticity gradients. *Journal of Geophysical Research: Atmospheres*, **116 (D1)**.

Landu, K., and E. D. Maloney, 2011: Effect of sst distribution and radiative feedbacks on the simulation of intraseasonal variability in an aquaplanet gcm. *Journal of the Meteorological Society of Japan. Ser. II*, **89 (3)**, 195–210.

Laplace, P. S., 1799: *Traité de mécanique céleste*. de l'Imprimerie de Crapelet.

Laskar, J., 1989: A numerical experiment on the chaotic behaviour of the solar system. *Nature*, **338 (6212)**, 237–238.

Lau, N.-C., 1985: Modeling the seasonal dependence of the atmospheric response to observed el ninos in 1962–76. *Monthly Weather Review*, **113 (11)**, 1970–1996.

Lesieur, M., 2008: Introduction to turbulence in fluid mechanics. *Turbulence in Fluids: Fourth Revised and Enlarged Edition*, 1–23.

Lewis, J., and R. Prinn, 1984: Planets and their atmospheres- origin and evolution(book). *Orlando, FL, Academic Press, Inc.(International Geophysics Series.*, **33**.

Li, T., L. Wang, M. S. Peng, B. Wang, C. Zhang, W. Lau, and H. chi Kuo, 2018: A paper on the tropical intraseasonal oscillation published in 1963 in a chinese journal. *Bulletin of the American Meteorological Society*.

Lilly, D. K., 1968: Models of cloud-topped mixed layers under a strong inversion. *Quarterly Journal of the Royal Meteorological Society*, **94 (401)**, 292–309.

Lilly, D. K., G. Bassett, K. Droegemeier, and P. Bartello, 1998: Stratified turbulence in the atmospheric mesoscales. *Theoretical and computational fluid dynamics*, **11 (3-4)**, 139–153.

Lindzen, R. A., 1990: *Dynamics in atmospheric physics*, Vol. 310. Cambridge University Press Cambridge.

Lindzen, R. S., and J. R. Holton, 1968: A theory of the quasi-biennial oscillation. *Journal of Atmospheric Sciences*, **25 (6)**, 1095–1107.

Lindzen, R. S., and A. V. Hou, 1988: Hadley circulations for zonally averaged heating centered off the equator. *Journal of Atmospheric Sciences*, **45 (17)**, 2416–2427.

Loeb, N. G., J. M. Lyman, G. C. Johnson, R. P. Allan, D. R. Doelling, T. Wong, B. J. Soden, and G. L. Stephens, 2012: Observed changes in top-of-the-atmosphere radiation and upper-ocean heating consistent within uncertainty. *Nature Geoscience*, **5 (2)**, 110–113.

Longuet-Higgins, M. S., 1968: The eigenfunctions of laplace's tidal equation over a sphere. *Philosophical Transactions of the Royal Society of London. Series A, Mathematical and Physical Sciences*, **262 (1132)**, 511–607.

Lord, S. J., 1982: Interaction of a cumulus cloud ensemble with the large-scale environment. part iii: Semi-prognostic test of the arakawa-schubert cumulus parameterization. *Journal of Atmospheric Sciences*, **39 (1)**, 88–103.

Lord, S. J., and A. Arakawa, 1980: Interaction of a cumulus cloud ensemble with the large-scale environment. part ii. *Journal of Atmospheric Sciences*, **37 (12)**, 2677–2692.

Lorenz, E., 1967: The nature and theory of the general circulation of the atmosphere. *World meteorological organization*, **161**.

Lorenz, E. N., 1955: Available potential energy and the maintenance of the general circulation. *Tellus*, **7 (2)**, 157–167.

Lorenz, E. N., 1963: Deterministic nonperiodic flow. *Journal of atmospheric sciences*, **20 (2)**, 130–141.

Lorenz, E. N., 1969: Three approaches to atmospheric predictability. *Bull. Amer. Meteor. Soc*, **50 (3454)**, 349.

Lorenz, E. N., 1982: Atmospheric predictability experiments with a large numerical model. *Tellus*, **34 (6)**, 505–513.

Luo, D., and Z. Chen, 2006: The role of land–sea topography in blocking formation in a block–eddy interaction model. *Journal of the atmospheric sciences*, **63 (11)**, 3056–3065.

Madden, R. A., and P. R. Julian, 1971: Detection of a 40–50 day oscillation in the zonal wind in the tropical pacific. *Journal of Atmospheric Sciences*, **28 (5)**, 702–708.

Madden, R. A., and P. R. Julian, 1972: Description of global-scale circulation cells in the tropics with a 40–50 day period. *Journal of Atmospheric Sciences*, **29 (6)**, 1109–1123.

Madden, R. A., and P. R. Julian, 1994: Observations of the 40–50-day tropical oscillation—a review. *Monthly weather review*, **122 (5)**, 814–837.

Manabe, S., and A. J. Broccoli, 2020: *Beyond Global Warming: How Numerical Models Revealed the Secrets of Climate Change*. Princeton University Press.

Manabe, S., and R. T. Wetherald, 1967: Thermal equilibrium of the atmosphere with a given distribution of relative humidity. *Journal of the Atmospheric Sciences*.

Mapes, B. E., and J. T. Bacmeister, 2012: Diagnosis of tropical biases and the mjo from patterns in the merra analysis tendency fields. *Journal of climate*, **25 (18)**, 6202–6214.

Margot, J.-L., D. B. Campbell, J. D. Giorgini, J. S. Jao, L. G. Snedeker, F. D. Ghigo, and A. Bonsall, 2021: Spin state and moment of inertia of venus. *Nature Astronomy*, 1–8.

Martius, O., L. Polvani, and H. Davies, 2009: Blocking precursors to stratospheric sudden warming events. *Geophysical Research Letters*, **36 (14)**.

Masuda, K., 1988: Meridional heat transport by the atmosphere and the ocean: Analysis of FGGE data. *Tellus A*, **40 (4)**, 285–302.

Matsuno, T., 1966: Quasi-geostrophic motions in the equatorial area. *Journal of the Meteorological Society of Japan. Ser. II*, **44 (1)**, 25–43.

Matsuno, T., 1970: Vertical propagation of stationary planetary waves in the winter northern hemisphere. *Journal of Atmospheric Sciences*, **27 (6)**, 871–883.

Matsuno, T., 1971: A dynamical model of the stratospheric sudden warming. *Journal of Atmospheric Sciences*, **28 (8)**, 1479–1494.

Matsuno, T., and K. Nakamura, 1979: The eulerian-and lagrangian-mean meridional circulations in the stratosphere at the time of a sudden warming. *Journal of the Atmospheric Sciences*, **36 (4)**, 640–654.

McCarthy, G. D., and Coauthors, 2015: Measuring the Atlantic meridional overturning circulation at 26 n. *Progress in Oceanography*, **130**, 91–111.

McDowell, J. C., 2018: The edge of space: Revisiting the Karman Line. *Acta Astronautica*, **151**, 668–677.

McFarlane, N., 1987: The effect of orographically excited gravity wave drag on the general circulation of the lower stratosphere and troposphere. *Journal of Atmospheric Sciences*, **44 (14)**, 1775–1800.

Mullen, S. L., 1987: Transient eddy forcing of blocking flows. *Journal of Atmospheric Sciences*, **44 (1)**, 3–22.

Naegele, A., and D. Randall, 2019: Geographical and seasonal variability of cloud-radiative feedbacks on precipitation. *Journal of Geophysical Research: Atmospheres*, **124 (2)**, 684–699.

Nakamura, H., M. Nakamura, and J. L. Anderson, 1997: The role of high-and low-frequency dynamics in blocking formation. *Monthly Weather Review*, **125 (9)**, 2074–2093.

Nakamura, N., and C. S. Huang, 2018: Atmospheric blocking as a traffic jam in the jet stream. *Science*, **361 (6397)**, 42–47.

Namias, J., and R. G. Stone, 1940: *An introduction to the study of air mass and isentropic analysis*. American Meteorological Society,.

Nastrom, G., and K. S. Gage, 1985: A climatology of atmospheric wavenumber spectra of wind and temperature observed by commercial aircraft. *Journal of the atmospheric sciences*, **42 (9)**, 950–960.

National Oceanic and Atmospheric Administration, 1976: U.S. Standard Atmosphere, 1976. U.S.Government Printing Office, 241 pp.

Neelin, J. D., and I. M. Held, 1987: Modeling tropical convergence based on the moist static energy budget. *Monthly Weather Review*, **115 (1)**, 3–12.

Newell, R. E., J. W. Kidson, D. Vincent, and G. Boer, 1972: The general circulation of the tropical atmosphere and interactions with extratropical latitudes, volume i. MIT Press, 258pp.

Newman, P. A., and E. R. Nash, 2005: The unusual southern hemisphere stratosphere winter of 2002. *Journal of the atmospheric sciences*, **62 (3)**, 614–628.

Ong, H., and P. E. Roundy, 2020: The compressional beta effect: Analytical solution, numerical benchmark, and data analysis. *Journal of the Atmospheric Sciences*, **77 (11)**, 3721–3732.

Oort, A. H., 1989: Angular momentum cycle in the atmosphere–ocean–solid Earth system. *Bulletin of the American Meteorological Society*, **70 (10)**, 1231–1242.

Oort, A. H., and T. H. Vonder Haar, 1976: On the observed annual cycle in the ocean-atmosphere heat balance over the northern hemisphere. *Journal of Physical Oceanography*, **6 (6)**, 781–800.

Pahlavan, H. A., Q. Fu, J. M. Wallace, and G. N. Kiladis, 2021a: Revisiting the quasi-biennial oscillation as seen in era5. part i: Description and momentum budget. *Journal of the Atmospheric Sciences*, **78 (3)**, 673–691.

Pahlavan, H. A., J. M. Wallace, Q. Fu, and G. N. Kiladis, 2021b: Revisiting the quasi-biennial oscillation as seen in era5. part ii: Evaluation of waves and wave forcing. *Journal of the Atmospheric Sciences*, **78 (3)**, 693–707.

Palmer, T., 2024: The real butterfly effect and maggoty apples. *Physics Today*, **77 (5)**, 30–35.

Palmer, T. N., 2022: *The Primacy of Doubt: From climate change to quantum physics, how the science of uncertainty can help predict and understand our chaotic world*. Oxford University Press.

Pan, D.-M., and D. D. Randall, 1998: A cumulus parameterization with a prognostic closure. *Quarterly Journal of the Royal Meteorological Society*, **124 (547)**, 949–981.

Pauluis, O., V. Balaji, and I. M. Held, 2000: Frictional dissipation in a precipitating atmosphere. *Journal of the atmospheric sciences*, **57 (7)**, 989–994.

Pauluis, O., A. Czaja, and R. Korty, 2010: The global atmospheric circulation in moist isentropic coordinates. *Journal of Climate*, **23 (11)**, 3077–3093.

Pauluis, O. M., and A. A. Mrowiec, 2013: Isentropic analysis of convective motions. *Journal of the atmospheric sciences*, **70 (11)**, 3673–3688.

Peixoto, J. P., and A. H. Oort, 1992: *Physics of climate*. New York, NY (United States); American Institute of Physics.

Philander, S. G., 1990: *El Niño, La Niña, and the Southern Oscillation*. Academic Press, 293 pp.

Quiroz, R. S., 1986: The association of stratospheric warmings with tropospheric blocking. *Journal of Geophysical Research: Atmospheres*, **91 (D4)**, 5277–5285.

Randall, D., M. Khairoutdinov, A. Arakawa, and W. Grabowski, 2003: Breaking the cloud parameterization deadlock. *Bulletin of the American Meteorological Society*, **84 (11)**, 1547–1564.

Randall, D. A., 2013: Beyond deadlock. *Geophysical Research Letters*, **40 (22)**, 5970–5976.

Randall, D. A., and D.-M. Pan, 1993: Implementation of the arakawa-schubert cumulus parameterization with a prognostic closure. *The representation of cumulus convection in numerical models*, Springer, 137–144.

Reed, R. J., 1966: Zonal wind behavior in the equatorial stratosphere and lower mesosphere. *Journal of Geophysical Research*, **71 (18)**, 4223–4233.

Ren, H.-L., F.-F. Jin, J.-S. Kug, J.-X. Zhao, and J. Park, 2009: A kinematic mechanism for positive feedback between synoptic eddies and nao. *Geophysical Research Letters*, **36 (11)**.

Rhines, P. B., 1975: Waves and turbulence on a beta-plane. *Journal of Fluid Mechanics*, **69 (3)**, 417–443.

Richter, J. H., F. Sassi, and R. R. Garcia, 2010: Toward a physically based gravity wave source parameterization in a general circulation model. *Journal of the Atmospheric Sciences*, **67 (1)**, 136–156.

Riehl, H., and J. S. Malkus, 1958: On the heat balance in the equatorial trough zone. *Geophysica*, **6**, 537.

Roemmich, D., and Coauthors, 2009: The argo program: Observing the global ocean with profiling floats. *Oceanography*, **22 (2)**, 34–43.

Rosen, R. D., D. A. Salstein, T. M. Eubanks, J. O. Dickey, and J. A. Steppe, 1984: An El Niño signal in atmospheric angular momentum and Earth rotation. *Science*, **225 (4660)**, 411–414.

Rossby, C.-G., 1941: The scientific basis of modern meteorology. *Climate and Man. Yearbook of Agriculture*, U.S. Government Printing Office, 599–655.

Rossby, C.-G., 1947: On the distribution of angular velocity in gaseous envelopes under the influence of large-scale horizontal mixing processes. *Bulletin of the American Meteorological Society*, **28 (2)**, 53–68.

Rossby, C.-G., and Collaborators, 1937: Isentropic analysis. *Bulletin of the american meteorological society*, **18 (6-7)**, 201–209.

Sadourny, R., and C. Basdevant, 1985: Parameterization of subgrid scale barotropic and baroclinic eddies in quasi-geostrophic models: Anticipated potential vorticity method. *Journal of Atmospheric Sciences*, **42 (13)**, 1353–1363.

Savijärvi, H., 1988: Global energy and moisture budgets from rawinsonde data. *Monthly Weather Review*, **116 (2)**, 417–430.

Scherhag, R., 1952: Die explosionsartige stratosphaerenerwarmung des spaetwinters 1951/1952. *Ber. Deut. Wetterdienstes*, **6**, 51.

Scherhag, R., 1960: Stratospheric temperature changes and the associated changes in pressure distribution. *Journal of Atmospheric Sciences*, **17 (6)**, 575–583.

Schneider, T., 2006: The general circulation of the atmosphere. *Annual Review of Earth and Planetary Sciences*, **34**, 655–688.

Schoeberl, M. R., 1978: Stratospheric warmings: Observations and theory. *Reviews of Geophysics*, **16 (4)**, 521–538.

Schulman, L. L., 1973: On the summer hemisphere Hadley cell. *Quarterly Journal of the Royal Meteorological Society*, **99 (419)**, 197–201.

Sclater, J., C. Jaupart, and D. Galson, 1980: The heat flow through oceanic and continental crust and the heat loss of the Earth. *Reviews of Geophysics*, **18 (1)**, 269–311.

Sellers, P., and Coauthors, 1997: Modeling the exchanges of energy, water, and carbon between continents and the atmosphere. *Science*, **275 (5299)**, 502–509.

Shangguan, M., and W. Wang, 2022: The semi-annual oscillation (SAO) in the upper troposphere and lower stratosphere (UTLS). *Atmospheric Chemistry and Physics Discussions*, 1–25.

Shutts, G., 1986: A case study of eddy forcing during an Atlantic blocking episode. *Advances in Geophysics*, Vol. 29, Elsevier, 135–162.

Simmons, A., M. Hortal, G. Kelly, A. McNally, A. Untch, and S. Uppala, 2005: Ecmwf analyses and forecasts of stratospheric winter polar vortex breakup: September 2002 in the southern hemisphere and related events. *Journal of the Atmospheric Sciences*, **62 (3)**, 668–689.

Smith, R. K., 2013: *The physics and parameterization of moist atmospheric convection*, Vol. 505. Springer Science & Business Media.

Staniforth, A. N., 2022: *Global Atmospheric and Oceanic Modelling: Fundamental Equations*. Cambridge University Press.

Starr, V. P., 1945: A quasi-lagrangian system of hydrodynamical equations. *Journal of the Atmospheric Sciences*, **2 (4)**, 227–237.

Starr, V. P., 1948: An essay on the general circulation of the Earth's atmosphere. *Journal of Atmospheric Sciences*, **5 (2)**, 39–43.

Stephens, G., and D. O'Brien, 1993: Entropy and climate. I: ERBE observations of the entropy production of the Earth. *Quarterly Journal of the Royal Meteorological Society*, **119 (509)**, 121–152.

Sussman, G. J., and J. Wisdom, 1992: Chaotic evolution of the solar system. *Science*, **257 (5066)**, 56–62.

Tapley, B. D., S. Bettadpur, M. Watkins, and C. Reigber, 2004: The gravity recovery and climate experiment: Mission overview and early results. *Geophysical research letters*, **31 (9)**.

Taylor, G. I., 1950a: The formation of a blast wave by a very intense explosion i. theoretical discussion. *Proceedings of the Royal Society of London. Series A. Mathematical and Physical Sciences*, **201 (1065)**, 159–174.

Taylor, G. I., 1950b: The formation of a blast wave by a very intense explosion.-ii. the atomic explosion of 1945. *Proceedings of the Royal Society of London. Series A. Mathematical and Physical Sciences*, **201 (1065)**, 175–186.

Thayer-Calder, K., and D. A. Randall, 2009: The role of convective moistening in the madden–julian oscillation. *Journal of the Atmospheric Sciences*, **66 (11)**, 3297–3312.

Tillman, J. E., N. C. Johnson, P. Guttorp, and D. B. Percival, 1993: The martian annual atmospheric pressure cycle: Years without great dust storms. *Journal of Geophysical Research*, **98**, 10 963–10 971.

Tomas, R. A., and P. J. Webster, 1997: The role of inertial instability in determining the location and strength of near-equatorial convection. *Quarterly Journal of the Royal Meteorological Society*, **123 (542)**, 1445–1482.

Townsend, R. D., and D. R. Johnson, 1985: A diagnostic study of the isentropic zonally averaged mass circulation during the first garp global experiment. *Journal of Atmospheric Sciences*, **42 (15)**, 1565–1579.

Trenberth, K. E., and J. M. Caron, 2001: Estimates of meridional atmosphere and ocean heat transports. *Journal of Climate*, **14 (16)**, 3433–3443.

Trenberth, K. E., J. R. Christy, and J. G. Olson, 1987: Global atmospheric mass, surface pressure, and water vapor variations. *Journal of Geophysical Research: Atmospheres*, **92 (D12)**, 14 815–14 826.

Trenberth, K. E., J. T. Fasullo, and M. A. Balmaseda, 2014: Earth's energy imbalance. *Journal of Climate*, **27 (9)**, 3129–3144.

Trenberth, K. E., J. T. Fasullo, and J. Kiehl, 2009: Earth's global energy budget. *Bulletin of the American Meteorological Society*, **90 (3)**, 311–324.

Uppala, S. M., and Coauthors, 2005: The era-40 re-analysis. *Quarterly Journal of the Royal Meteorological Society: A journal of the atmospheric sciences, applied meteorology and physical oceanography*, **131 (612)**, 2961–3012.

Vallis, G. K., 2017: *Atmospheric and oceanic fluid dynamics*. Cambridge University Press.

VonderHaar, T. H., and A. H. Oort, 1973: New estimate of annual poleward energy transport by northern hemisphere oceans. *Journal of Physical Oceanography*, **3 (2)**, 169–172.

Wallace, J. M., and D. S. Gutzler, 1981: Teleconnections in the geopotential height field during the northern hemisphere winter. *Monthly weather review*, **109 (4)**, 784–812.

Wang, J., and D. A. Randall, 1994: The moist available energy of a conditionally unstable atmosphere. part ii: Further analysis of gate data. *Journal of Atmospheric Sciences*, **51 (5)**, 703–710.

Webster, P. J., 1972: Response of the tropical atmosphere to local, steady forcing. *Monthly Weather Review*, **100 (7)**, 518–541.

Wedi, N. P., and P. K. Smolarkiewicz, 2006: Direct numerical simulation of the plumb–mcewan laboratory analog of the QBO. *Journal of the atmospheric sciences*, **63 (12)**, 3226–3252.

Wheeler, M., and G. N. Kiladis, 1999: Convectively coupled equatorial waves: Analysis of clouds and temperature in the wavenumber–frequency domain. *Journal of Atmospheric Sciences*, **56 (3)**, 374–399.

White, A. A., and R. Bromley, 1995: Dynamically consistent, quasi-hydrostatic equations for global models with a complete representation of the coriolis force. *Quarterly Journal of the Royal Meteorological Society*, **121 (522)**, 399–418.

Wielicki, B. A., B. R. Barkstrom, E. F. Harrison, R. B. Lee III, G. L. Smith, and J. E. Cooper, 1996: Clouds and the Earth's radiant energy system (CERES): An Earth observing system experiment. *Bulletin of the American Meteorological Society*, **77 (5)**, 853–868.

Wielicki, B. A., and Coauthors, 1998: Clouds and the Earth's radiant energy system (CERES): Algorithm overview. *IEEE Transactions on Geoscience and Remote Sensing*, **36 (4)**, 1127–1141.

Wilczek, F., 2005: On absolute units, i: Choices. *Physics Today*, **58 (10)**, 12–13.

Wilczek, F., 2006a: On absolute units, ii: Challenges and responses. *Physics Today*, **59 (1)**, 10–11.

Wilczek, F., 2006b: On absolute units, iii: Absolutely not? *Physics Today*, **59 (5)**, 10–11.

Williams, P. D., and Coauthors, 2017: A census of atmospheric variability from seconds to decades. *Geophysical Research Letters*, **44 (21)**, 11–201.

Wing, A. A., and Coauthors, 2020: Clouds and convective self-aggregation in a multimodel ensemble of radiative-convective equilibrium simulations. *Journal of Advances in Modeling Earth Systems*, **12**.

Winker, D. M., R. H. Couch, and M. McCormick, 1996: An overview of lite: Nasa's lidar in-space technology experiment. *Proceedings of the IEEE*, **84 (2)**, 164–180.

Woollings, T., and Coauthors, 2018: Blocking and its response to climate change. *Current Climate Change Reports*, **4 (3)**, 287–300.

Xie, Y.-B., S.-J. Chen, I.-L. Chang, and Y.-L. Huang, 2018: A preliminarily statistic and synoptic study about the basic currents over southeastern asia and the initiation of typhoons. *Journal of Meteorological Research*, **32**, 661–669.

Xu, K.-M., and A. Arakawa, 1992: Semiprognostic tests of the arakawa-schubert cumulus parameterization using simulated data. *Journal of the atmospheric sciences*, **49 (24)**, 2421–2436.

Xu, K.-M., and K. A. Emanuel, 1989: Is the tropical atmosphere conditionally unstable? *Monthly Weather Review*, **117 (7)**, 1471–1479.

Zeitlin, V., 2018: Symmetric instability drastically changes upon inclusion of the full coriolis force. *Physics of Fluids*, **30 (6)**, 061 701.

Zent, A. P., 1996: The evolution of the martian climate. *American scientist*, **84 (5)**, 442–451.